A STUDY OF THE REACTION $e^+e^- \rightarrow \mu^+\mu^-$ USING THE CELLO DETECTOR

by

Craig McLeod Buttar

Department of Physics and Astronomy

University of Glasgow

Submitted for the degree of PhD

at the University of Glasgow

October 1987

Abstract

A study was made of the reaction $e^+e^- \rightarrow \mu^+\mu^-$ using the CELLO detector at PETRA. Using data collected at a centre of mass energy of 35 GeV the total cross section, σ_0 and the electroweak charge asymmetry A_{fb} were measured giving:

$$R_{\mu\mu} = \frac{\sigma_0}{\sigma_{QED}} = 0.95 \pm 0.02 \pm 0.05$$

$$A_{fb} = -8.9 \pm 2.0 \pm 1.0 \ \%$$

The results are in good agreement with the values predicted by the electroweak model of $R_{\mu\mu} = 1.0$ and $A_{fb} = -8.9\%$ at this energy.

Using data collected at a centre of mass energy of 43 GeV a search was made for acoplanar muon pairs, a signature of scalar muons. No candidates were found and the following masses were excluded at the 95% C.L.

$$2.8 < M_{\tilde{\mu}L} = M_{\tilde{\mu}R} < 20.5 \ \frac{GeV}{c^2}$$

$$3.4 < M_{\tilde{\mu}R} < 20.5 \ \frac{GeV}{c^2} \ < M_{\tilde{\mu}L}$$

assuming $M_{\tilde{\gamma}} = 0 \ \frac{GeV}{c^2}$.

Contents

Preface

This thesis describes a study of $e^+e^- \rightarrow \mu^+\mu^-$ using the CELLO detector at the PETRA e^+e^- collider situated at DESY, Hamburg. From data collected at a centre of mass energy of 35 GeV, the total cross-section and the electroweak charge asymmetry were measured and used to test the theory of quantum electrodynamics and the electroweak model respectively. In addition, data collected at a centre of mass energy of 43 GeV were used to search for evidence of scalar muons. Such particles are predicted by supersymmetric models which are a possible path beyond the present model of particle interactions.

The results obtained in this thesis depend directly or indirectly on the work of many people, although the physics analysis presented in this thesis is the individual work of the author.

In addition to his work on the analysis of μ-pairs, the author was involved with the supervision and maintenance of the muon detectors.

No portion of the work referred to in this thesis has been submitted in support of an application for another degree or qualification in this or any other university or institution of learning.

Acknowledgements

I wish to thank the Department of Physics and Astronomy under Prof. E. Laing and the High Energy Physics group under Prof. I. Hughes for giving me the opportunity to undertake this research. My thanks also go to my supervisor Prof. Ian Skillicorn for his help, guidance and encouragement during this study, to Drs. Peter Bussey and John Dainton for their advice and help, and Dr. Alan Campbell for his help with all aspects of CELLO hardware and software.

I would also like to thank the other members of the CELLO Collaboration for all their help and encouragement, particularly Drs. Wim de Boer and George Cozzika, and Hermann Kuster. This study was made considerably easier through many discussions with, and the patient help of, Dr. Farid Ould-Saada.

My stay in Hamburg, travel and dealings with the Science and Engineering Research Council were made much easier through the ready help of Catherine McIntyre in Glasgow and Josephine Zilberkweit in Hamburg.

I should also like to thank the Science and Engineering Research Council for their financial support throughout the three years.

My stay in Hamburg was made very enjoyable through the friendship of: Paul, Tim, Sandra, Graham, Kitti, Hertha, Richard, Howard, Heike, Denis, Farid and Maggie. My thanks to all of them for many hours of fun.

I would like to thank my family for their support and encouragement, and last but certainly not least, Pamela for washing the car.

Chapter 1

Theoretical Introduction

1.1 Introduction

During the last decades of the 19th century and the first decades of the 20th physical science gave man a new perception of the Universe. In 1867 James Clerk Maxwell unified the theories of magnetism and electricity into the single elegant theory of electromagnetism. This led to the idea that light was an electromagnetic wave and the subsequent discovery of other parts of the electromagnetic spectrum such as radio waves. The failure to detect a medium through which electromagnetic waves propagated, led Einstein to propose the theory of special relativity showing that the world is not simply three-dimensional in space but is four-dimensional in space and time, and that energy has mass. Rutherford's observation of large angle α-particle scattering from gold foil proved that the atoms were not elementary but had a compact massive nucleus with orbiting electrons. Bohr developed a theory to describe the Rutherford atom which led

to the formulation of quantum mechanics by Heisenberg and Schrodinger. Dirac combined the ideas of relativity and quantum theory and laid the foundations of quantum field theory.

In recent years the study of high energy physics has again produced fundamental changes in how we understand the physical world. Gone is the world of atoms made up of nucleons and electrons. Now we have two families of fermions, particles having odd integral spin, the leptons and the quarks. The leptons are the electron and its heavier partners, the muon and the tau and their associated neutrinos which are electrically neutral and are believed to be massless. The quarks are fractionally charged fermions introduced to explain, in terms of symmetry principles, the structure of the large number of particles discovered such as the proton and neutron, the pions and the Ω^-. Originally it was thought that the quarks might only be mathematical objects convenient for the description of the observed particle spectra. However in electron-proton scattering experiments it was discovered that the proton was not point-like and further evidence, such as the observation of jets in e^+e^- annihilation, have established that the quarks are physical particles. The present members of the two families are shown in Figures 1.1 and 1.2. A question mark is shown beside

$$\begin{pmatrix} e^- \\ \nu_e \end{pmatrix} \begin{pmatrix} \mu^- \\ \nu_\mu \end{pmatrix} \begin{pmatrix} \tau \\ \nu_\tau \end{pmatrix}$$

Figure 1.1: The lepton family

the top quark as it has not yet been experimentally observed.

Just as our view of what particles are fundamental has changed, so have

$$\begin{pmatrix} u \\ d \end{pmatrix} \begin{pmatrix} c \\ s \end{pmatrix} \begin{pmatrix} t? \\ b \end{pmatrix}$$

Figure 1.2: The quark family

our ideas about how particles interact. Until recently it was believed that the interactions of the quarks and leptons were governed by four forces: the electromagnetic force describing interactions between particles with electric charge, the weak force which is responsible for interactions such as μ-decay and β-decay, the colour force which describes how quarks interact and the gravitational force which governs how masses interact.

The electromagnetic interaction is described by the theory of quantum electrodynamics (QED). Precision tests such as the measurement of the anomalous magnetic moment of the electron and the muon and measurement of the mass of the photon have verified the theory. The observation that QED is locally gauge invariant and development of the ideas of renormalisation to deal with the infinities in the theory, have proved to be sound bases on which to build other physical theories.

The colour force is described by the theory of quantum chromodynamics (QCD), each of the quarks having three colour states. Colour was orginally introduced to solve the problem of three quarks existing in a symmetric quantum state for example the Δ^{++}, violating the Pauli exclusion principle, but has proved to play a similar role to electric charge. Quarks in the theory of QCD interact via their colour charges by the exchange of massless gluons. However QCD is not simply another version of QED. It is a non-abelian gauge theory

having SU(3) symmetry. This means that there are eight gluons having colour charge so that they interact not only with the quarks but also with themselves. The colour force is the strongest force having a coupling constant α_s, QCD's equivalent of QED's fine structure constant α, of the order of 1. The QCD coupling constant unlike that of QED increases in strength as the distance between the charges increases. This property known as confinment. is believed to be the reason why free quarks have never been observed by experiment.

Although gravity controls the large scale structure of the Universe, in the realm of high energy physics it is many orders of magnitude weaker than even the weak force because of the small masses involved and so its effects are not considered.

After many years of development it was realised that the weak and electromagnetic interaction could be described by an $SU(2) \times U(1)$ gauge symmetry. So just as Maxwell had unified electricity and magnetism, about 100 years later electromagnetism was unified with the weak interaction. This is not a unification as complete as that of electricity and magnetism since the theory requires two coupling constants. It is nevertheless a powerful theory able to describe both electromagnetic interactions and weak interactions.

Although the electroweak theory was elegant it did not have much experimental evidence to back it up. However the observation of neutral currents at the BEBC at CERN in 1974 [1] and the discovery of the intermediate vector bosons, the W^+, W^-, and the Z^0 [2], with the masses predicted by this theory have made it the so called standard model. As it forms the theoretical basis for

this thesis it will be discussed in more detail later in this Chapter.

Having related the electromagnetic and the weak force many theorists are now trying to produce a theory which describes all the forces. One of the more successful theoretical ideas being explored is that of supersymmetry. This assumes that every boson, a particle having integral spin, has a fermion partner and every fermion has a boson partner. The derivatives of supersymmetry, supergravity and superstrings, are turning out to be promising candidates for grand unified theories. This is discussed further in Chapter 8.

1.2 Development of weak interaction theory

The Fermi theory of beta decay

Using ideas from QED, Fermi developed a current-current interaction (Figure 1.3) to describe β-decay:

$$n \rightarrow p\ e^-\ \bar{\nu}_e$$

Originally Fermi assumed a vector current interaction, as in QED, with a cou-

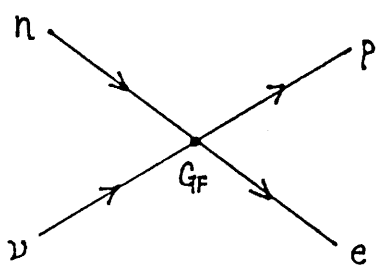

Figure 1.3: Fermi's picture of β-decay

pling constant G_F. Although this was successful in describing some experimental observations it failed to describe others. It was noted by Fermi and others

that a current-current interaction Lagrangian could be written much more generally by taking linear combinations of bilinear covariants.

$$L_\beta = \frac{G_F}{\sqrt{2}} \sum_{j=S,V,T,A,P} \bar{\psi}_p O_j \psi_n \bar{\psi}_e O_j \psi_{\bar{\nu}} \tag{1.1}$$

where G_F is the Fermi coupling constant and O_j are the bilinear covariants

$$\begin{aligned} S &= Scalar = \bar{\psi}\psi \\ V &= Vector = \bar{\psi}\gamma^\mu\psi \\ T &= Tensor = \bar{\psi}\sigma^{\mu\nu}\psi \\ A &= Axial - vector = \bar{\psi}\gamma^5\gamma^\mu\psi \\ P &= Pseudo - scalar = \bar{\psi}\gamma^5\psi \end{aligned} \tag{1.2}$$

where the γ^μs are the usual gamma matrices and $\sigma^{\mu\nu}$ is defined as

$$\sigma^{\mu\nu} = \frac{i}{2}(\gamma^\mu\gamma^\nu - \gamma^\nu\gamma^\mu) \tag{1.3}$$

Parity non-conservation

Originally it was assumed that the Lagrangian must be both Lorentz invariant and invariant under parity transformations. However to explain the τ-θ puzzle: The observation of two particles with the same mass and lifetime decaying into opposite parity states ($K^- \rightarrow 3\pi$ and $K^- \rightarrow 2\pi$ decays), Lee and Yang [3] proposed that parity was not conserved by weak interactions. This was soon confirmed by the observation of a forward-backward asymmetry in the β-emission of polarized ^{60}Co nuclei [4].

The V-A structure of weak currents

After much theoretical and experimental activity arising from discovery of parity violation in weak interactions a generalisation of the Fermi current-current interaction was proposed by Feynman and Gell-Man [5]. Instead of a pure vector interaction a V-A, vector axial-vector interaction was proposed.

$$L_\beta = \frac{G_F}{\sqrt{2}}(\bar{\psi}_p\gamma^\mu(C_v - C_a\gamma^5)\psi_n)(\bar{\psi}_e\gamma_\mu(1-\gamma^5)\psi_\nu) \tag{1.4}$$

where C_v and C_a are constants describing how the hadron current deviates from pure V-A due to strong interaction effects. This structure of the weak currents was verifed by measurement of the electron neutrino's helicity and measurement of the polarisation of electrons from β-decay [6].

The $(1-\gamma^5)\psi_\nu$ implies that only left-handed helicity states ($H = -\frac{1}{2}$) of neutrinos take part in weak interactions, coupling to left-handed electrons, where helicity is defined for a particle having spin $\frac{1}{2}\boldsymbol{\sigma}$ and momentum $\mathbf{p}$ as

$$H = \frac{\boldsymbol{\sigma}\cdot\mathbf{p}}{|\,\mathbf{p}\,|} \tag{1.5}$$

This description of weak interactions where only right-handed antineutrinos and left-handed neutrinos take part is said to be maximally parity violating.

Problems with the Fermi theory

Although the V-A current-current interaction was very successful, it carried within it the seeds of its own destruction. If the reaction $\nu_\mu e^- \rightarrow \mu^-\nu_e$ is examined, then its cross-section grows with the centre of mass energy squared, s. This can be shown to be due to the coupling constant in the theory, G_F, having

units GeV^{-2}. The cross-section has units of GeV^{-2} but is proportional to G_F^2 which has units GeV^{-4}. Therefore the cross-section must also be proportional to a Lorentz invariant variable having units GeV^2; such as s. This growth of the cross-section with energy leads to a violation of unitarity at high energies. This problem cannot be solved by including higher order diagrams since these diverge. In QED these divergences also arise but can be absorbed in the mass and charge which are then replaced by their experimentally measured values. This procedure removes divergences to all orders, thus QED is said to be renormalisable. However in the Fermi theory an infinite number of parameters would be required to remove divergences to all orders. So the theory has no predictive power and is said to be non-renormalisable.

Interacting vector boson model

A possible solution to the violation of unitarity in the Fermi theory is to introduce massive force carriers having a dimensionless coupling g, removing the problem of a dimensional coupling. To describe the then identified weak processes required two charged intermediate vector bosons (IVBs) the W^+ and the W^-, of mass M_W . The matrix element for muon-decay would then be[7]

$$M = -g\bar{u}_e\gamma_\lambda(1-\gamma^5)v_\nu \left(\frac{g^{\lambda\sigma} - \frac{1}{M_W^2}q^\lambda q^\sigma}{q^2 - M_W^2} \right) g\bar{u}_\nu\gamma_\sigma(1-\gamma_5)u_\mu \qquad (1.6)$$

The extra $\frac{1}{M_W^2}q^\lambda q^\sigma$ term in the propagator arises because massive vector particles have longitudinal polarisation states, the implications of which are dicussed below.

At low energies $q^2 << M_W^2$ the V-A theory is known to describe muon decay.

So comparing the IVB matrix element with the V-A matrix element gives

$$\frac{G_F}{\sqrt{2}} = \frac{g^2}{8M_W^2} \tag{1.7}$$

This shows that the weakness of the weak interaction can be identified with the large masses of the IVBs. If this is done then the weak and electromagnetic interactions can be unified by asserting $g = e$.

However it turns out that, like the Fermi theory, the IVB theory violates unitarity at high energies and is non-renormalisable. The problem arises because of the $W^{\pm}$'s longitudinal polarisation states. In reactions where the Ws act as mediators of the weak force it is found that unitarity is no longer violated because the coupling is now dimensionless, but in reactions containing real Ws, such as $\nu_\mu \bar{\nu}_\mu \rightarrow W^+W^-$, the longitudinal polarisation states result in a cross-section that increases with energy. To seek guidance theorists turned to QED and looked at a process containing external photons, $e^+e^- \rightarrow \gamma\gamma$. Why do the longitudinal polarisation states of the photon not cause this cross-section to violate unitarity at high energies ? The answer is that photons have no longitudinal polarisation state and this can be attributed to the gauge invariance of the photon.

This success of the gauge structure of QED persuaded theorists to try to construct a gauge theory of weak interactions. However, as will be shown in Section 1.3, gauge invariance requires that the gauge bosons be massless. Therefore two important problems had to be solved before a gauge theory of weak interactions could be written down: what is the gauge group and how can the gauge bosons acquire their masses ?

Neutral currents

Despite the failure of the IVB model, it was believed that electromagnetic and weak interactions could be unified by treating the IVBs and the photon as a triplet of vector bosons with a single universal coupling. Glashow [8] showed that the $W^{\pm}$ and the γ could not be described by a single triplet but that the $W^{\pm}$ and a new neutral vector boson, coupling to a weak neutral current, could be associated with a $SU(2)_L$ symmetry, the L denoting that the weak vector bosons have only left-handed couplings thus retaining the successful V-A structure of the charged weak currents. However this seems to preclude the possibility of including the photon in the theory. Glashow therefore introduced a $U(1)_Y$ group such that

$$Q = T_3 + \frac{Y}{2} \tag{1.8}$$

where Q is the electric charge, T_3 is the third component of the weak isospin and Y is the weak hypercharge associated with the $U(1)_{em}$, $SU(2)_L$, and the $U(1)_Y$ groups respectively. Demanding local gauge invariance under $SU(2)_L \times U(1)_Y$ requires that four gauge bosons be introduced: a triplet from $SU(2)_L$ and a singlet from $U(1)_Y$. Two members of the $SU(2)_L$ triplet can be combined to form the charged current IVBs, the W^+ and the W^-. The $U(1)_Y$ gauge boson and the third member of the $SU(2)_L$ triplet are mixed, introducing the weak mixing or Weinberg angle θ_w, to give two gauge bosons one of which can be identified as the photon through (1.8) and the other as a weak neutral vector boson, the Z^0 .

Glashow established only partial symmetries, symmetries of the Lagrangian

where the mass terms are ignored, thus ignoring the problem of the IVB masses but it turns out this was exactly the right thing to do.

Spontaneous symmetry breaking

Gauge symmetries are broken by mass terms in the Lagrangian but Glashow showed that the $SU(2)_L \times U(1)_Y$ gauge symmetry was a good candidate for describing weak and electromagnetic interactions in the same theory. How can these two ideas be reconciled ? The answer is the concept of hidden or spontaneously broken symmetries. The symmetry although manifest in the Lagrangian of the theory is hidden or broken because the ground state about which the field theory is built does not possess this symmetry. The breaking of a global gauge symmetry introduces a massive scalar particle and massless scalar particles which have not been observed by experiment. However, as will be discussed below, it is believed that theories which are locally gauge invariant are better physical models. Does this solve the problem of massless scalars ? When a local gauge symmetry is broken a massive scalar particle is introduced and the gauge bosons acquire mass by absorbing the massless scalars as the additional degree of freedom they require to be massive. The application of this to $SU(2)_L \times U(1)_Y$ gauge symmetry is the Higgs mechanism [9] and the associated scalar boson, the much sought Higgs particle.

1.3 Gauge invariance and QED

In Section 1.2 we showed why theorists were led to believe that the answer to the problems of the weak interactions were gauge symmetries. Here using the example of the model gauge theory, QED, several important properties of gauge symmetries will be demonstrated.

The Lagrangian for a free spin-$\frac{1}{2}$ particle is

$$L_0 = \bar{\psi}(i\gamma^\mu \partial_\mu - m)\psi \tag{1.9}$$

This is invariant under the gauge transformation

$$\psi(x) \rightarrow \psi'(x) = e^{i\alpha}\psi(x) \tag{1.10}$$

where α is a constant. These transformations are described by the $U(1)$ group and are global transformations since they fix the phase at all space-time points to the same value simultaneously. The invariance of the Lagrangian implies a conserved current (Noethers theorem) of the form:

$$J^\mu = \bar{\psi}\gamma^\mu\psi \tag{1.11}$$

If we write $\alpha = q\Theta$ then the current is

$$J^\mu_{em} = q\bar{\psi}\gamma^\mu\psi \tag{1.12}$$

The current can be identified with the electromagnetic current for a fermion with charge q.

However Yang and Mills [10] thought that fixing the phase instantaneously over all space-time simultaneously was unphysical. Therefore they proposed

that Lagrangians be made locally gauge invariant i.e. the Lagrangian should be invariant under the transformation

$$\psi(x) \rightarrow \psi'(x) = e^{i\alpha(x)q}\psi \tag{1.13}$$

The Lagrangian is no longer invariant under this transformation because the space-time dependence of α results in an additional derivative term which breaks the gauge invariance, an extra term is then required in the Lagrangian to cancel the derivative term and restore gauge invariance. Such a term is

$$q\bar{\psi}\gamma^{\mu}\psi A_{\mu} \tag{1.14}$$

provided, under gauge transformations, A_{μ} transforms as

$$A_{\mu} \rightarrow A'_{\mu} = A_{\mu} + \partial_{\mu}\alpha(x) \tag{1.15}$$

The cancellation term, (1.14), is the interaction of an electromagnetic current with a vector field A_{μ} which can be identified with the photon. Imposing local gauge invariance on the free particle Lagrangian generates an interaction with a vector field A_{μ}. So the locally gauge invariant Lagrangian is

$$L_{int} = \bar{\psi}(i\gamma^{\mu}\partial_{\mu} - m)\psi + q\bar{\psi}\gamma^{\mu}\psi A_{\mu} \tag{1.16}$$

This cannot yet be identified with the QED Lagrangian since there is no term describing the dynamics of the gauge field. A term is therefore added, which is called a Yang-Mills term. As it must be gauge invariant the gauge invariant field tensor $F_{\mu\nu}$ is used

$$F_{\mu\nu} = \partial_{\mu}A_{\nu} - \partial_{\nu}A_{\mu} \tag{1.17}$$

The full Lagrangian is then

$$L_{qed} = \bar{\psi}(i\gamma^{\mu}\partial_{\mu} - m)\psi - q\bar{\psi}\gamma^{\mu}\psi A_{\mu} - \frac{1}{4}F_{\mu\nu}F^{\mu\nu} \tag{1.18}$$

Gauge invariance implies that the photon must be massless since adding a mass term $\frac{1}{2}m_\gamma A_\mu A^\mu$ would break the gauge invariance. This property of gauge symmetries has important consequences for the electroweak model described later.

Generally local gauge invariance can be restored by replacing ∂_μ with the covariant derivative D_μ, where D_μ transforms in the same way as ψ under local gauge transformations such that:

$$D_\mu\psi \rightarrow D'_\mu\psi' = e^{i\alpha(x)q}D_\mu\psi \tag{1.19}$$

For QED

$$D_\mu = \partial_\mu - iqA_\mu \tag{1.20}$$

In this Section we have shown how local gauge symmetries can be used to generate interactions by introducing massless gauge bosons. Now these ideas will be applied to Glashow's $SU(2)_L \times U(1)_Y$ to generate the electroweak model.

1.4 The electroweak model

Using the ideas of Glashow and the Higgs mechanism, Weinberg [11] and Salam [12] constructed a gauge theory which could describe both weak and electromagnetic interactions. They postulated that because the unbroken Lagrangian contained only massless gauge bosons the theory would be renormalisable and in 1971 't Hooft was able to show that this was so [13].

The electroweak model is based on an $SU(2)_L \times U(1)_Y$ gauge symmetry. As for QED demanding that the Lagrangian be invariant under these gauge

transformations introduces the fermion gauge boson interactions. The $SU(2)_L$ group describes the interactions of left-handed lepton doublets, χ_L Figure 1.4 via a triplet of fields $W_\mu^{1,2,3}$ with coupling g. The $U(1)_Y$ describes the interactions of the left-handed doublets and the right-handed singlets, ψ_R, Figure (1.4), via neutral vector boson B_μ with coupling g'.

$$\begin{pmatrix} e^- \\ \nu_e \end{pmatrix}_L \quad \begin{pmatrix} \mu^- \\ \nu_\mu \end{pmatrix}_L \quad \begin{pmatrix} \tau^- \\ \nu_\tau \end{pmatrix}_L$$

$$e_R^- \quad \mu_R^- \quad \tau_R^-$$

Figure 1.4: The left handed lepton doublets and right handed singlets

The gauge transformations are written,

$$\chi_L \rightarrow \chi_L' = (exp(i\boldsymbol{\alpha}(x) \cdot \mathbf{T}) + i\beta(x)Y)\chi_L \tag{1.21}$$

$$\psi_R \rightarrow \psi_R' = exp(i\beta(x)Y)\psi_R \tag{1.22}$$

where the T_i are the generators of the $SU(2)_L$ group satisfying the $SU(2)$ algebra

$$[T_i, T_j] = i\epsilon_{ijk}T_k \tag{1.23}$$

and Y is the generator of the $U(1)_Y$ group. The generators of the $SU(2)_L$ and $U(1)_Y$ are defined such that the charge generator of $U(1)_{em}$ is, see Section 1.2,

$$Q = T_3 + \frac{Y}{2} \tag{1.24}$$

so that the correct electromagnetic current can be recovered from the Lagrangian. The leptons have the quantum numbers shown in Table 1.1

Lepton	$\mathbf{T}, T_3$	Y	Q
$\nu_e\ \nu_\mu\ \nu_\tau$	$\frac{1}{2},\ \frac{1}{2}$	-1	0
$e_L^-\ \mu_L^-\ \tau_L^-$	$\frac{1}{2},\ -\frac{1}{2}$	-1	-1
$e_R^-\ \mu_R^-\ \tau_R^-$	0, 0	-2	-1

Table 1.1: Electroweak quantum numbers of the leptons

As for QED the interactions are introduced by requiring that the Lagrangian is locally gauge invariant which is equivalent to replacing the derivative with the covariant derivative. The $SU(2)_L$ and $U(1)_Y$ then introduce the following covariant derivatives. For left-handed states

$$D_\mu = \partial_\mu - ig\frac{1}{2}\boldsymbol{\tau}\cdot\mathbf{W}_\mu - ig'\frac{Y}{2}B_\mu \tag{1.25}$$

where the $\boldsymbol{\tau}$s are the Pauli spin matrices and for right-handed states

$$D'_\mu = \partial_\mu - ig'\frac{Y}{2}B_\mu \tag{1.26}$$

then the Lagrangian is

$$L_1 = \bar{\chi}_L(i\gamma^\mu D_\mu)\chi_L + \bar{\psi}_R(i\gamma^\mu D'_\mu)\psi_R + \frac{1}{4}\mathbf{W}_{\mu\nu}\mathbf{W}^{\mu\nu} + \frac{1}{2}B_{\mu\nu}B^{\mu\nu} \tag{1.27}$$

where the last two terms describe the dynamics of the vector fields. $B_{\mu\nu}$ is the same as $F_{\mu\nu}$ since they both describe $U(1)$ gauge invariances. However the $\mathbf{W}_{\mu\nu}$ comes from a non-abelian $SU(2)$ group,

$$\mathbf{W}_{\mu\nu} = \partial_\mu\mathbf{W}_\nu - \partial_\nu\mathbf{W}_\mu - g\mathbf{W}_\mu\times\mathbf{W}_\nu \tag{1.28}$$

The last-term results in interactions between the weak vector bosons. This occurs because the $\mathbf{W}$s are the gauge bosons of a group whose generators do not commute.

The above Lagrangian contains no mass terms but to be consistent with experiment there must be three massive vector fields,the W^+, W^- and the Z^0, and one massless one, the photon. To generate the masses the Higgs mechanism is used. A complex scalar doublet is introduced

$$\begin{pmatrix} \phi^+ \\ \phi^0 \end{pmatrix} = \frac{1}{\sqrt{2}} \begin{pmatrix} \phi_1 + i\phi_2 \\ \phi_3 + i\phi_4 \end{pmatrix} \tag{1.29}$$

with $(\mathbf{T},\ T_3) = (\frac{1}{2},\ \pm\frac{1}{2})$ and $Y = 1$. This choice is important as both the $SU(2)_L$ and the $U(1)_Y$ symmetries are broken but for the ϕ^0 the $U(1)_{em}$ symmetry remains unbroken. This ensures that after the $SU(2)_L \times U(1)_Y$ symmetry is broken the $U(1)_{em}$ symmetry remains unbroken thus preserving charge conservation.

The Lagrangian describing these particles is

$$L_H = (D_\mu \phi)^+ (D^\mu \phi) + \frac{1}{2}\mu^2(\phi^+\phi) - \frac{1}{4}\lambda(\phi^+\phi)^4 \tag{1.30}$$

The use of the covariant derivative, D_μ, ensures that the Lagrangian is invariant under $SU(2)_L \times U(1)_Y$ transformations. The potential part of the Lagrangian, the Higgs potential, has $\mu^2 < 0$ which gives a mass term of the wrong sign. The Higgs potential is minimised for

$$\phi = v = \sqrt{\frac{\mu^2}{2\lambda}} \tag{1.31}$$

and in fact $\phi = 0$ is a local maximum. If the Lagrangian could be solved exactly then this would not be important but since perturbation methods are used to solve problems in quantum field theory the Lagrangian should be defined about the minimum of the potential, the vacuum. There is therefore a set of degenerate

vacua defined by

$$\phi_1^2 + \phi_2^2 + \phi_3^2 + \phi_4^2 = \frac{\mu^2}{2\lambda} \tag{1.32}$$

However one vacuum must be chosen about which particles are to be defined. Choose

$$\phi_1 = \phi_2 = \phi_4 = 0 \quad \phi_3 = \frac{\mu^2}{\lambda} \tag{1.33}$$

The scalar doublet, equation 1.29 above, can be rewritten to first order in terms of perturbations about the vacuum

$$\phi(x) = exp(i\boldsymbol{\theta}(x) \cdot \frac{\boldsymbol{\tau}}{2v}) \begin{pmatrix} 0 \\ \frac{v+\sigma(x)}{\sqrt{2}} \end{pmatrix} \tag{1.34}$$

The four real fields are now three phase degrees of freedom and one real field. The $\boldsymbol{\theta}$ degrees of freedom can be gauged away by defining the gauge transformation of the $\mathbf{W}_\mu$ as

$$\mathbf{W}_\mu \rightarrow \mathbf{W}'_\mu = \mathbf{W}_\mu - \frac{1}{g}\partial_\mu \boldsymbol{\theta} \times \mathbf{W}_\mu \tag{1.35}$$

This may seem very artificial however if an arbitary gauge is chosen then an additional degree of freedom is introduced to the Lagrangian. Since the process described above cannot generate an additional physical degree of freedom this additional degree of freedom should be removed somehow and this is done by defining the above gauge transformation. However to prove renormalisability of the theory these unphysical degrees of freedom are neccesary.

The resulting Lagrangian is then

$$L'_H = \frac{1}{2}\partial_\mu \sigma \partial^\mu \sigma - \frac{1}{2}\mu^2\sigma^2 \tag{1.36}$$

$$+ \frac{1}{8}v^2 g^2 (W_\mu^1 W^{1\mu} + W_\mu^2 W^{2\mu}) \tag{1.37}$$

$$+\frac{1}{8}v^2(gW_\mu^3 - g'B_\mu)(gW^{3\mu} - g'B^\mu) + \cdots \tag{1.38}$$

The Lagrangian now describes a scalar particle, the Higgs boson, with mass μ and contains mass terms for the vector bosons. The $+\cdots$ contains Higgs self interaction terms and Higgs gauge boson interaction terms. From the $W^{1,2}$ the physical $W^\pm$ fields are defined

$$W^+ = \frac{1}{\sqrt{2}}(W_\mu^1 + iW_\mu^2) \quad W^- = \frac{1}{\sqrt{2}}(W_\mu^1 - iW_\mu^2) \tag{1.39}$$

The masses of the $W^\pm$ are then

$$M_W = \frac{1}{2}vg \tag{1.40}$$

The W^3 and the B field are mixed so that neither field has definite mass. To get the physical particles, a linear combination of W^3 and B must be defined

$$A_\mu = -sin\theta_w W_\mu^3 + cos\theta_w B_\mu \quad Z_\mu = cos\theta_w W_\mu^3 - sin\theta_w B_\mu \tag{1.41}$$

where

$$tan\theta_w = \frac{g'}{g} \tag{1.42}$$

The masses are then

$$M_A = 0 \qquad M_Z = \frac{1}{2}v\sqrt{g^2 + g'^2} \tag{1.43}$$

From (1.40),(1.42) and (1.43)

$$cos\theta_w = \frac{M_W}{M_Z} \tag{1.44}$$

If the covariant derivatives are written in terms of the physical particles then

$$D_\mu = \partial_\mu + igsin\theta_w(T_3 + \frac{Y}{2})A_\mu + i\frac{g}{cos\theta_w}(T_3 cos^2\theta_w - \frac{Y}{2}sin^2\theta_w)Z_\mu + \cdots \tag{1.45}$$

Using (1.24) and (1.43) we can identify A_μ as the photon and therefore:

$$e = g sin\theta_w \tag{1.46}$$

The fermions can also be given masses by the Higgs mechanism by introducing another term into the Lagrangian

$$L_3 = -G_l(\bar{\chi}_L \phi \psi_R + \bar{\psi}_R \phi^+ \chi_L) \tag{1.47}$$

after the symmetry is broken the term becomes

$$L_3' = -\frac{G_l v}{\sqrt{2}}(\bar{\chi}_L \psi_R + \bar{\psi}_R \chi_L) - \frac{G_l v}{\sqrt{2}}(\bar{\chi}_L \psi_R + \bar{\psi}_R \chi_L)\sigma \tag{1.48}$$

$$= -\frac{G_l v}{\sqrt{2}}(\bar{\psi}\psi) - \frac{G_l v}{\sqrt{2}}(\bar{\psi}\psi)\sigma \tag{1.49}$$

The $\bar{\psi}\psi$ term is a lepton mass term so

$$\frac{G_l v}{\sqrt{2}} = m_l \tag{1.50}$$

Thus L_3 can be finally written as

$$L_3 = -m_l \bar{\psi}_l \psi_l - \frac{m_l}{v}\bar{\psi}_l \psi_l \sigma \tag{1.51}$$

The second term describes a lepton-Higgs coupling which is proportional to lepton mass.

We have presented above a classical Lagrangian. To quantise this and extract the Feynman rules for this theory the path integral formalism of quantum field theory is used. This is considered to be beyond the scope of an experimental thesis but can be found in [14].

For the study of $e^+e^- \rightarrow \mu^+\mu^-$ the relevent part of the Lagrangian is the part describing the interaction of fermions and the photon and the Z^0, L_{NC},

the neutral current Lagrangian:

$$L_{NC} = -e\bar{\psi}\gamma^{\mu}Q\psi A_{\mu} - \frac{g}{cos\theta_{w}}\bar{\psi}\gamma^{\mu}((1-\gamma^{2})T_{3} - 2Qsin^{2}\theta_{W})\psi Z_{\mu} \qquad (1.52)$$

The predictions of this theory are discussed in Chapter 2.

Chapter 2

Physics of e^+e^- annihilation

2.1 QED processes

In electron positron annihilation the process $e^+e^- \rightarrow l\bar{l}$ is decribed to lowest order by the Feynman diagram shown in Figure 2.1.

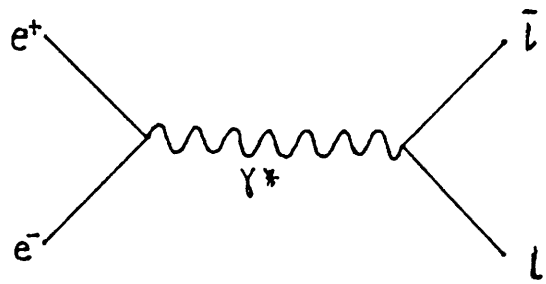

Figure 2.1: QED diagram for $e^+e^- \rightarrow l\bar{l}$

For Bhabha scattering ($e^+e^- \rightarrow e^+e^-$) there is an additional diagram, Figure 2.2

The cross-section for the process $e^+e^- \rightarrow l\bar{l}$ where l is any lepton, with

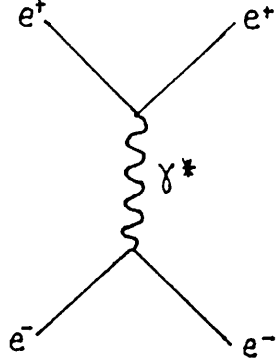

Figure 2.2: Additional diagram for Bhabha scattering

energy E and momentum **p**, except the electron is

$$\frac{d\sigma}{d\Omega} = \frac{\alpha^2}{4s}(\beta(1 + cos^2\theta) + (1 - \beta^2)sin^2\theta) \tag{2.1}$$

where $\beta = \frac{p}{E}$ is the velocity of the fermion, $\sqrt{s}$ is the centre of mass energy, α the QED coupling constant and θ is the scattering angle between the electron and the fermion, illustrated in Figure 2.3.

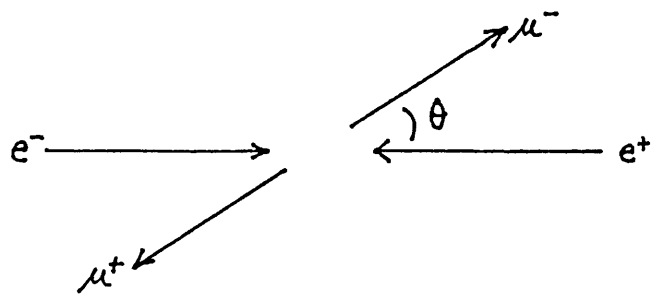

Figure 2.3: Definition of θ

In $e^+e^- \rightarrow \mu^+\mu^-$ at PETRA energies, $\beta \rightarrow 1$ and so the cross-section simplifies to

$$\frac{d\sigma}{d\Omega} = \frac{\alpha^2}{4s}(1 + cos^2\theta) \tag{2.2}$$

The total cross-section $\sigma_{\mu\mu}$ is found by integrating (2.2) over the total solid angle

$$\sigma_{\mu\mu} = \frac{4\pi\alpha^2}{3s} \tag{2.3}$$

Second order processes such as final state radiation, shown in Figure 2.4 are

important because they can be confused with $e^+e^- \rightarrow \mu^+\mu^-$ events due to the finite resolution of the detector. This is discussed later in Section 2.2.2.

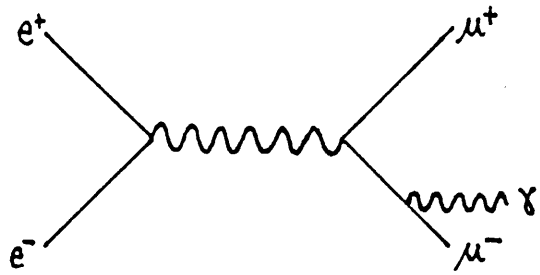

Figure 2.4: Final state radiation diagram

Another QED process of interest is two-photon production of μ-pairs shown in Figure 2.5.

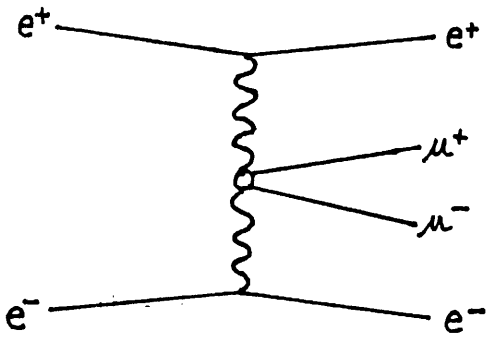

Figure 2.5: Two-photon production of μ-pairs

This is a potential background since the two electrons may remain undetected in the beam-pipe. Consideration of this contamination is discussed later.

The process $e^+e^- \rightarrow l\bar{l}$ is not completely described by the single photon exchange diagram of QED because there is in addition a Z^0 exchange diagram predicted by the electroweak model. This leads to modifications of the differential cross-section (2.2) and the total cross-section (2.3) which are discussed in Section 2.2. However it turns out that at PETRA energies the weak effects do not have a measurable effect on the total cross-section and so deviations from QED are looked for instead.

2.1.1 Deviations from QED

QED is a successful theory only because techniques were developed to handle the infinities in the theory. These infinities arise because of the point-like nature of the interaction. One possible cure is to assume that the leptons are not point-like thereby introducing a fundamental length into the theory [15].

The normal photon propagator term is $-\frac{1}{q^2}$, where q^2 is the four-momentum transfer of the process, related to the Fourier transform of the Coulomb potential $\frac{1}{r}$. If a deviation of the form below is introduced

$$\frac{1}{r} \rightarrow \frac{1}{r}(1 - e^{-\Lambda r}) \tag{2.4}$$

where Λ is related to the the distance at which QED breaks down, R, by $R = \frac{\hbar c}{\Lambda}$. Then the propagator becomes

$$-\frac{1}{q^2} \rightarrow -\frac{1}{q^2} + \frac{1}{q^2 - \Lambda^2} = -\frac{1}{q^2}\left(1 + \frac{q^2}{q^2 - \Lambda^2}\right) \tag{2.5}$$

A heavy photon like particle will introduce a similar modification to the propagator.

In general deviations are looked for by introducing a form factor, $F(q^2)$:

$$F(q^2) = 1 \mp \frac{q^2}{q^2 - \Lambda_{\pm}^2} \tag{2.6}$$

where the $\pm$ denotes a correction that $\begin{matrix}\text{increases}\\ \text{decreases}\end{matrix}$ the cross-section.

The measured differential cross-section for $e^+e^- \rightarrow \mu^+\mu^-$ is now written as a product of the point-like differential cross-section (2.2) and the form factor $F(q^2 = s)$

$$\frac{d\sigma}{d\Omega} = \left(\frac{d\sigma}{d\Omega}\right)_{QED}^{\mu\mu} \mid F(s) \mid^2 \tag{2.7}$$

Since F is independent of angle, equation 2.7 can be integrated over the whole solid angle so that the form factor can be written in terms of $R_{\mu\mu}$

$$R_{\mu\mu} = \frac{\sigma_{meas}}{\sigma_{\mu\mu}} \tag{2.8}$$

where $\sigma_{\mu\mu}$ is the point-like QED cross-section (2.3) above and σ_{meas} is the experimentally measured cross-section. Then, for $\Lambda^2 >> s$,

$$1 - R_{\mu\mu} = \pm\frac{2s}{\Lambda_{\pm}^2} \tag{2.9}$$

A compilation of previous results is shown in Table 2.1. The HRS data were collected at $\sqrt{s} = 29GeV$ and the CELLO, JADE and MARK-J data were collected at an average $\sqrt{s} = 43GeV$ [16].

Final state	Experiment	95% C.L. limits (GeV)	
		Λ_+	Λ_-
e^+e^-	HRS	154	220
	JADE	267	200
	MARK-J	165	235
$\mu^+\mu^-$	HRS	172	172
	CELLO	230	171
	JADE	230	245
	MARK-J	238	174
$\tau^+\tau^-$	HRS	92	246
	JADE	285	210
	MARK-J	235	205

Table 2.1: Results from PEP and PETRA for Λ_+ and Λ_-

These results are all consistent with an upper limit on the lepton charge radius of $10^{-18}m$.

2.2 Electroweak interactions

In the electroweak model described in Chapter 1, there are two lowest order Feynman diagrams describing $e^+e^- \rightarrow \mu^+\mu^-$, a photon exchange diagram and a Z^0 exchange diagram (Figure 2.6).

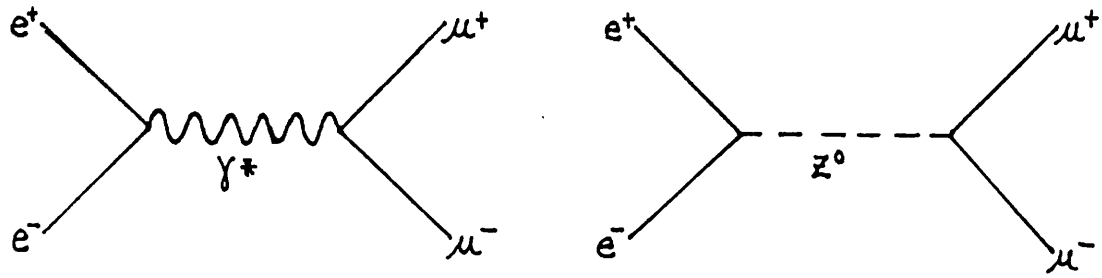

Figure 2.6: Electroweak diagrams for $e^+e^- \rightarrow \mu^+\mu^-$

In Chapter one the neutral current part of the Lagrangian was found to be

$$L_{NC} = -e\bar{\psi}\gamma^\mu Q\psi A_\mu - \frac{g}{cos\theta_w}\bar{\psi}\gamma^\mu((1-\gamma^2)T_3 - 2Qsin^2\theta_w)\psi Z_\mu \qquad (2.10)$$

The Z^0 part can be written in terms of vector and axial-vector coupling constants by defining

$$a_f = 2T_3 \quad v_f = 2T_3 - 4Qsin^2\theta_w \qquad (2.11)$$

so L_{NC} is now

$$L_{NC} = -e\bar{\psi}\gamma^\mu Q\psi A_\mu - \frac{g}{cos\theta_w}\bar{\psi}\gamma^\mu(v_f - a_f\gamma^5)\psi Z_\mu \qquad (2.12)$$

From the neutral current Lagrangian, the following Feynman diagrams, shown in Figure 2.7, are obtained

Lepton	Q	a_l	$v_l(sin^2\theta_w = 0.228)$
$\nu_e\ \nu_\mu\ \nu_\tau$	0	+1	+1
$e^-\ \mu^-\ \tau^-$	−1	−1	−0.088

Table 2.2: Electromagnetic, axial vector and vector couplings of the leptons

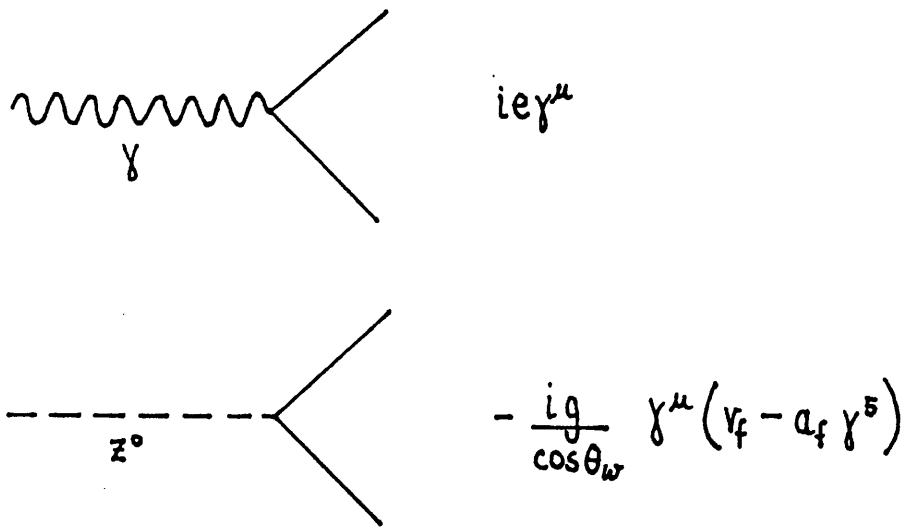

Figure 2.7: Feynman diagrams for neutral current interactions

2.2.1 $e^+e^- \rightarrow \mu^+\mu^-$ in the electroweak model

The lowest cross-section for $e^+e^- \rightarrow \mu^+\mu^-$ in the electroweak model, derived from the Feynman diagrams in Figure 2.7, is:

$$\frac{d\sigma}{d\Omega} = \frac{\alpha^2}{4s}[C_1(1 + cos^2\theta) + C_2 cos\theta] \tag{2.13}$$

where

$$C_1 = Q_e^2 Q_\mu^2 + 2Q_e Q_\mu v_e v_\mu Re(\chi) + (a_e^2 + v_e^2)(a_\mu^2 + v_\mu^2) \mid \chi^2 \mid \tag{2.14}$$

$$C_2 = 4Q_e Q_f a_e a_f Re(\chi) + 8a_e a_f v_e v_f \mid \chi^2 \mid \tag{2.15}$$

where the coupling constant propagator term, χ, can take two forms, χ_1:

$$\chi_1 = \frac{1}{16 sin^2\theta_w (1 - sin^2\theta_w)} \frac{s}{s - M_Z^2} \tag{2.16}$$

where this is known as parameterisation 1.

and χ_2 (parameterisation 2):

$$\chi_2 = \frac{\rho G_F M_Z^2}{8\sqrt{2}\pi\alpha} \frac{s}{s - M_Z^2} \tag{2.17}$$

where ρ is the relative strength of the neutral current and charged current interactions predicted to be one in the minimal $SU(2)_L \times U(1)_Y$ electroweak model.

The two parameterisations are related by:

$$M_Z^2 = \frac{\pi\alpha}{\rho\sqrt{2} G_F sin^2\theta_w (1 - sin^2\theta_w)} \tag{2.18}$$

This is derived from the relation between the Fermi model and the IVB model (1.7), and the various relations among the electroweak model parameters: equations (1.42), (1.44) and (1.46). The ρ parameter was introduced in the Fermi model to measure the difference in coupling strength between the charged current interaction and the neutral current interaction. Paramerisation 2 was originally introduced because G_F and α are precisely measured but now that $sin^2\theta_w$ has been precisely measured in νN scattering experiments and the $W^{\pm}$ and Z^0 have been observed parameterisation 1 is used, except when ρ is determined.

The width of the Z^0, Γ_Z, has been ignored since at PETRA energies

$$\left(\frac{M_Z \Gamma_Z}{s - M_Z^2} \right)^2 \simeq 0.0026$$

for $M_Z = 92 GeV$, $\Gamma_Z = 4 GeV$ and $\sqrt{s} = 35 GeV$.

Integrating over the total solid angle we get the total cross-section relative to the QED cross-section

$$R_{\mu\mu} = C_1 \tag{2.19}$$

However even at the highest PETRA energies ($\sqrt{s} = 45GeV$) the electroweak correction to the QED crossection is very small, $\simeq 0.01$, since the cross-section is sensitive to the electroweak model only through the vector couplings which are small as $sin^2\theta_w$ is near the critical value of 0.25. The variation of the total cross-section with $\sqrt{s}$ for QED and the electroweak model is shown in Figure 2.8.

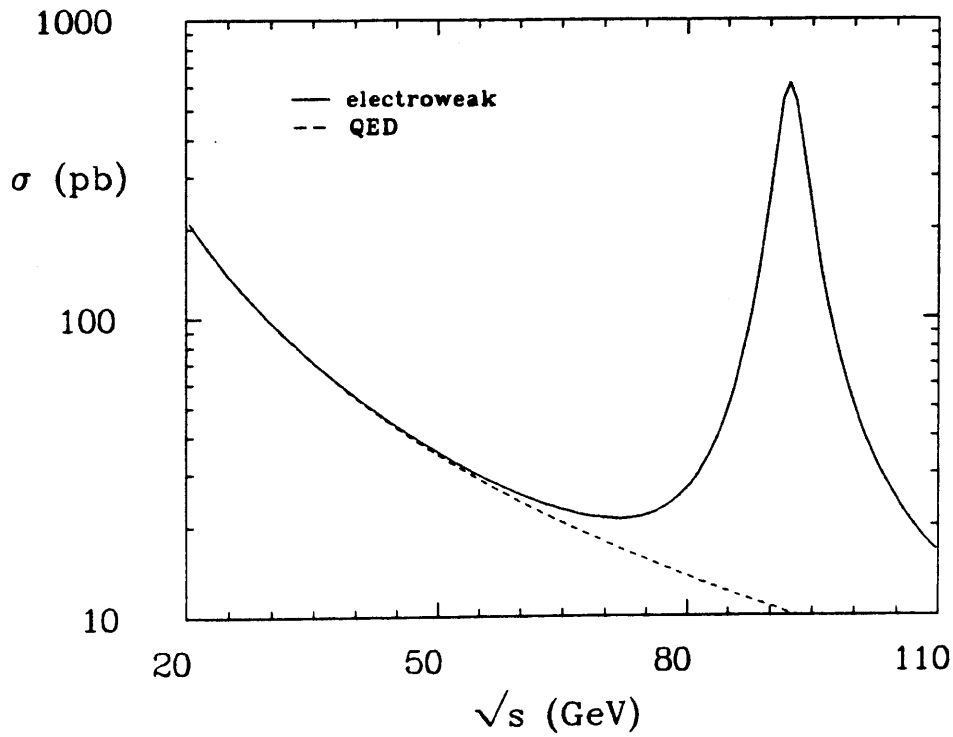

Figure 2.8: The total cross-section predicted by QED and the electroweak model as a function of the centre of mass energy

If we treat the electroweak theory as a deviation from QED using the formalism of Section 2.1.1 we find, using (2.19) and the values from Tables 2.2 and 2.3, that the electroweak theory predicts $\Lambda \sim 1\ TeV$ which is well outside the sensitivity of present experimental results, given in Table 2.1.

An experimentally measureable quantity sensitve to electroweak effects is the charge asymmetry defined as

$$A_{fb} = \frac{\int_0^1 \frac{d\sigma}{dcos\theta} dcos\theta - \int_{-1}^0 \frac{d\sigma}{dcos\theta} dcos\theta}{\int_{-1}^1 \frac{d\sigma}{dcos\theta} dcos\theta} \tag{2.20}$$

so

$$A_{fb} = \frac{3}{8}\frac{C_2}{C_1} \tag{2.21}$$

A_{fb} is shown as a function of $\sqrt{s}$ in Figure 2.9.

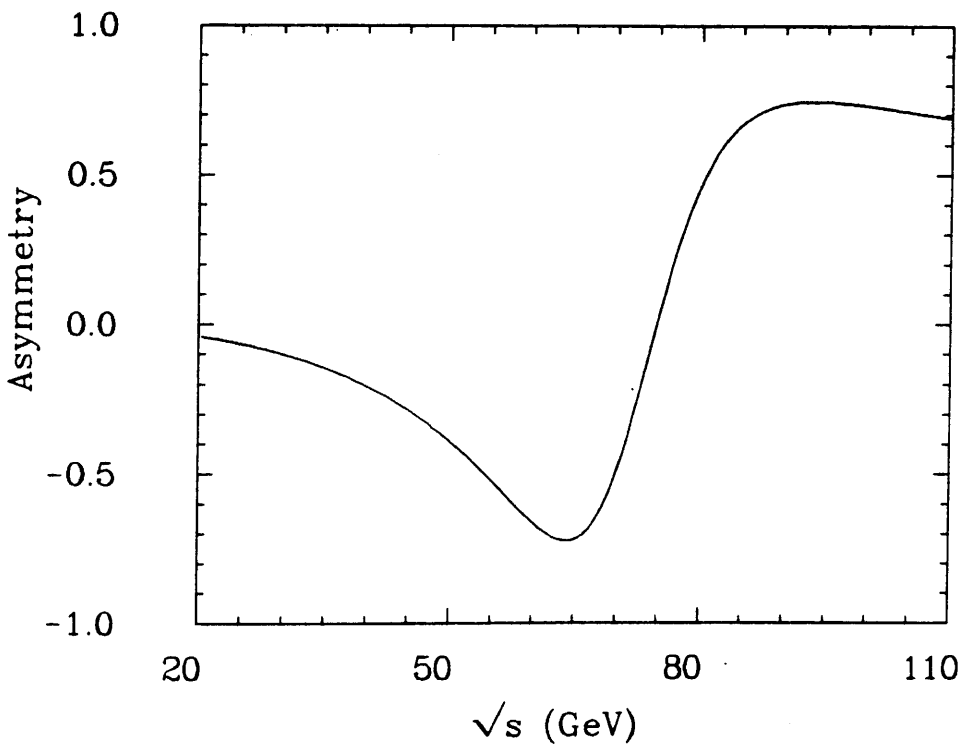

Figure 2.9: The asymmetry as a function of the centre of mass energy

At PETRA energies

$$A_{fb} = \frac{3}{2} a_e a_\mu \chi \tag{2.22}$$

is a good approximation since the χ^2 term is $\simeq 0.005$ at the highest PETRA energies.

A summary of the measured values of the electroweak variables is given in Table 2.3.

Variable	Value	Ref
α	$1/137.03604 \pm 0.00011$	[17]
G_F	$(1.166347 \pm 0.00002) \times 10^{-5}\ GeV^2$	[17]
M_W	$80.8 \pm 1.3\ GeV$	[18]
M_Z	$92.3 \pm 1.6\ GeV$	[18]
$sin^2\theta_w$	0.228 ± 0.004	[19] and [20]

Table 2.3: World averages of important electroweak parameters

Using the values in Tables 2.2 and 2.3 the minimal electroweak model predicts the following asymmetries at $\sqrt{s} = 35\ GeV$

$$A^1_{fb} = -8.94\% \quad A^2_{fb} = -9.65\% \tag{2.23}$$

The two parameterisations give slightly different asymmetries because the calculation was made using the lowest order cross-section. The effects of higher order diagrams such as final state radiation are now discussed.

2.2.2 One-loop corrections to the asymmetry

The asymmetries given above (2.23) are derived from the lowest-order or Born cross-section, (2.13), but if the asymmetries are corrected for the effect of one-loop diagrams then the two asymmetries should agree. The two parameterisations use different sets of physical constants as input so that the renormalisation schemes relevent to the two parameterisations lead to different one-loop corrections. Calculations at the one-loop level have been done in several different renormalisation schemes and give asymmetries that agree provided care is taken in comparing them [21].

The one-loop corrections can be divided into three classes,

- The QED corrections to the photon exchange diagram (reduced QED corrections).
- The QED corrections to the Z^0 exchange diagram.
- Pure weak corrections.

Taken together, the reduced QED corrections and the QED corrections to the Z^0 diagrams are usually known as full QED corrections.

The reduced QED corrections are due to initial and final state radiation, (Figure 2.10b), virtual diagrams such as vertex corrections and two-photon exchange (Figure 2.10c) and the vacuum polarisation of the photon (Figure 2.10d).

The radiative photons from initial and final state radiation are divided into soft and hard photons. The soft photons have very little energy and so cannot be observed, the final state is then assumed to be a μ-pair. The soft photon correction is infra-red divergent but when added to the infrared divergent virtual correction produces a total correction which is infrared finite. The hard photons result in an acollinear $\mu\mu\gamma$ final state. The contamination from $\mu\mu\gamma$ in a sample of $\mu\mu$ events can be reduced by limiting the bremmstrahlung phase space using an acollinearity cut and a muon momentum cut but some $\mu\mu\gamma$ events will remain, increasing the observed cross-section. This is most significant for initial-state radiation since it results in a reduced centre of mass energy for $\mu\mu$.

Interference between the one-photon exchange diagram and the two-photon

exchange diagrams and between initial and final state radiation diagrams leads to a positive angular asymmetry. This arises because one-photon exchange and initial-state radiation produce μ-pairs in a negative charge conjugation state and two-photon exchange and final-state radiation produce μ-pairs in a positive charge conjugation state.

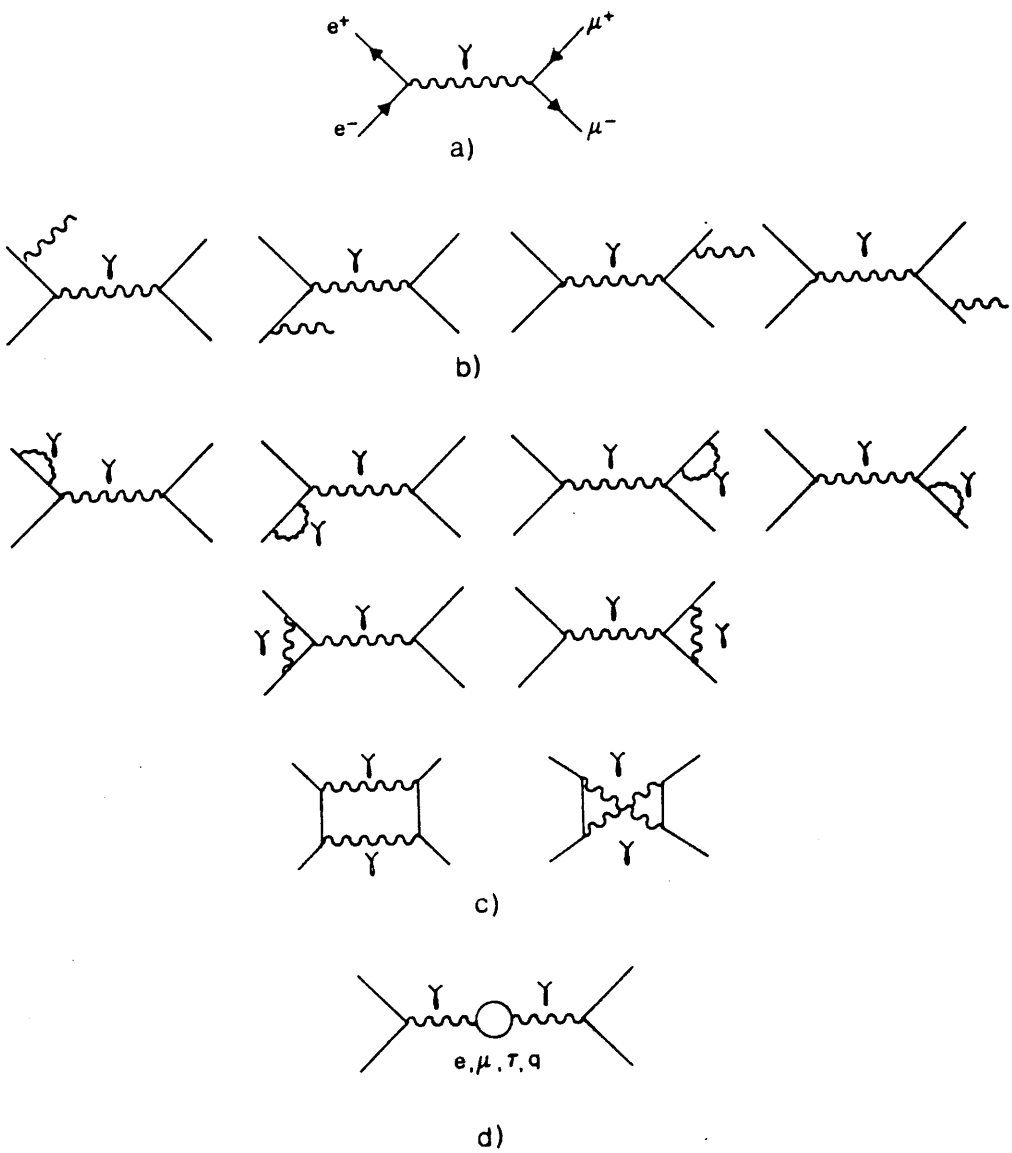

Figure 2.10: The pure QED diagrams

The QED corrections to the Z^0 exchange diagram are shown in Figure 2.11. These are analogous to the reduced QED diagrams in Figure 2.10 except that there is no Z^0 vacuum polarisation. This is included in the set of purely weak corrections.

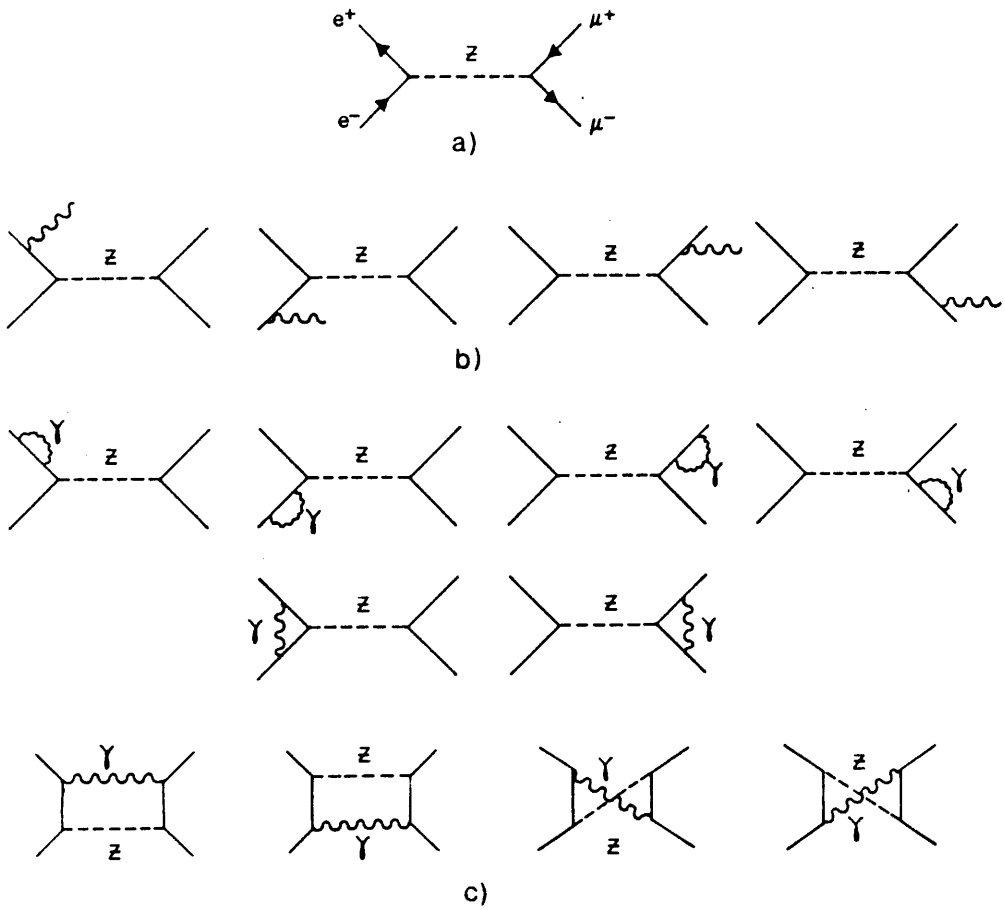

Figure 2.11: The QED corrections to Z^0 exchange

The weak corrections are shown in Figure 2.12. These are diagrams containing the creation and absorbtion of virtual Z^0s, Ws and W^+W^- pairs (Figure 2.12a), two weak boson exchange diagrams (Figure 2.12b), the Z^0 vacuum polarisation (Figure 2.12c) and the $\gamma - Z^0$ mixing diagrams (Figure 2.12d).

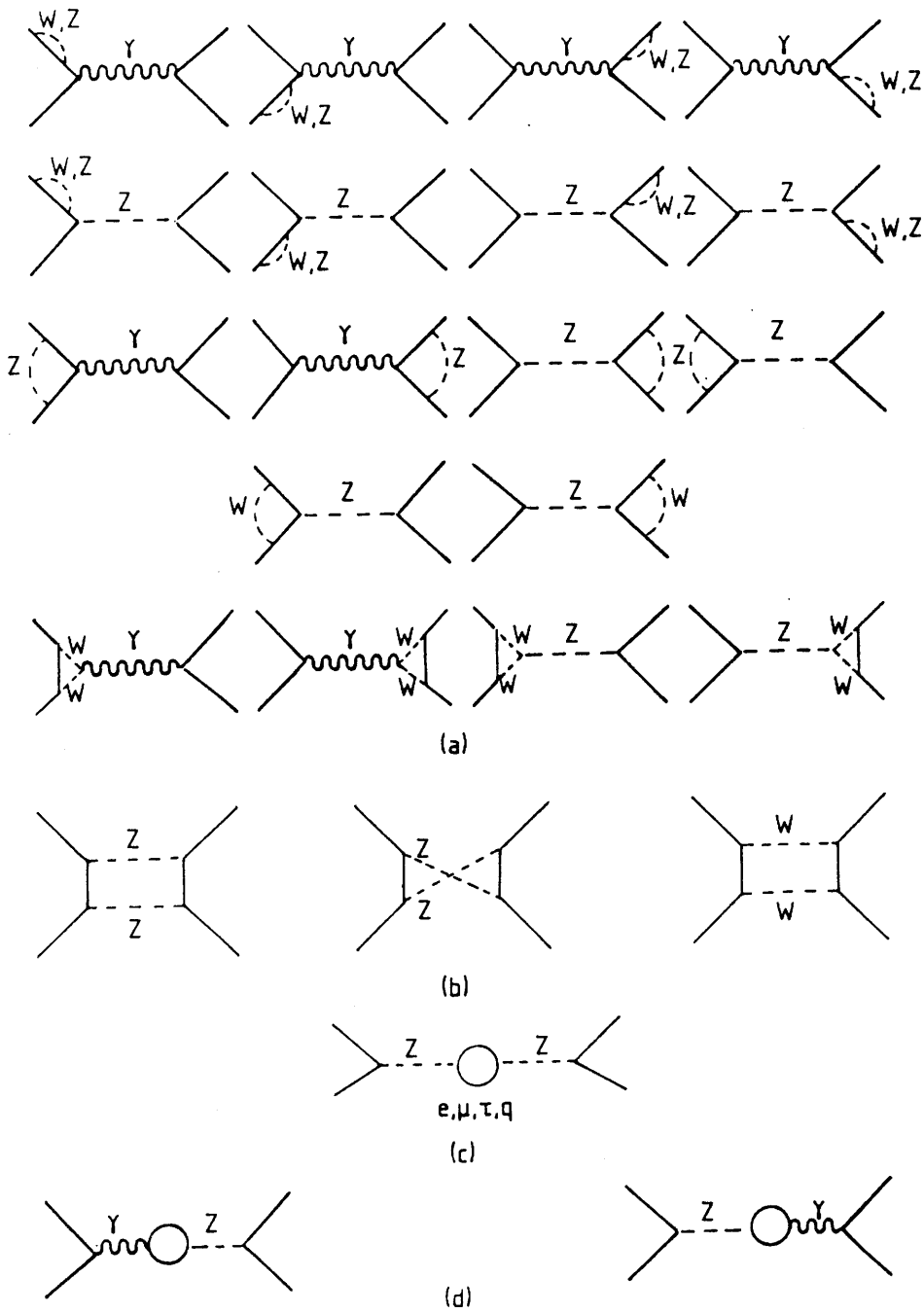

Figure 2.12: The weak diagrams

The corrections are usually calculated in the on-shell renormalisation scheme. The input parameters in this scheme are M_Z , M_W , the Higgs mass M_H, the fermion masses m_f and the fine structure constant in the Thomson limit ($q^2 \rightarrow 0$). This means that $sin^2\theta_w$ is no longer a free parameter but is defined to all orders by

$$sin^2\theta_w = 1 - \frac{M_W}{M_Z}$$

Corrections to parameterisation 1

Bohm and Hollik have shown that for realistic experimental cuts the purely weak corrections, dominated by the Z^0 self-energy [25], cancel the QED corrections to the Z^0 [23]. So data corrected for the reduced QED diagrams shown in Figure 2.10 can be compared directly with lowest order asymmetry A^1_{fb} in (2.23).

Corrections to parameterisation 2

M_W is related to the well measured Fermi coupling constant by (1.7). However the definition of G_F includes all the weak radiative corrections to muon decay. These are dominated by the $W^{\pm}$ self energy. The weak corrections due to the diagrams in Figure 2.12 are dominated by the Z^0 self energy. The corrections from the $W^{\pm}$ self energy and the Z^0 self energy cancel [22] so that the data must be corrected for full QED.

In the above discussion the reduced QED corrections are dependent only on the experimental cuts applied. These corrections can be applied using the Berends, Kleiss and Jadach (BKJ) Monte Carlo [24]. The QED corrections

to the Z^0 diagrams depend on the experimental cuts applied and the values of $sin^2\theta_w$ and M_Z used in the calculations. These corrections can also be calculated using the BKJ Monte Carlo. The weak corrections are sensitive to the input parameters used. The weak corrections are the most interesting since it is here that the electroweak model is tested at the one-loop level. Unfortunately these cannot be tested at PETRA energies and this will be one of the important areas to be studied by LEP and SLC.

The choice of input parameters introduces two potential sources of error; the Higgs mass and the top-quark mass neither of which has been measured. However these do not significantly affect the weak corrections, a variation in M_H from 10 to 1000 GeV resulting in a change in the weak corrections of about -0.1%.

The corrections to the asymmetry in parameterisation 1, in particular the cancellation of the weak corrections and the Z^0 QED corrections for the cuts used in this analysis, were studied using the BKJ Monte Carlo. The cuts applied were: the momenta of both muons must be greater than 0.5*beam energy, $\mid cos\theta \mid \leq 0.85$ and the acollinearity of the muons must be less than 10^o. The input values used were: $sin^2\theta_w = 0.228$ and $M_Z = 92.3\ GeV$. The results are summarised in Table 2.4.

In the Table A^{Born} is the lowest order asymmetry, A^{QED} is the asymmetry corrected for reduced QED diagrams, A^{full} is the asymmetry corrected for full QED diagrams, δA^{QED} is the reduced QED correction, δA^Z is the correction due to the Z^0 QED corrections, δA^{wk} is the purely weak correction taken from

A^{Born}	-8.17%	
A^{QED}	-5.77%	$\delta A^{QED} = +2.40\%$
A^{full}	-5.18%	$\delta A^{Z} = +0.59\%$
A^{1-loop}	-5.78%	$\delta A^{wk} = -0.60$ [23]

Table 2.4: Corrections to the asymmetry in parameterisation 1

[23] and corrected for the $cos\theta$ acceptance and A^{1-loop} is the asymmetry corrected to the 1-loop level. The data in Table 2.4 shows that to compare the measured asymmetry with the the theoretical asymmetry calculated using parameterisation 1 we need only correct the data for the reduced QED diagrams.

A similar study was made of the corrections applied to asymmetry in parameterisation 2 and the results are shown in Table 2.5.

A^{Born}	-8.81%	
A^{QED}	-6.41%	$\delta A^{QED} = +2.40\%$
A^{full}	-5.82%	$\delta A^{Z} = +0.59\%$
A^{1-loop}	-5.82%	$\delta A^{wk} \sim 0$[22]

Table 2.5: Corrections to the asymmetry in parameterisation 2

From the Table 2.5 we see that to compare the theoretical asymmetry with the measured asymmetry, which has been corrected for the reduced QED diagrams, we must add δA^{Z}.

Comparing the 1-loop level asymmetries of the two parameterisations we see that they are in good agreement.

2.3 Review of current results

Asymmetry measurements have been made for both $e^+e^- \rightarrow \mu^+\mu^-$ and $e^+e^- \rightarrow \tau^+\tau^-$ at PEP and PETRA over a large range of centre of mass energies. The results are shown in Table 2.6 (these results are taken from [26] and [19]). The predicted asymmetry is calculated using parameterisation 1 with M_Z =92.3 GeV and $sin^2\theta_w$ =0.23. and the data have been corrected for reduced QED.

Experiment	$\sqrt{s}(GeV)$	$A_{\mu\mu}$ (%)	$A_{\tau\tau}$ (%)	Theory (%)
MARK-2	6.0	-0.30 ± 1.0		-0.2
JADE	13.9	2.70 ± 4.9		
MARK-J	14.0	5.30 ± 5.0		
Averaged	14.0	4.0 ± 3.6		-1.2
CELLO	22.0		1.1 ± 7.8	
JADE	22.0	-10.6 ± 6.4		
MARK-J	22.5	-4.3 ± 6.1		
Averaged	22.0	-7.3 ± 4.5	1.1 ± 7.8	-3.2
HRS	29.0	$-4.9 \pm 1.5 \pm 0.5$	$-4.4 \pm 1.4 \pm 0.5$	
MAC	29.0	$-5.9 \pm 0.7 \pm 0.2$	$-5.5 \pm 1.2 \pm 0.5$	
MARK-2	29.0	-7.1 ± 1.7	-4.2 ± 2.0	
Averaged	29.0	-5.9 ± 0.6	-4.9 ± 0.9	-5.8
CELLO	34.2	-6.4 ± 6.4	$-10.30 \pm 5.2 \pm 1.0$	
JADE	34.4	$-11.1 \pm 1.8 \pm 1.0$	$-6.0 \pm 2.5 \pm 1.0$	
MARK-J	34.6	$-11.7 \pm 1.7 \pm 0.5$	$-8.6 \pm 3.7 \pm 1.5$	
PLUTO	34.7	$-13.2 \pm 2.8 \pm 1.0$	$-5.9 \pm 6.8 \pm 1.5$	
TASSO	34.5	$-9.1 \pm 2.3 \pm 0.5$	$-4.9 \pm 5.3 \pm 1.3$	
Averaged	34.5	-10.9 ± 1.1	-6.8 ± 1.9	-8.6
CELLO	38.3	$-3.9 \pm 6.5 \pm 0.7$	$-13.5 \pm 6.9 \pm 1.0$	
JADE	38.0	-9.7 ± 5.2	$7.5 \pm 6.3 \pm 1.0$	
MARK-J	39.1	-10.0 ± 4.1		
TASSO	38.3	1.6 ± 8.6		
Averaged	38.7	-7.6 ± 2.8	-1.9 ± 4.7	-11.2
CELLO	43.8	$-18.9 \pm 4.5 \pm 0.7$	$-22.3 \pm 4.1 \pm 1.0$	
JADE	43.7	-19.1 ± 3.1	$-17.0 \pm 3.6 \pm 1.0$	
MARK-J	44.1	-16.0 ± 3.0	-12.8 ± 7.0	
TASSO	43.7	-18.4 ± 4.3		
Averaged	43.8	-17.9 ± 1.8	-18.3 ± 2.7	-15.2

Table 2.6: Results from PEP and PETRA for $A_{\mu\mu}$ and $A_{\tau\tau}$

Using parameterisation 1 and setting; $a_e a_\mu = 1$ and $M_Z = 92.3\ GeV$, a combined fit to all the muon data has been made to determine $sin^2\theta_w$ [19], giving

$$sin^2\theta_w = 0.200 \pm 0.017$$

Using the muon and tau data [19],

$$sin^2\theta_w = 0.215 \pm 0.017 \pm 0.01$$

The muon and tau data give a $sin^2\theta_w$ which is in excellent agreement with the values of $sin^2\theta_w$ measured in other processes [20]. The agreement between experiments measuring lepton-lepton, lepton-hadron and hadron-hadron processes over a very large Q^2 range is shown in Figure 2.13.

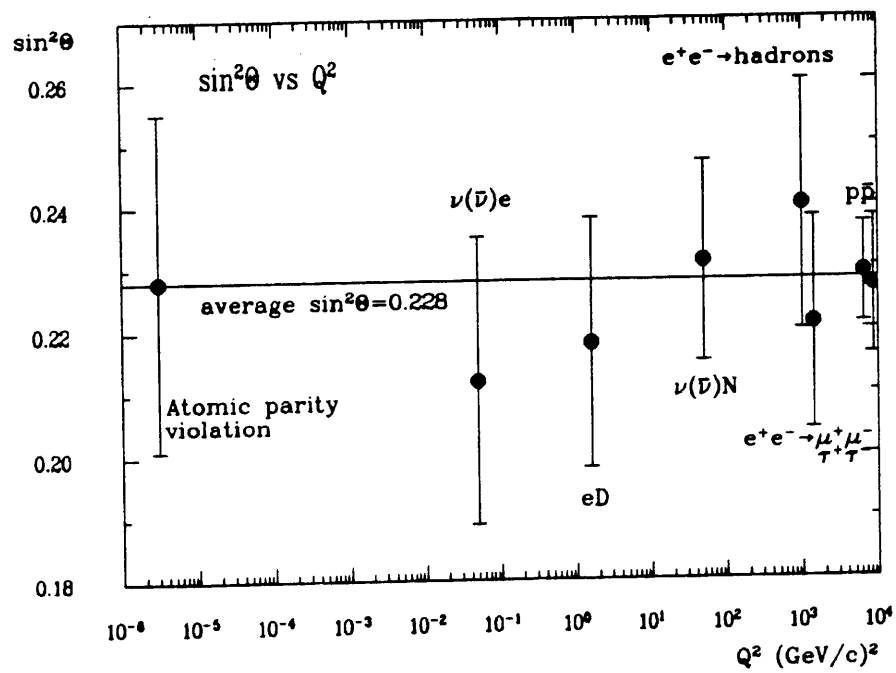

Figure 2.13: $sin^2\theta_w$ against Q^2 for different processes

Using parameterisation 2 with $\rho = 1$ and $M_Z = 93\ GeV$, $a_e a_\mu$ can be calculated. A compilation of data is given in Table 2.7 taken from [26].

	$\sqrt{s}\ (GeV)$	$a_e a_\mu$
PEP	29.0	0.99 ± 0.11
PETRA	34.5	1.24 ± 0.13
PETRA	38.6	0.85 ± 0.26
PETRA	43.9	1.13 ± 0.12
Average		1.10 ± 0.07

Table 2.7: Results from PEP and PETRA for $a_e a_\mu$

The average for $a_e a_\tau$ is

$$a_e a_\tau = 0.84 \pm 0.10$$

To test universality we can look at the ratio $\frac{a_\mu}{a_\tau}$

$$\frac{a_\mu}{a_\tau} = 1.31 \pm .0.18$$

This supports universality.

Alternatively setting $a_e a_\mu = 1.0$ we can determine ρ

$$\rho = 1.11 \pm 0.07 \quad for\ \mu\mu$$

$$\rho = 1.02 \pm 0.05 \quad for\ \mu\mu\ and\ \tau\tau$$

Both these result are in good agreement with the minimal electroweak model which contains only Higgs doublets.

Chapter 3

Experimental Apparatus

3.1 PETRA

The e^+e^- collider PETRA (Positron Elektron Tandem Ring Anlage) at DESY, Hamburg started producing collisions in November 1978 and since then has operated at beam energies rising from 11 GeV, in 1979, to a maximum of 23.6 GeV in 1985.

The injection scheme starts with electrons being emitted from an electron gun, accelerated to 40 MeV in LINAC 1, and passed to the synchrotron (DESY) where they are accelerated to 7 GeV, they are then injected into PETRA. Positrons are produced by firing electrons at a metal target and are accelerated to 400 MeV in LINAC 2. The positrons are then stored in the Positron Intensity Accumulator, when a sufficient number have been collected they are injected into the synchrotron and accelerated to 7 GeV. The positrons are then injected into PETRA and accelerated simultaneously with the electrons. Usu-

ally injection and acceleration to the final beam energy takes approximately thirty minutes.

PETRA consists of eight straight sections and eight curved sections (see Figure 3.1). There are four long straight sections where the accelerating R.F. cavities are located and four short sections where the experimental areas are situated. These contain the four PETRA experiments: TASSO, MARK J, JADE and CELLO. The eight curved sections consist of quadrupole, sextupole and dipole bending magnets. The quadrupole magnets prevent lateral bunch dispersion and the sextupoles correct the orbits of off-momentum particles. Longitudinal bunch dispersion is prevented by synchrotron radiation and the acceleration system. Some important PETRA parameters are given in Table 3.1.

Luminosity

The rate of an interaction having cross-section σ is,

$$r = L\sigma \tag{3.1}$$

where L is the luminosity of the collider: the number of interactions per unit time per unit cross-section. L is determined from

$$L = fb\frac{n^+n^-}{A} \tag{3.2}$$

where $n^+(n^-)$ are the number of positrons (electrons) per bunch, b is the number of bunches, f is the rotation frequency and A is the common geometrical cross-section of the bunches. This gives a typical PETRA luminosity of $9 \times 10^{-31} cm^{-2} s^{-1}$.

Circumference	2304m
Injection energy	6-7 GeV
Beam energy	5-23 GeV
Energy spread	$2.3 \times 10^{-5} * E_{beam}$
Luminosity	max. $17 \times 10^{30} cm^{-2} s^{-1}$
Beam lifetime	3-5 hrs
Number of bunches	2 per beam
Bunch length	10 mm rms
Bunch width	0.7 mm
Bunch height	0.1 mm
Bunch crossing time	$3.8 \mu s$
Beam current	20 mA max.
RF	500 MHz
RF power	4 MW
Klystrons	8
RF cavities	60

Table 3.1: PETRA parameters

The integrated luminosity l,

$$l = \int L dt$$

gives the total number of interactions per unit cross-section during a running period. Using this, the cross-section of a process can be determined from the number of observed events using,

$$N = l \epsilon \sigma \tag{3.3}$$

where ϵ is the detection efficiency.

The luminosity used in this analysis was found to be $85.3 \pm 1.1 \pm 4.3\ pb^{-1}$, where the first error is statistical and the second systematic, from a study of $e^+e^- \rightarrow \gamma\gamma$ [27]. This is in good agreement with the luminosity of $84 \pm 4\ pb^{-1}$, where only the systematic error is given, obtained from a study of Bhabha events in the forward detectors.

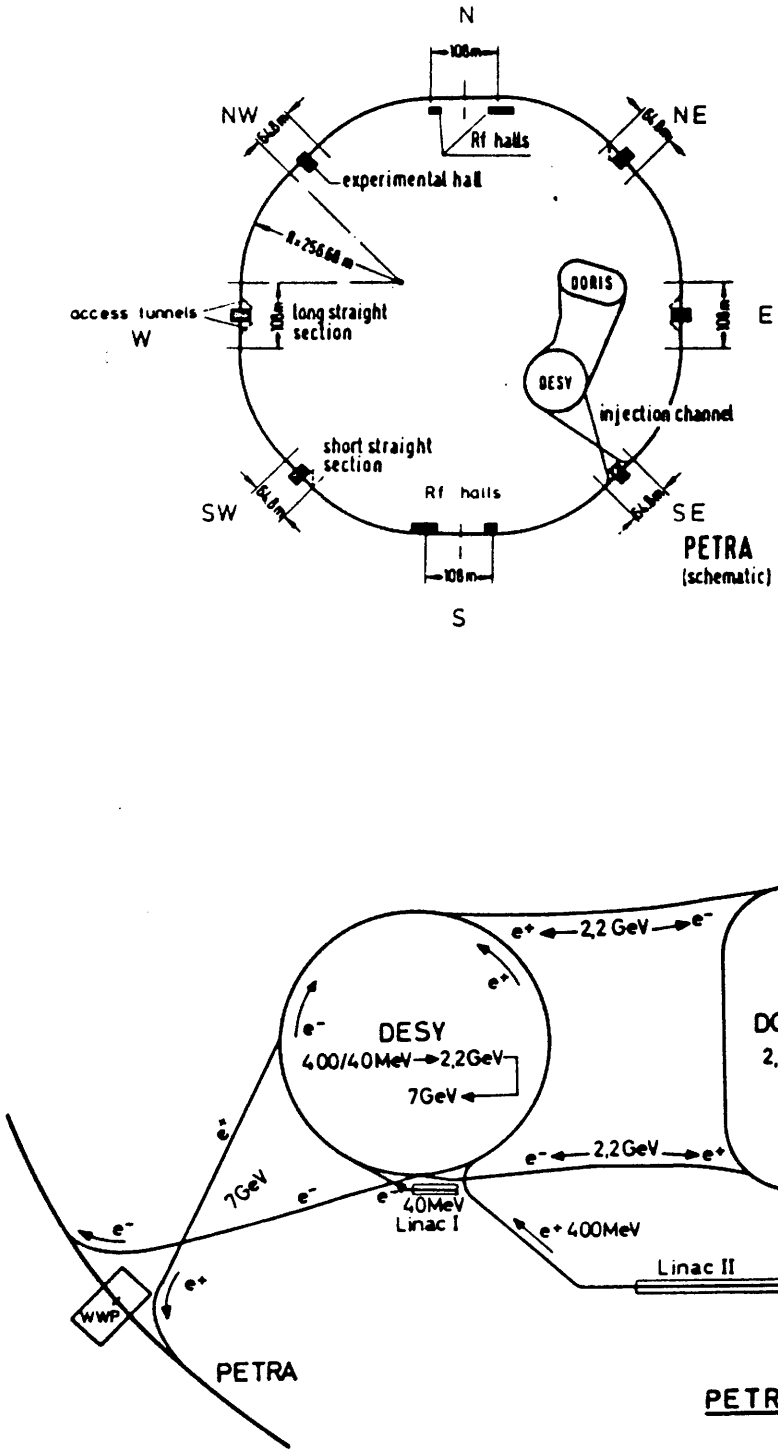

Figure 3.1: PETRA and the PETRA experiments

3.2 CELLO

The range of physics that can be studied at e^+e^- colliders is very large e.g. jet physics, two photon physics, electroweak physics and searches for new particles; therefore detectors for e^+e^- colliders are designed to cover as much of this range as possible. With this in mind CELLO [28] was designed as a general purpose magnetic detector covering a large fraction of the solid angle, optimised for photon and electron identification at the expense of extensive particle identification. The detector is shown in Figure 3.2 and the polar acceptance of CELLO is shown in Figure 3.3.

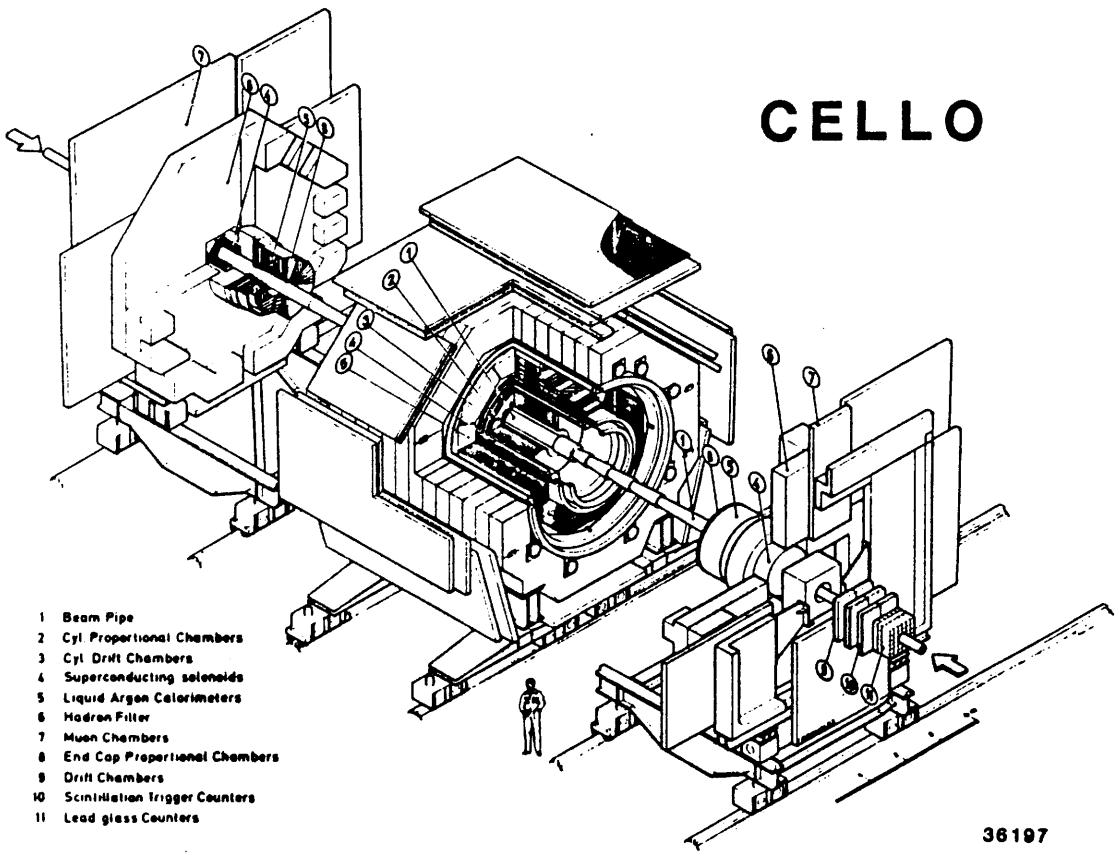

Figure 3.2: The CELLO detector

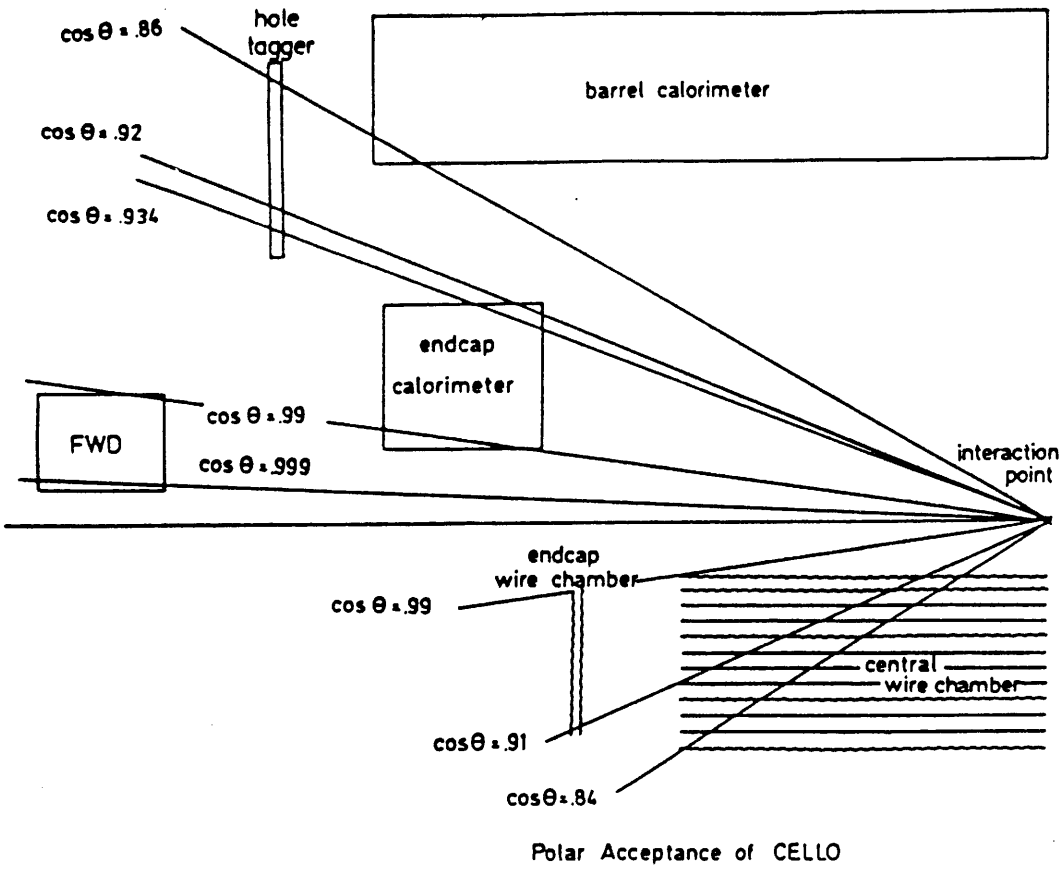

Figure 3.3: The Polar acceptance of CELLO

The main components are: a central tracking detector providing particle tracking and momentum measurement, enclosed in a solenoidal magnet giving a $1.3T$ axial magnetic field, a fine grain lead liquid argon calorimeter for electromagnetic calorimetery and electron identification and large planar drift chambers located outside the iron return yoke for muon identification. The detector is triggered by a combination of neutral and charged triggers. The components are further discussed below and Table 3.2 summarises their important properties. In Table 3.2; BPCs are beam pipe drift chambers, CDCs are cylindrical drift chambers, CPCs are cylindrical proportional wire chambers, PWCs are planar wire chambers, X_0 is a radiation length, DCs are drift chambers, scint is scintillator and Pb-gl is lead glass.

Detector Component	Number of Modules	Solid angle $\frac{\Delta\Omega}{4\pi}$	Typical Dimensions (cm)	Important Properties
Central Tracker	2 BPCs		Length 220	$\sigma_{rz} = 440\mu m$
	5 CPCs	0.87	Radius 10.9	$\sigma_{r\phi} = 170\mu m$
	7 CDCs		to 70	$\frac{\sigma_p}{P} = \frac{0.02\ P\ (GeV)}{\beta}$
Endcap	8 PWCs	0.10	$z = \pm 140.5$	Thickness=0.02 X_0
Tracker			$z = \pm 142.5$	
Central Solenoid	1		Length 400 Radius 80	Superconducting Thickness=0.59X_0
Calorimeter	16 around the central tracker + 4 endcaps	0.86 0.07	Length 400 radius 80	$\frac{\sigma_E}{E} = .05 + \frac{0.10}{\sqrt{E(GeV)}}$ $\sigma_\phi = \sigma_\theta$ =4mrad typically
Muon Chambers	32	0.92	200 × 300 to 300 × 400	$\sigma_{x,y} = 6mm$
Forward Detector	24 DCs 96 scint 112 Pb glass Shower Counters			$\sigma = 300\mu m$ $\frac{\sigma_E}{E} = \frac{0.05}{\sqrt{E(GeV)}}$

Table 3.2: Main components of the CELLO detector

3.2.1 The CELLO Coordinate System

The coordinate system is shown in Figure 3.4. The x-y plane is called the $R\Phi$ projection and the plane containing the beam axis and the initial track momentum is called the RZ projection. The origin is located at the interaction point which is determined on run by run basis from the vertices of colinear Bhabha events reconstructed with the GLOFIT program described in Chapter 4. The distances from the vertex in the $R\Phi$ plane and the RZ plane are $\delta R\Phi$ and δRZ respectively.

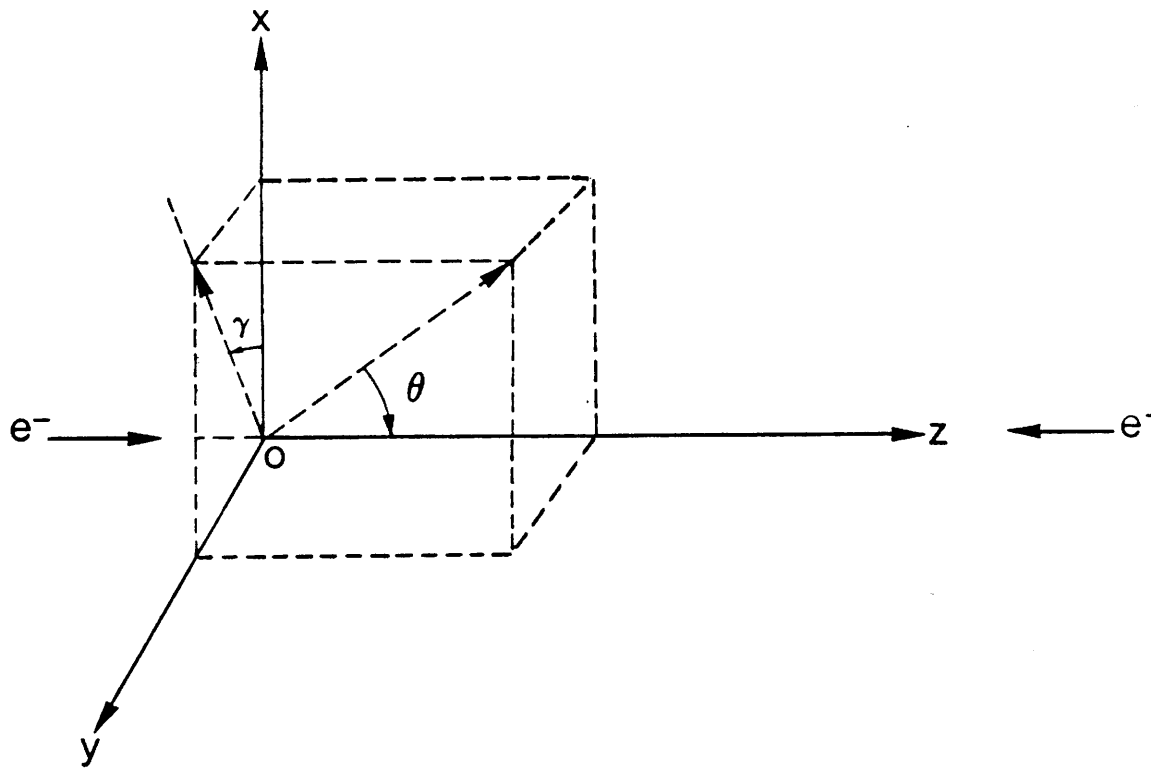

Figure 3.4: The CELLO coordinate system

3.2.2 The Central Detector

The central tracking detector was designed to fulfill the following objectives.

- Stable operation in a strong axial magnetic field.
- Accurate position measurement in the $R\Phi$ and RZ projections for tracking and momentum determination.
- High resolution so that nearby tracks in multijet events can be distinguished.
- Information for a fast charged trigger.

To fulfill these objectives a set of interleaved cylindrical proportional wire chambers (CPCs) and cylindrical drift chambers (CDCs) concentric with the beam axis were chosen. Two additional drift chambers are located just outside the beam-pipe (BPCs). The layer structure is shown in Figure 3.5 and summarised in Table 3.3. The CPCs provide trigger information, space point and precise RZ measurment. The BPCs and CDCs provide good $R\Phi$ and momentum measurement.

Layer	Type	Radius (cm)	Number of anode wires or drift cells	Wire spacing or drift cell width (mm)	Number of Cathodes	
					90^o	30^o
1	BPC	10.9	128	5.35	–	
1	BPC	11.4	128	5.35	–	
3	CPC	17.0	512	2.09	258	256
4	CPC	21.0	512	2.58	228	256
5	CDC	25.5	104	15.41	–	
6	CDC	30.4	128	14.92	–	
7	CPC	35.7	1024	2.19	366	512
8	CDC	40.2	168	15.03	–	
9	CDC	45.1	192	14.76	–	
10	CDC	50.0	208	15.10	–	
11	CPC	55.3	1536	2.26	420	768
12	CDC	59.8	256	14.68	–	
13	CDC	64.7	256	15.88	–	
14	CPC	70.0	1536	2.86	494	768

Table 3.3: Layer structure of central tracker

The Cylindrical Proportional Wire Chambers

There are 5 CPCs [29] each with axial anode wires and finely segmented cylindrical cathode strips at 90^o and 30^o with respect to the anode wires in an 80% argon, 20% isobutane and 0.18% freon gas mixture. Analogue measurement of the induced charge on the strip is done for each of the cathode strips. The Z

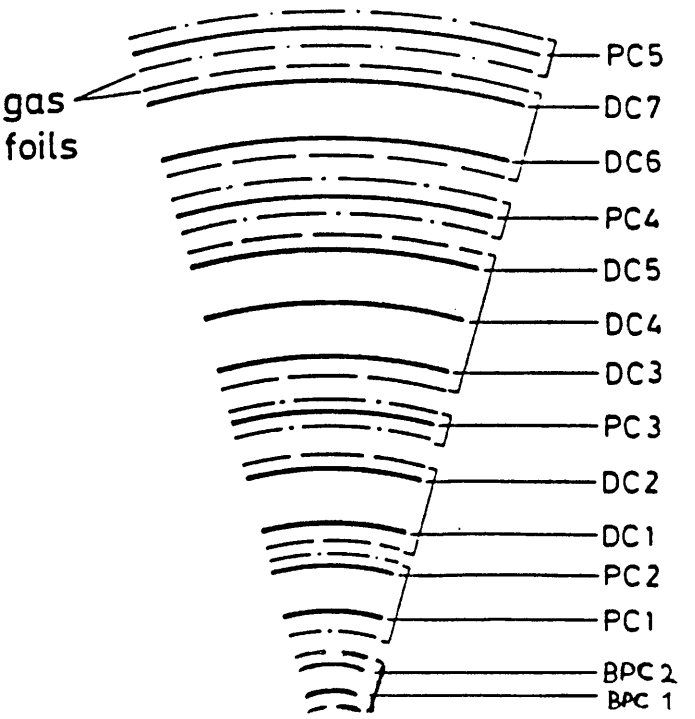

Figure 3.5: Layer structure of the central tracker

coordinate is determined from the centroid of the induced charge distribution and has a precision of $\sigma_z = 440\mu m$. The charge correlation between the 30° and the 90° anodes is used to disentangle overlapping cathode clusters, allowing nearby tracks to be resolved. Space points can then be found by combining the cathode and anode information. The information from the anodes and the 90° cathodes is used in the charged trigger.

The Cylindrical Drift Chambers

The CDCs [30] complement the CPC's by determining the $R\Phi$ coordinates with good precision. They are arranged in an open-cell drift structure which consists of drift cells approximately 15mm across separated electrostatically by a triplet of potential wires as shown in Figure 3.6. Minimising the number of potential wires reduces multiple scattering. The small drift cell size provides

good track resolution in multijet events and allows single hit electronics to be mounted directly on the chambers, as the probability of more than one track passing through a drift cell is negligible. Each sense wire has an amplifier/ discriminator, which is connected by long cables to CAMAC TDC's. These TDC's have a total range of 810ns and are stable to better than 1% with a nonlinearity of less than 3ns. A gas mixture of 50% argon and 50% ethane is used [31].

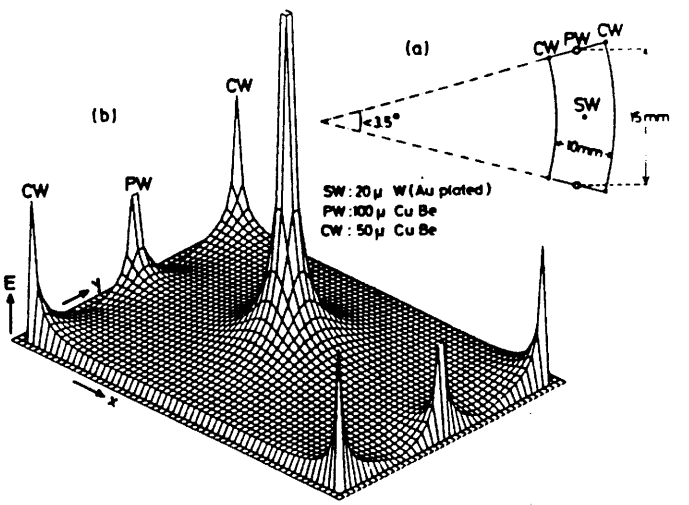

Figure 3.6: Drift cell geometry (a) and electric field distribution (b) inside a drift cell.

In a large magnetic-field the drift process is affected by the electrons drifting along the direction of the Lorentz force [32], which can be as much as 50° or 60° relative to the electric field lines, and their drift velocity can be reduced by a factor which is strongly dependent on the electric field strength. These effects lead to non-linearities in the space-time relationship which were parameterised using a computer simulation. Using this parameterisation tracks can be reconstructed which have a point resolution in $R\Phi$ of $170\mu m$. This accuracy

is dominated by systematic effects such as the quantisation of the TDC's, wire displacement due to electrostatic and gravitational forces and alignment errors.

The Beam-Pipe Chambers

These are two layers of drift tubes located just outside the beam-pipe and are used to get precise vertex information and improve the momentum resolution [33]. The use of individual drift tubes instead of the open layer structure used in CDCs isolates damage due to beam associated backgrounds. They operate in the same gas mixture as the CDCs and also require a parameterisation of their space-time relationship due to the difference in direction between the Lorentz force and the electric force.

The drift cells overlap, as shown in Figure 3.7. This can be used in conjunction with the outermost DCs to reject events not in coincidence with the beam crossing signal. This is very important in rejecting cosmic ray events and is discussed more fully further on.

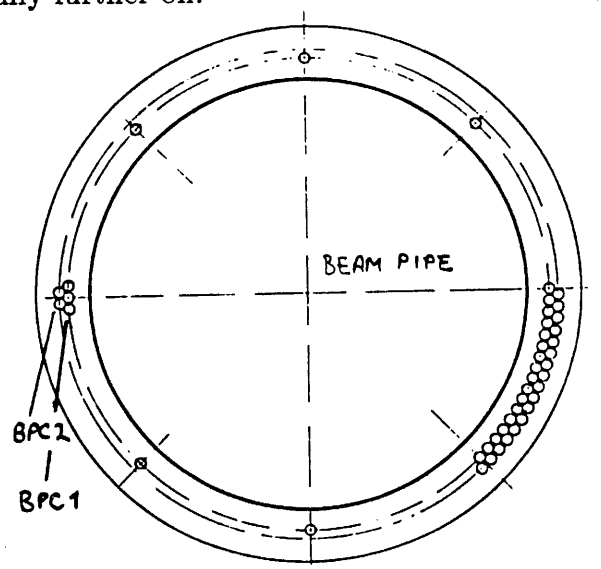

Figure 3.7: Construction of the beampipe chambers

If a track is required to pass through 12 layers of the central tracker then the solid angle coverage is 87% of 4π (or $\cos\Theta \leq 0.87$). To provide good tracking of tracks in the extreme forward or backward regions (for Bhabhas and two-photon physics) there are multiwire proportional chambers located at the ends of the detector (see fig 3.2). This increases the solid angle coverage of 12 tracking layers to 92% of 4π.

There are four identical units, semi-circular in shape, each unit consisting of two electrically separated chambers, shown in Figure 3.8 One chamber of each unit is located at $z = \pm 1405mm$ with anode wires parallel to the x-axis to provide y-coordinate measurement. The other chamber is located at $z = \pm 1425mm$ with anode wires orientated to measure the x-coordinate. One set of cathodes is divided into sections of $\frac{180^o}{32}$ in Φ and the other is divided into rings concentric with the beam axis. Each ring corresponds to a Θ interval subtended by a 90^o cathode strip in the central tracker.

3.2.3 The Superconducting Solenoid

The central tracker is mounted inside a superconducting solenoid which provides an uniform axial magnetic field of 1.3T [34] . The solenoid is designed with a wall thickness of $0.5X_0$ radiation lengths including the cryostat and insulating material. This design reduces the probability of photons or electrons showering which would reduce the spatial and energy resolution of the calorimeter.

This design philosophy of minimising the amount of material between the

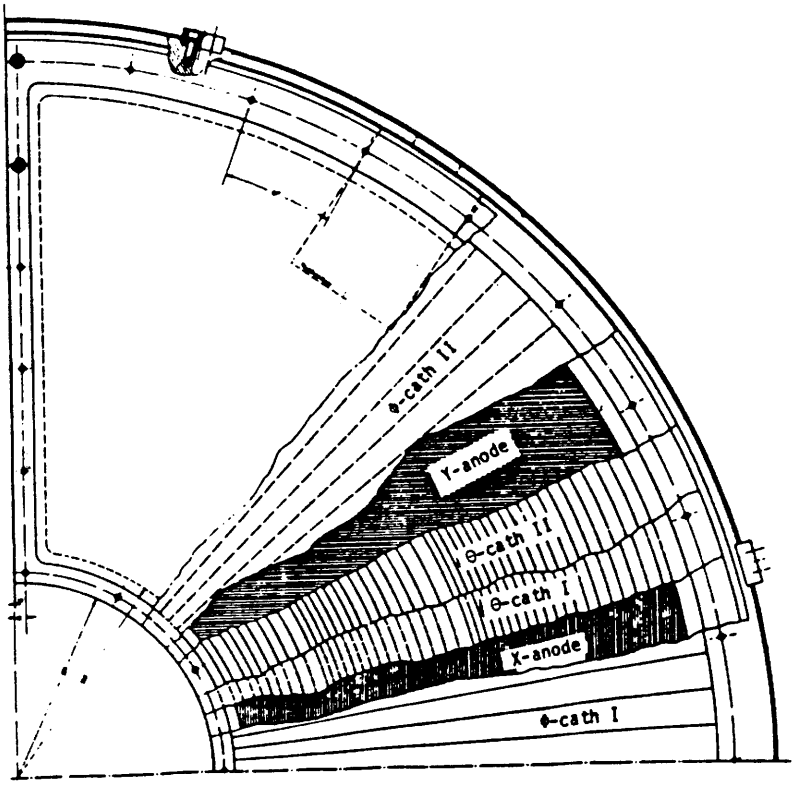

Figure 3.8: Construction of the endcap tracker

interaction point and the calorimeter to reduce showering meant that no scintillators were placed around the central tracker to provide time of flight information.

3.2.4 Lead liquid-argon calorimeter

The design objectives of the electromagnetic calorimeter were,

- Good electron-hadron separation.
- Good detection efficiency, energy resolution and spatial resolution for low energy photons over the entire solid angle.
- Provide information for a neutral trigger.

The resulting design was a barrel shaped lead liquid-argon calorimeter with endcaps covering in total 96% of 4π [35].

The barrel part is contained in a $25m^3$ cryostat and consists of 2×8 stacks, mirror symmetric about $z = 0$ and octagonally symmetric in $R\Phi$. Each of the 16 stacks has a trapezoidal cross-section with a length of $2m$ and a width of $85cm$ in the first layer and $121cm$ in the last layer as shown in Figure 3.9. The stacks are $43cm$ or 20 radiation lengths deep which is enough to contain electromagentic showers even at the highest PETRA energies.

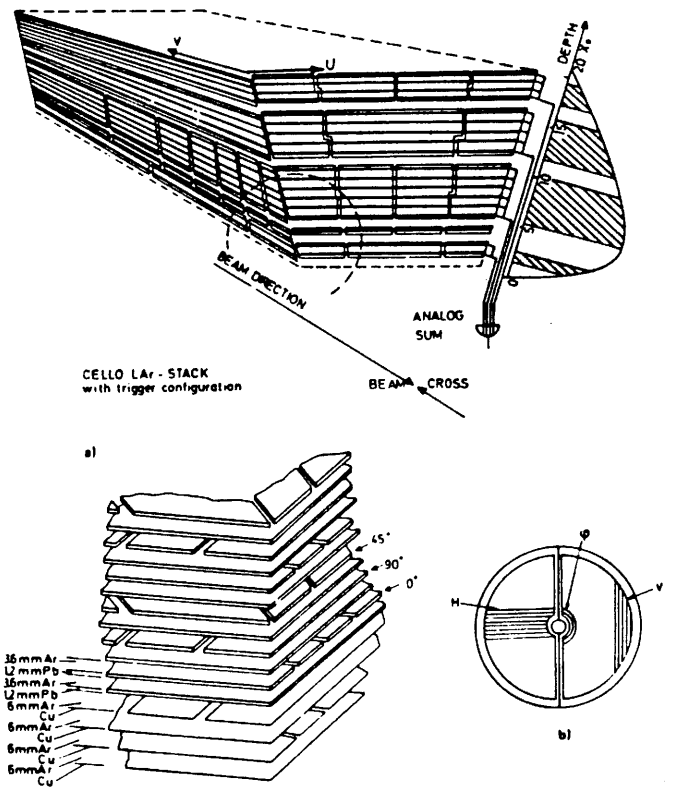

Figure 3.9: (a) A calorimeter stack and the neutral trigger (b) The layer structure of the barrel and (c) the layer structure of the endcaps.

A layer scheme of lead strips $1.2mm$ thick alternating with continuous lead plates, also $1.2mm$ thick, with a gap of $3.6mm$ is used to obtain good spatial

resolution. The strips are held at a positive high voltage relative to the plates. The strips are orientated at 0^o relative to beam axis giving a Φ measurement (the U-strips), 90^o relative to the beam giving a Θ measurement (the W-strips) and 45^o relative to the beam to resolve ambiguities (the V-strips). In front of each stack there are two $\frac{dE}{dx}$ gaps consisting of copper foil glued to epoxy plates with a gap width of $6mm$.

The wiring optimises the spatial resolution while minimising the number of electronic channels to be read out. Laterally the strips are grouped into $20mrad$ bins and perpendicularly all strips are read out. Deep inside the calorimeter coarser strips are used since good spatial resolution is not so important. To obtain good $\pi - e$ separation seven samplings in depth are taken for the U and W-strips and 5 samplings in the V-strips. The wiring is shown in Figure 3.10. Pulse height sums for the neutral trigger, discussed below, are made using the U-strip pulse heights and the layer 4 V-strip pulse height.

To minimise gaps and dead material the stacks are mainly supported from the rear resulting in the overall dead area being less than 3.5% of the total solid angle covered by the barrel.

The endcaps consist of two cylindrical cryostats, surrounding the beam, see Figure 3.2, each containing two half-cylindrical modules. Each module contains 42 layers of lead strips alternating with continuous plates. The strips are alternatively vertical, horizontal and circular. The radial extension is $23 - 66mm$, covering the solid angle region $0.92 \leq |cos\Theta| \leq 0.99$. In front of each of the modules there are layers of copper foils glued to epoxy plates for $\frac{dE}{dx}$ measure-

ments. The total thickness corresponds to $21X_0$ and the number of electronic channels per module is 368.

The analogue signals from the 10688 electronic channels are processed by pre-amplifiers attached to the cryostat. The signals are then sent to the counting house where they are amplified again and digitised. The final signals are organised on a readout card where channels with signals below a noise threshold are suppressed. As minimum ionising particles deposit about four times more charge than noise levels they are readily detected.

Layer	U	V	W	Total
7	32	12	12	56
6	16	12	12	40
5	16	24	48	88
4	16	24	–	40
3	32	56	48	136
2	32	64	40	136
$\frac{dE}{dx}$	32	48	–	80
Total	176	240	160	576

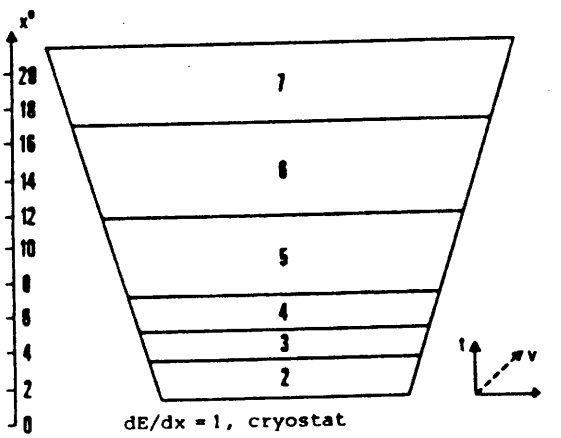

Figure 3.10: Wiring scheme for Lead liquid-argon calorimeter

3.2.5 The Holetagger

The holetagger provides crude calorimetery in the gap between the barrel and the endcap calorimeters, which can be seen in Figure 3.3. It consists of a lead-scintillator sandwich hanging on the inner side of the detector doors as shown in Figure 3.11. The scintillators are readout to photomultipliers located outside the iron return yoke via wavelength shifters and light-guides. On each door there are eight scintillator modules which overlap to avoid dead areas and have octagonal symmetry. In addition there is one module located in the chimney where there is a hole in the calorimetry due to liquid argon supply lines. The signals from the photomultipliers are digitised and are used to provide a neutral energy trigger in this region.

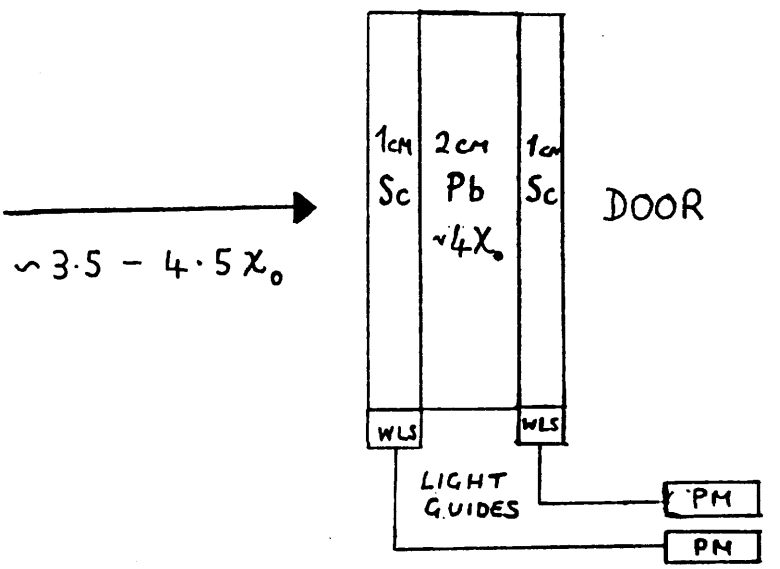

Figure 3.11: The holetagger

3.2.6 The Muon Chambers

There are 32 large proportional chambers [36] located outside the iron return yoke of the magnet, which acts as a hadron filter being $5-8$ interaction lengths deep. As the muons undergo multiple scattering in the iron high precision in the position measurement is not required but to study muons in multihadronic events both coordinates in the chamber plane must be resolved unambigously.

The anodes are spaced at $12.7mm$ separated by one field wire. The cathodes are $10.6mm$ copper foil strips on mylar and are glued onto a honeycomb structure. The construction of the chamber is shown in Figure 3.12. The cathodes are orientated at $\pm 34.27^{\circ}$ with respect to the anodes. This allows the coordinates in the plane of the chamber to be reconstructed without ambiguity.

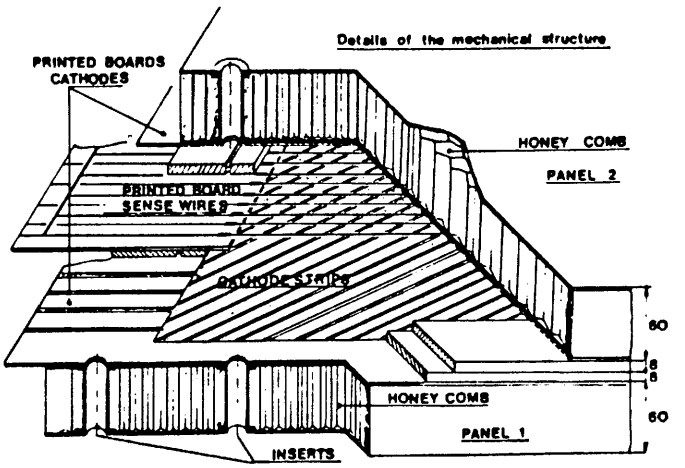

Figure 3.12: Construction of a muon chamber

3.2.7 The Forward Detector

The forward detector allows electrons to be identified in the extreme forward region $0.9969 \leq |cos\Theta| \leq 0.9986$. This is important for identifying Bhabhas and tagging electrons/ positrons to study two-photon physics.

The detector consists of drift chambers with scintillators and lead glass shower counters. It must be robust to stand large amounts of synchrotron radiation, beam gas and beam pipe interactions.

There are three groups of two drift chambers, each with eleven sense wires at 45^o and 135^o relative to the vertical operating, in a 30% isobutane 70% argon mixture. Due to the large amount of background multihit TDCs with a $4ns$ least count error are used for readout. In the first and third groups scintillators cover all of the drift chamber's active area, and in the second group there is two planes of overlapping finger scintillators. The scintillator resolves left-right ambiguities and excludes synchrotron radiation hits from track-finding.

The lead glass block shower counters consists of six vertical, six horizontal and sixteen longitudinal blocks with lengths of $3X_0$, $3X_0$ and $14X_0$. Comparing pulse heights from these three readout layers cuts can be made so that only $2-3\%$ of minimum ionising particles are mis-identified as electrons.

3.2.8 The Trigger System

CELLO can be triggered by combinations of charged and/or neutral triggers which are selected by computer control. The charged trigger information comes

from the central tracker and the neutral trigger information from the calorimeter and the forward detector's lead glass shower counters.

The Charged Particle Trigger

The charged particle trigger is a programmable hardware trackfinding processor [37] . It can make a decision in less than $1500ns$ after a bunch crossing signal, acting on information from the five CPC's and two CDC's. The decision is taken on the basis of the following requirements,

1. Curved tracks in the $R\Phi$ projection above a preselected transverse momentum ($\sim 350\frac{MeV}{c}$) are found from the anodes wires of the CPCs and CDCs, using only hit information from the CDCs.

2. Straight tracks in RZ projection are found using the CPC 90^o cathodes. To reduce the background rate due to beam-gas events these tracks must come from a limited region about the interaction point.

The fast trackfinding is done separately in 64 $R\Phi$ sectors and 37 RZ sectors, shown in Figure 3.13. The sector signals are compared with masks which correspond to the hit combinations in a sector of all allowed tracks. These masks are stored in RAMs and because of the large amount of memory available chamber inefficiencies have been taken into account so that tracks with 5/7, 6/7 or 7/7 hits in the $R\Phi$ sector and 4/5 or 5/5 hits in the RZ sector can be triggered on.

A summation logic then counts the number of masks which have been fulfilled and compares this with the preselected trigger conditions. The triggers

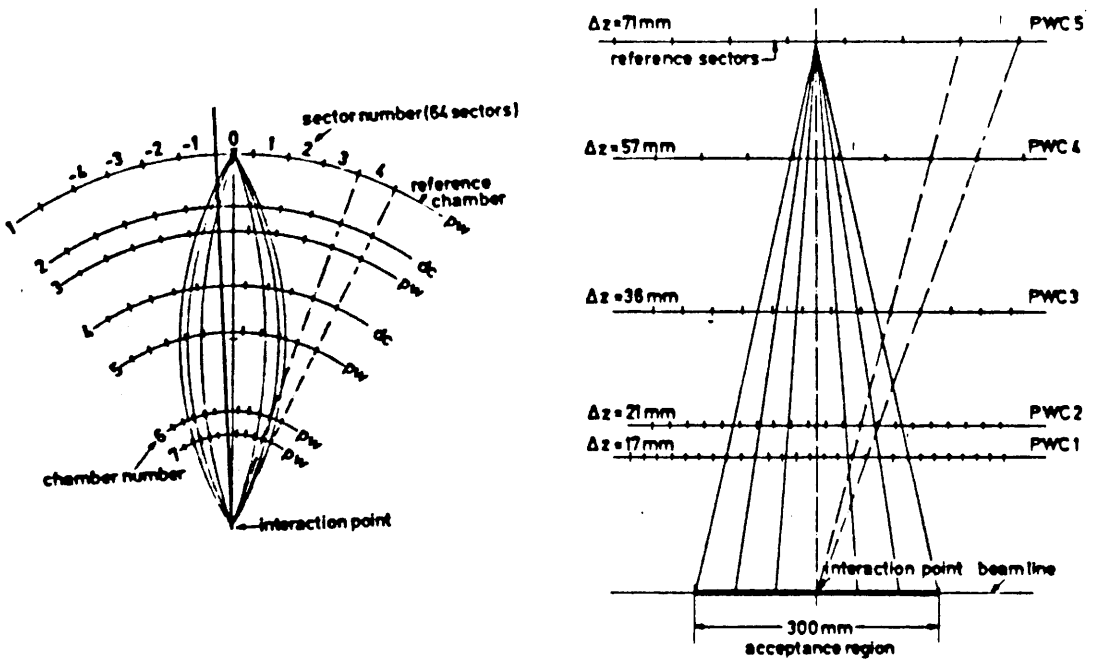

Figure 3.13: The $R\Phi$ and RZ sectors

used for this analysis were purely charged triggers since the minimum ionising muons would not be selected by neutral triggers. The trigger used in the analysis required:

- Two track candidates in $R\Phi$ with at least 5/7 hits, a minimum transverse momentum of 250 $\frac{GeV}{c}$ and an opening angle of at least 135° between the tracks. It also required at least one track in the RZ projection and a low number of hits in the BPCs and the CPC 90° cathodes.

The Neutral Triggers

The neutral triggers use information from the barrel and endcaps of the lead-liquid argon calorimeter and the forward detector's shower counters.

In the barrel the neutral trigger [38] is based on reading out the signals from each stack and forming the following energy sums:

SUMA This is formed by combining the U-channels in layers $1-5$ giving a sampling over the range $1-17X_0$.

SUMB This is formed by combining the U-channel in layer 2 with the V-channel in layer 3. This provides a sampling around the electromagnetic shower maximum, $3.5-7X_0$.

The channels are readout $1.5\mu s$ after the beam crossing so that the shower has fully developed. In addition SUMB is sampled $0.5\mu s$ after the beam crossing to provide a signal not synchronised with an event. Requiring that both SUMA and SUMB give signals reduces background from noise in the electronics and the out of time SUMB can be used to veto events from noise and cosmic rays. The final trigger decision is ready after $2.1\mu s$.

Both of the energy sums have adjustable threshold energies between 1 and 3 GeV depending on the trigger conditions. From the energy sums the following neutral triggers were defined:

- At least one module with an energy deposit of 2 GeV, from both SUMA and SUMB.
- Two modules separated by at least 45^o in the $R\Phi$ projection each having a minimum of 1.8 GeV, from SUMA only.

In the endcaps the energy sums per module are used. All signals from the semicircular strips are summed and compared with discriminator thresholds. A trigger based on a signal from any one of the modules is used in conjunction

with the charged triggers. A stand alone trigger of two and only two modules is used for Bhabha selection independent of track information.

The forward trigger uses coincidences between the scintillator and energy deposited in the lead glass shower counters.

3.2.9 Data Acquisition

The detector components are read out by a CAMAC-ROMULUS system with each detector component and the trigger having its own branch, as shown in Figure 3.14. Each of the branches can be accessed by either the online computer or by a minicomputer which monitors the data and can run simple programs to check the performance of the individual detector.

The online computer, a PDP 11/55, reads out the data from the CAMAC branches, it's large buffer averaging peak trigger rates, and produces an event record. It then passes the events to the DESY IBM computer where the events are stored on disk and transferred to tape when the disk is full. It also runs an elaborate control program which allows the whole detector to be monitored and controlled by a shift crew of two physicists. While the data is on disk it is accessed by a 370/E emulator and passed through the filter program which is discussed in chapter 4.

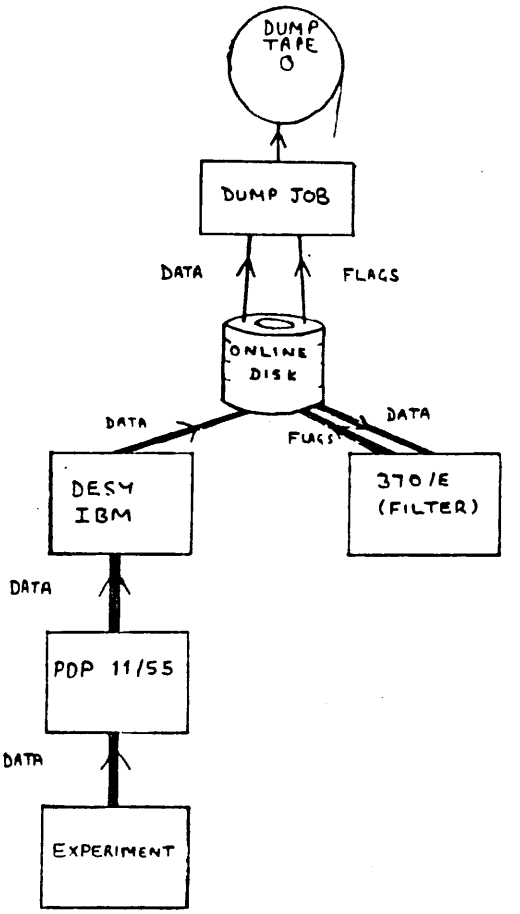

Figure 3.14: Data acquisition system

Chapter 4

Experimental Software

4.1 The Event Filter

The CELLO trigger system, described in Chapter three, is designed to trigger on physical processes of interest such as Bhabha, multihadronic and two photon events and is optimised to produce a data rate of $\leq 10Hz$ compatible with the data acquisition system. However a large fraction of these triggers will be background events such as beam-gas interactions, beam-pipe interactions and cosmic-ray events. Such events are not easily discriminated against by the triggers, which are necessarily simple to minimise the time taken to make the decision whether to reject or accept an event. Therefore, to reduce the number of background events before the final reconstruction by the program OFFRAM, described later in this Chapter, a filter program analyses the data while it is on the online disk and classifies events as good or bad according to whether it is an event of physical interest or an obvious background event. Good events are kept

and fully reconstructed and bad events are discarded. The filter program is run on a $370/E$ emulator which runs programs in the same way as an IBM 370/168 mainframe. Its use greatly lowers the computing load on the DESY IBM and the computers of the collaborating institutes but its slower speed means it cannot process all the events on the online disk before the disk is full, when the events must be transfered to tape. This is compensated for by running the filter offline on the DESY IBM to process the remaining events. Usually the emulator processes around 60% of the events depending on data rates. After processing the remaining 40% of the events, the offline filter checks that the emulator was working by reprocessing several events that were classified as bad and checks that they are again marked bad. The filter then writes all events onto DUMP tapes. The filter program is then rerun, this time discarding all the events marked bad and writing all the events marked good onto FILTER tapes. These FILTER tapes are then distibuted to the collaborating institutes to be passed through the reconstruction program. The filter program and reconstruction program OFFRAM are described below.

4.1.1 The Filter Program

The filter [40] uses information from

- The central tracker wire chamber coordinates.
- The pulse height sums of the calorimeter stacks (SUMA).
- The barrel calorimeter single channels.

Using this information the data is reconstructed in three stages, described below, each stage using more information. After each reconstruction the event is compared with acceptance criteria. If an event is accepted it is classified as a good event and is passed onto the next stage of reconstruction. If an event is rejected it is classified as bad and it is not further reconstructed. After the third and last reconstruction all good events have their triggers verified. This is done by checking that at least one trigger, compatible with the acceptance criteria used, had fired. If an event is not fully analysed due to decoding or bank errors or it being marked neither good nor bad, then it is also kept.

First pass reconstruction

The first pass reconstruction uses the proportional and drift chamber wires to calculate the Φ coordinates. Using this information an attempt is made to find tracks in the $R\Phi$ projection. Two patterns are looked for, a single track coming from the interaction point which is approximated by $r = 0$, where r is the radial distance from the interaction point in the $R\Phi$ projection, and collinear tracks

which are not forced through $r = 0$. This separation into two classes is done so that cosmic rays are found and kept.

The single track reconstruction starts by finding two point pairs (r_1, Φ_1) and (r_2, Φ_2). These are taken from a fixed set of chamber pairs and should have an angle between them of $< \frac{\pi}{8}$. A curve is generated using (r_1, Φ_1), (r_2, Φ_2) and $r = 0$ which is a good approximation to a circle. Hits are then looked for in a road around the curve and if nine hits are found then it is fitted to an exact circle through $r = 0$ and accepted as a track if the quality of the fit, measured by the χ^2, of the fit is good.

Including $r = 0$ in the fit means that events such as beam-gas, beam-pipe and cosmic ray events will not be reconstucted and subsequently rejected. However it is desirable to retain cosmic ray events for calculation of muon chamber efficiencies, geometrical alignment of the detector and for mu-pair analyses such as this one.

To retain cosmic rays a second reconstruction was made to find collinear tracks. To start two points are found in the same PC or DC but with an angle between them of greater than $\frac{\pi}{8}$. A circle is then generated using the two initial points and $r = 0$ and a road around it searched for hits in the same way as above. However in the fit $r = 0$ is not used and so cosmics will be reconstructed. However beam-gas and beam-pipe interactions do not have a simple collinear track pattern and so they will still not be reconstructed.

From the track information the quantities used as acceptance criteria are the number of reconstructed tracks N_{trk}, the absolute sum of the charges of the

tracks $\mid \Sigma q \mid$ and for two tracks or more the largest opening angle between two tracks ($\Delta\phi_0$). If a track is found using the collinear fit N_{trk} is set to two.

The liquid argon and forward shower counter energies are calculated from the A sums, defined in Chapter 3, of the liquid argon and the single channels of the forward counters, which are treated as a +Z stack and a -Z stack. Each stack is calibrated individually and the stack energies are divided into energy levels L_E given in Table 4.1.

Class	Level L_E	Energy range
junk	-1	$E_{stack} \leq -800MeV$
zero	0	$-800MeV < E_{stack} \leq 800MeV$
low	1	$800MeV < E_{stack} \leq 1500MeV$
medium	2	$1500MeV < E_{stack} \leq 2000MeV$
high	3	$2000MeV < E_{stack}$

Table 4.1: Energy level definitions

The stack direction cosines with respect to the interaction point are calculated. Using the direction cosines and the energy levels an energy spread parameter S_E is calculated,

$$S_E = max_{i,j}\Omega_{ij} \times (L_i + L_j) \tag{4.1}$$

where Ω_{ij} is the angle between any two stacks and L_i, L_j their respective energy levels. The value of Ω which maximises S_E, θ_S is also calculated and used as an acceptance criterion. The event time with respect to the bunch crossing is calculated from the in time and out of time liquid argon trigger sums:

$$t_{event} = 2\mu s \frac{atan\frac{D}{P}}{\pi} \tag{4.2}$$

where D is the out of time SUMB pulse height and P is the in time SUMB pulse height. A stack is then said to be in time if $t_{event} \leq 0.3\ \mu s$.

The quantities used as acceptance criteria are the number of stacks with a given energy level, the number of stacks in time, S_E and Θ_S.

The track and energy information is compared with a set of acceptance criteria examples of which are given below,

\$ACC 0 /	$N_{trk} \geq 4$	$\Delta(\phi_0) > \frac{2\pi}{8}$	$\mid \Sigma q \mid < N_{trk}$	
\$ACC 13 /	$N_{st,hi} < 5$	$S_E > 16$	$\theta_S < \frac{\pi}{16}$	

Table 4.2: Example of acceptance criteria

All the events which are accepted are marked good and go onto the next reconstruction the remaining are marked bad and no further processing of them is done.

Second pass reconstruction

The Z coordinates are found for each of the Φ coordinates used in the track in the $R\Phi$ projection. A clustering algorithm is used on the 30^o and 90^o cathodes of the CPCs and the Z coordinates are found from the overlaps of these clusters.

Using these coordinates, tracks in the RZ projection are looked for. Ideally these tracks could be found by considering only Z coordinates associated with Φ coordinates of the $R\Phi$ track. However this is impractical due to mirror coordinates and high multiplicity events in which there may be more than one Z coordinate associated with a Φ coordinate. So a road method similar to that

used to find the $R\Phi$ track is used to find the RZ track. The road is defined around a straight line through a Z coordinate pair. If at least four coordinates are found in the road then the points are fitted to straight line. The track with the most points and in ambiguous cases the best χ^2 is used as the RZ track.

A Z vertex is now searched for, if the vertex is found to lie outside $Z = \pm 15cm$ then all the reconstructed tracks are ignored, i.e. N_{trk} is set to zero.

The track quantities are redefined taking into account the RZ track and the event is again compared with the acceptance criteria and marked good or bad accordingly.

Third pass reconstruction

In this last stage showers in the stacks are reconstructed. Clusters are searched for in the U, V, W stack projections and are then merged in space. The energy levels are recalculated using the the total reconstructed shower energy and S_E and Θ_S are recalculated using the direction cosines of the shower. The events are compared with the acceptance criteria for the last time.

The filter program rejects 75% of the events. To check that this 75% consisted of background events Monte Carlos were used to determine the selection efficiencies for various processes of physical interest. The efficiency for multihadronic events is 98% and for Bhabhas and μ-pairs it is 99%.

4.2 Event reconstruction: OFFRAM

Events which pass the filter are processed by the main reconstruction program OFFRAM. This consists of several semi-independent programs which calculate useful physical quantities such as momentum, energy and direction cosines from the raw data collected by the various detector components. The output consists of a set of BOS banks [41] [42] produced by the subprograms described below.

4.2.1 CELPAT

The program CELPAT searches for tracks in the central tracker. The program consists of two parts: the space point reconstruction program, ANOCAT and the track finding programs, RFIPAT and RZPAT.

ANOCAT reconstructs space points in the CPCs by looking for correlations between the three coordinates: the 90° cathode strips, the 30° cathode strips and the anode wires.

RFIPAT searches for tracks in the $R\Phi$ projection using coordinate information from the CDCs and the CPCs. The $R\Phi$ projection is divided into overlapping sectors each of which is searched for a track, using only points from a single sector. This procedure imposes a momentum cut since the size of the sector will limit the curvature of the track. The program initially uses a large number of small sectors which allows high momentum tracks to be found quickly and then repeats the procedure several times, increasing the sector width each time to find low momentum tracks. The program allows the variables of the fit to

be changed to allow for different kinds of physics analysis e.g. the interaction region may or may not be included depending on whether good momentum resolution is required or a search for decay vertices is being made.

In the RZ projection RZPAT searches for straight lines that point back to the interaction region.

Finally the tracks in the $R\Phi$ and RZ projections are combined using the space points reconstructed by ANOCAT to make a complete three dimensional track.

In this reconstruction no interaction point information is used and the magnetic field is assumed to be a constant axial field of 1.32 T. The output is a bank for each track containing its momentum, charge, spatial direction, χ^2 of the track fit etc.

4.2.2 CELGEOM

This takes the tracks found by CELPAT and refits them using an accurate map of the magnetic field and including the interaction point as a point on the track. The interaction point is obtained from Bhabha events by doing a common fit to both tracks using the GLOFIT program described below. Inclusion of the interaction point as a point on the track increases the momentum resolution since the momentum resolution is inversely proportional to the square of the tracklength [43]. As in CELPAT the interaction point can be left out of the fit.

The CELGEOM fit information is put into the CELPAT track bank along with the CELPAT information.

4.2.3 GLOFIT

This takes two tracks and providing they are approximately collinear, subjects them to a common fit. The interaction point is not included and so the fit can be used to obtain vertex information. Using the two tracks in a common fit improves the momentum resolution since the tracklength is increased.

The output is another single bank containing the track information. Since in GLOFIT infomation about the acollinearity of the two tracks is lost both CELGEOM (or CELPAT) and GLOFIT information is used in this analysis.

4.2.4 LATRAK

This reconstructs electromagnetic showers in the liquid argon calorimeter from the charge deposited in the stacks to give the energy deposited, spatial direction of the shower, link information to tracks in the central tracker etc. In each of the seven layers of a stack, two dimensional clusters are searched for using correlations between the three strip orientations. The program then examines these clusters to see if any of them have a double cluster structure consistent with overlapping showers.

Charged tracks are then extrapolated into the calorimeter and a set of clusters are searched for which can be linked together to form a three dimensional shower associated with the track. A fit is then made using the centres of gravity of the clusters used in the shower and the entry point of the track to the calorimeter to find the shower axis.

The remaining clusters are searched for possible showers. The shower axis is found using a fit in the same way as above but using the interaction point instead of the track entry point.

4.2.5 MUCH

The program MUCH [44] reconstructs hits in the muon chambers and associates these to tracks reconstructed in the central tracker. The output gives information on the reconstructed hits and the quality of the association with tracks in the central tracker.

Hits are reconstructed either using all three coordinates, from the two sets of cathode strips and the anode wires or using any combination of two of these coordinates. There are two sources of error on each reconstructed point: the error due to the width of the cathodes strips and the spacing of the anode wires, and the uncertainty of the position of the muon chambers in the CELLO coordinate system. The error matrix associated with the reconstucted point is then:

$$\begin{pmatrix} \sigma_x & 0 \\ 0 & \sigma_y \end{pmatrix} \tag{4.3}$$

where σ_x and σ_y are errors defined in the muon chamber frame x,y (see Figure 4.1).

The tracks in the central tracker are extrapolated up to the muon chambers taking into account the effect of the magnetic field on the particles trajectory and the loss of momentum as it passes through the calorimeter and the hadron filter. This is achieved by extrapolating in steps, revaluating the particle's tra-

jectory and momentum after each step. The result is a point, P (see Figure 4.1) where the extrapolated track intersects the chamber, and an error matrix associated with P. The error matrix takes into account: the uncertainties in the track information from the central tracker and the effect of multiple scattering as the particles are tracked through the calorimeter and the hadron filter. Therefore P lies at the origin of a coordinate frame u,v; defined such that the error matrix is diagonal i.e.

$$\begin{pmatrix} \sigma_{ue} & 0 \\ 0 & \sigma_{ve} \end{pmatrix} \tag{4.4}$$

The chamber coordinates frame x,y and the frame associated with the extrapolated point; u,v are not, in general, the same and so the two error matrices cannot be combined. However the errors σ_x and σ_y are approximately equal and so the error matrix is approximately circular. Therefore the error matrix of the reconstructed point can be rotated into the u,v frame without introducing any off-diagonal terms into the error matrix. The errors on the reconstructed point are now σ_{ur} and σ_{vr} defined by:

$$\sigma_{ur} = \sqrt{\sigma_x^2 cos^2\alpha + \sigma_y^2 sin^2\alpha} \tag{4.5}$$

$$\sigma_{vr} = \sqrt{\sigma_x^2 sin^2\alpha + \sigma_y^2 cos^2\alpha} \tag{4.6}$$

where α is the angle of rotation between the two coordinate frames as shown in Figure 4.1.

The two sets of errors can now be combined in quadrature to give the final

errors σ_u and σ_v:

$$\begin{pmatrix} \sigma_u & 0 \\ 0 & \sigma_v \end{pmatrix} = \begin{pmatrix} \sigma_{ue}^2 + \sigma_{ur}^2 & 0 \\ 0 & \sigma_{ve}^2 + \sigma_{vr}^2 \end{pmatrix} \tag{4.7}$$

The reconstructed point is defined in the u,v frame as R(U,V) as shown in Figure 4.1, and the quality of association can now be defined as:

$$Q = \sqrt{\left(\frac{U}{\sigma_u}\right)^2 + \left(\frac{V}{\sigma_v}\right)^2} \tag{4.8}$$

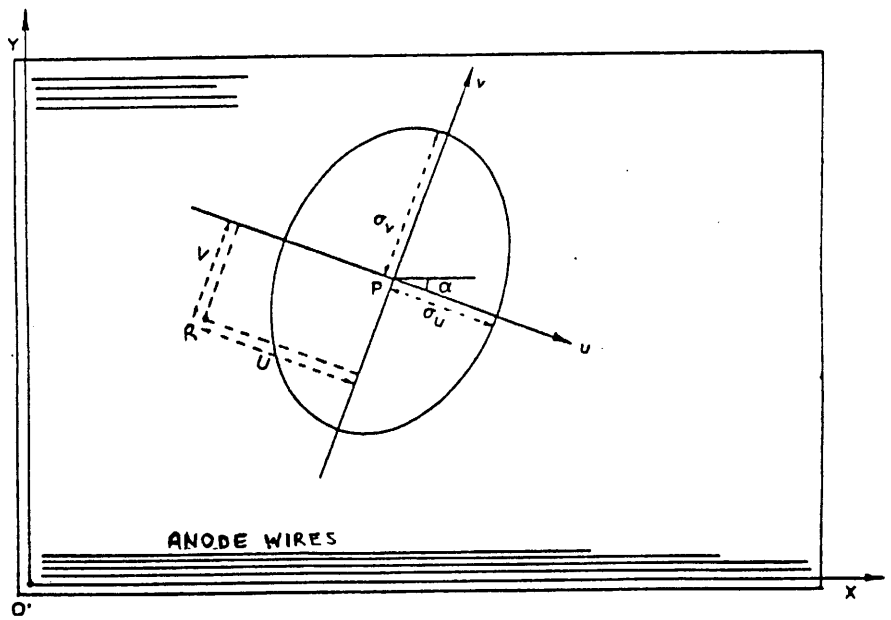

Figure 4.1: The frame of the extrapolated track in the muon chambers

The large amount of material between the interaction point and muon chambers, particularly the calorimeter material and the hadron filter, means that low momentum muons are less likely to reach the muon chambers than high momentum muons. To evaluate this muons with different momenta were generated using Monte Carlo and tracked through the material taking into account the

energy loss [44]. From this, the probability of a muon reaching the muon chambers as a function of inverse momentum was found and is plotted in Figure 4.2. A momentum cut of 3 $\frac{GeV}{c}$ ensures that a muon reaches the muon chambers.

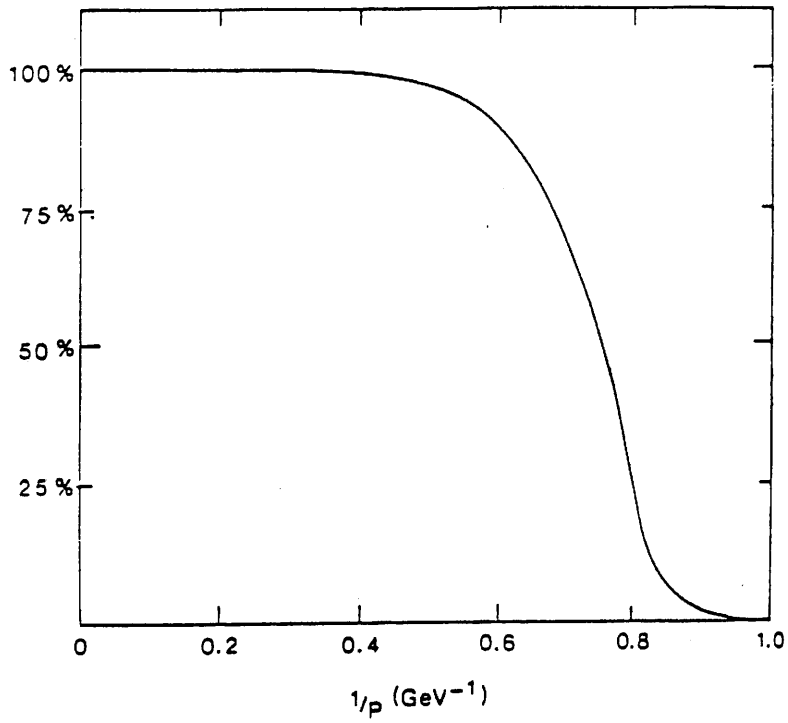

Figure 4.2: Probability of a muon reaching the muon chambers as a function of inverse momentum

The output from OFFRAM is written onto DSTs (Data Summary Tapes), to reduce the number of these tapes to a manageable level the tapes are passed through the DST SELECT filter [45] . It applies very loose cuts on the total energy, momentum and total number of tracks of an event; accepting all physics processes of interest but rejecting beam-gas and beam-pipe interaction events. It also suppresses events selected by the random trigger: this selects events at random which are not selected by other triggers for studying e.g. background, and the number of Bhabha events selected by the forward trigger. The output is written onto DST SELECT tapes. For this experiment this reduced the 806 DST tapes to 371 DST SELECT tapes.

4.3 Detector simulation

To compare experimental measurements with theoretical predictions the influence of the detector due to limited geometrical acceptance and the efficiencies of the various detector components, must be studied and their effect removed from the measurement. Often this can be done using an independent process e.g. the determination of the muon chamber efficiencies using cosmic ray events, but this is not always possible and so a detailed detector simulation is required.

The detector simulation consists of two parts: PTRAK followed by CELLINT. PTRAK takes the four vectors from the physics Monte Carlo e.g. LUND for multihadronic events or BKJ [24] for $e^+e^- \rightarrow \mu^+\mu^-(\gamma)$, and tracks them through the detector simulating the interactions of electrons and photons with the detector material: the beampipe, coil calorimeter and the hadron filter,

using the EGS program [46] and simulating the passage of hadrons and muons through the calorimeter hadron filter using the HETC program [47]. CELLINT then takes the particle's track information and energy deposits, and using measured detector constants such as: central tracker chamber efficiencies and calorimeter calibration constants, builds a raw data record which has the same format as that of a real event. The raw data can then be reconstructed using OFFRAM in the same way as real data.

Chapter 5

Muon selection

5.1 Introduction

An $e^+e^- \rightarrow \mu^+\mu^-$ event in the CELLO detector has a distinctive signature: two back to back straight tracks coming from the interaction region in the central tracker, little or no energy deposited in the calorimeter as muons are minimum ionising particles, and hits in the muon chambers which can be associated with the tracks using the procedure described in Chapter 4. An example of such an event is shown in Figure 5.1: Figure 5.1a shows the $R\Phi$ projection and Figure 5.1b shows the RZ projection.

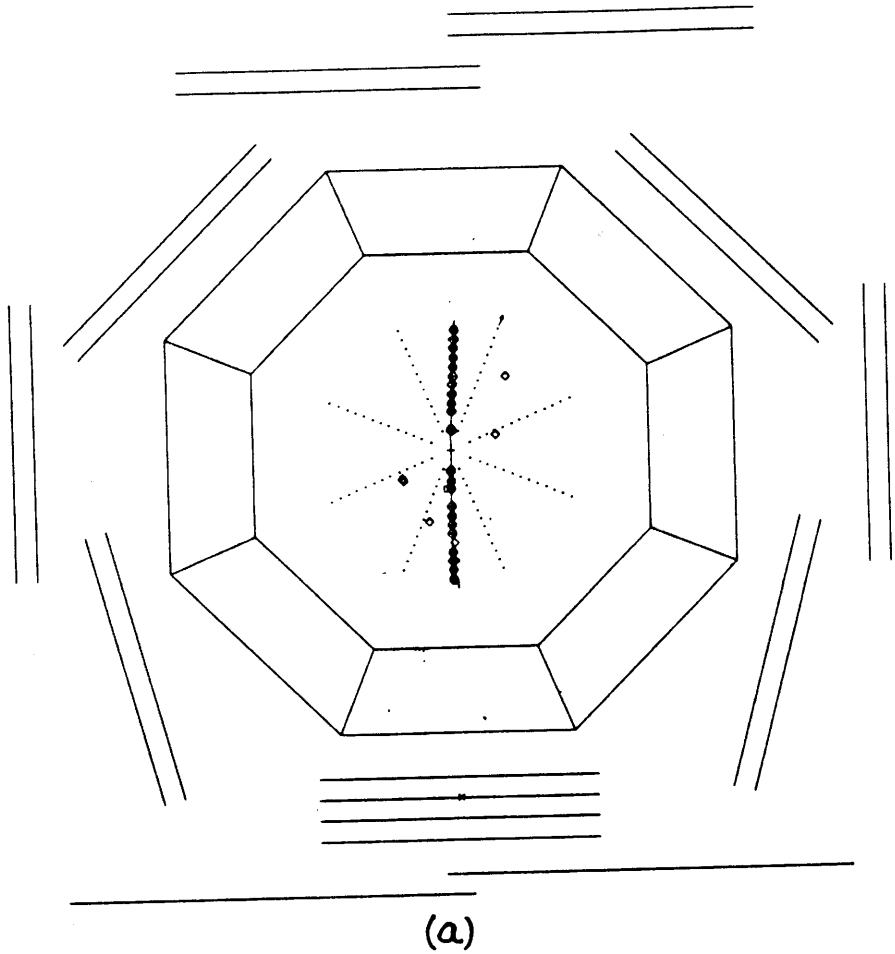

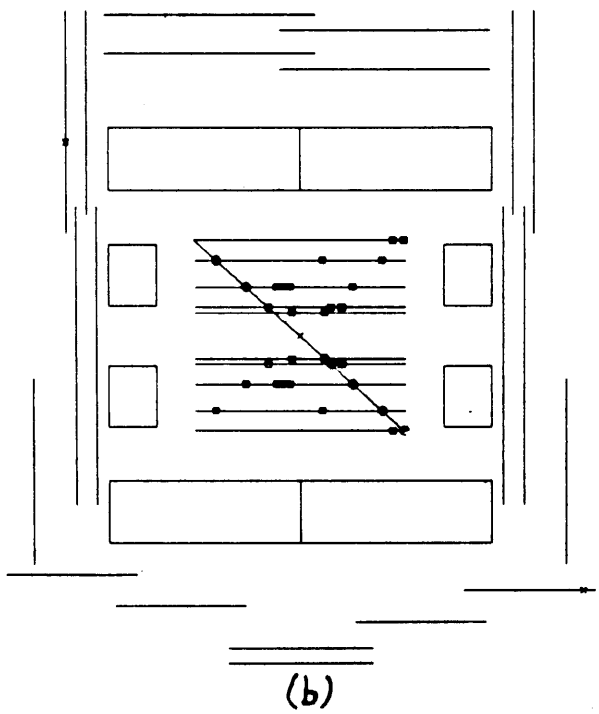

Figure 5.1: A typical μ-pair event

Unfortunately other processes lead to events with, to a greater or lesser degree, a similar signature to the $e^+e^- \rightarrow \mu^+\mu^-$ signature. Such processes are cosmic ray events, Bhabha events, $e^+e^- \rightarrow \tau^+\tau^-$ and $e^+e^- \rightarrow e^+e^-\mu^+\mu^-$ events. These events must be eliminated from the data sample and so we discuss these processes further.

cosmic ray events

Primary cosmic rays impinging on the upper atmosphere consist of protons (87%), α-particles (12%) and heavier nuclei. The subsequent nucleon-nuclei interactions produce large numbers of pions and kaons. The pions and kaons either decay or undergo further interaction with nuclei before decaying, however their short lifetime means that most of them decay in the atmosphere. The charged pions and kaons decay mainly into muon channels. These muons do not interact in the atmosphere and are stable resulting in a large muon flux at sea level.

Both the differential and integral intensity of cosmic ray muons have been measured as a function of momentum at sea level for directions close to the vertical in the range $0.1 \rightarrow 10^3 \ \frac{GeV}{c}$ using magnetic spectrometers. This is shown in Figure 5.2 taken from [48]. The intensity peaks at low momenta $\sim 1 \ \frac{GeV}{c}$ and falls rapidly with increasing momentum.

The intensity has also been measured as a function of zenith angle, θ, the angle between the incoming track and the vertical. The intensity falls with increasing zenith angle according to $I(\theta) = I(\theta = 0)cos^n\theta$ where $n \simeq 2$ for the

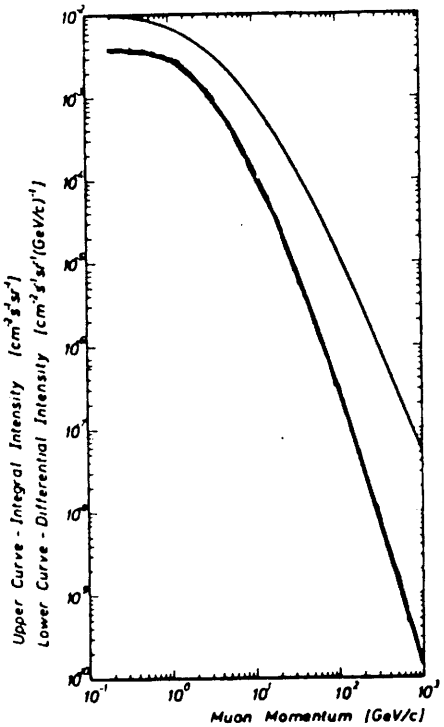

Figure 5.2: The vertical differential and integral cosmic ray muon momentum measured at sea level

range $0^o \rightarrow 75^o$.

Thus a large flux of muons falls on the detector. If a cosmic ray muon should pass through the detector while the beam crossing gate is open then it will trigger the detector which will record an event such as the one shown in Figure 5.3 below.

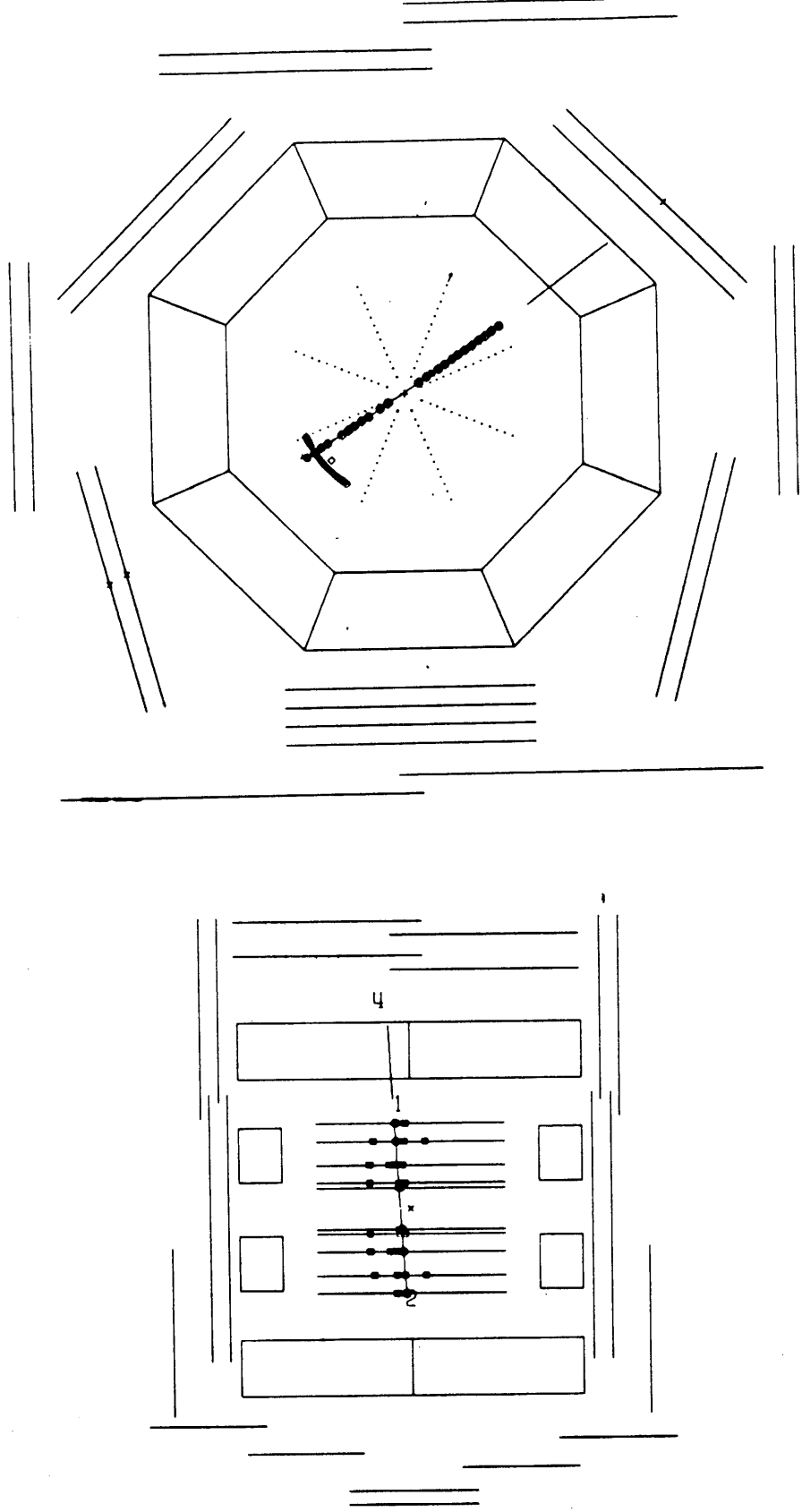

Figure 5.3: A cosmic ray event

Comparing this event with the $e^+e^- \rightarrow \mu^+\mu^-$ event candidate we see that such events are indistinguishable, only the fact the track does not pass through the interaction region reveals its true nature. In fact we can not say that the event shown in Figure 5.1 is definitely a $e^+e^- \rightarrow \mu^+\mu^-$ event. This contamination can be reduced by imposing cuts on the the $\delta R\Phi$ and δRZ distances, cuts on the momentum which will drastically reduce the cosmic ray flux falling on the detector, as shown by the momentum spectrum in Figure 5.2 and a timing cut to ensure the event is synchronised with the beam crossing. However despite these cuts a number of cosmic ray events will mimic the $e^+e^- \rightarrow \mu^+\mu^-$ events perfectly and so these must be subtracted using the background subtraction procedure described below.

Although such events are a bad backgound they can be used to provide a sample of pure muons to determine, for example, the muon chamber efficiencies.

Bhabha events

Bhabha events, like $e^+e^- \rightarrow \mu^+\mu^-$ events, have two back to back straight tracks in the central tracker but unlike muons, electrons deposit most or all of their energy in the calorimeter in the form of electromagnetic showers and so they either do not penetrate the hadron filter to make hits in the muon chambers or the hits cannot be well associated with the tracks in the central tracker. However there are cracks in the calorimeter e.g. between the modules through which an electron can pass without depositing any of it's energy. They can then pass through the hadron filter to make hits in the muon chambers which can

be well associated with tracks in the central tracker. Two methods were used to estimate this and are described later.

This background must be well understood as Bhabhas have an angular distribution which is strongly forward peaked. Thus even a small background would increase the muon asymmetry although not significantly affecting the total cross-section.

Bhabha events come from the interaction region and will have a similar momentum spectrum to $e^+e^- \rightarrow \mu^+\mu^-$ events. Being very numerous Bhabhas thus can be used to define the interaction region and the momentum cut. They can also be used to determine the charged trigger efficiency.

$e^+e^- \rightarrow \tau^+\tau^-$ $e^+e^- \rightarrow e^+e^-\mu^+\mu^-$

A small fraction of $e^+e^- \rightarrow \tau^+\tau^-$ events (3.1%) will decay into a $\mu^+\mu^-$ pair, neutrinos and antineutrinos. These events can be rejected with high efficiency by cuts in the acollinarity of the μ-pair and muon momentum since the undetected particles result in missing momentum. $e^+e^- \rightarrow \tau^+\tau^-$ events will not affect the measurement of the asymmetry since such events have the same angular distribution as $e^+e^- \rightarrow \mu^+\mu^-$ events. However such a contamination would affect the measurement of the total cross-section.

The two-photon process $e^+e^- \rightarrow ee\mu\mu$ has a total cross-section comparable with that of $e^+e^- \rightarrow \mu^+\mu^-$, however such events have missing momentum associated with the undetected electron and positron. Thus a momentum cut strongly suppresses this background.

5.2 Preselection

This sample was made from DST SELECT tapes using the following cuts,

- There must be exactly two charged tracks
- Both tracks must have momentum greater than 2.5 $\frac{GeV}{c}$
- Both tracks must have $\mid cos\theta \mid \leq 0.95$

The requirement of exactly two charged tracks with minimum momentum rejects multihadronic events, beam-gas and beam-pipe interaction events while accepting: $e^+e^- \rightarrow \mu^+\mu^-$, cosmic-ray and Bhabha events. The $\mid cos\theta \mid$ cut is applied since this analysis uses the barrel calorimeter which covers the region $\mid cos\theta \mid \leq 0.85$ as shown in Figure 3.3. The Bhabha and cosmic-ray events are kept for evaluating efficiencies and studying the cuts.

Figure 5.4 shows the energy deposited by a track in the calorimeter for events from the preselection sample. The low energy peak is due to muons which are minimum ionising and the high energy peak is due to the electrons which deposit most or all of their energy as electromagnetic showers in the calorimeter. Thus a cut on the energy deposited in the calorimeter associated with a track can be used to select Bhabha events.

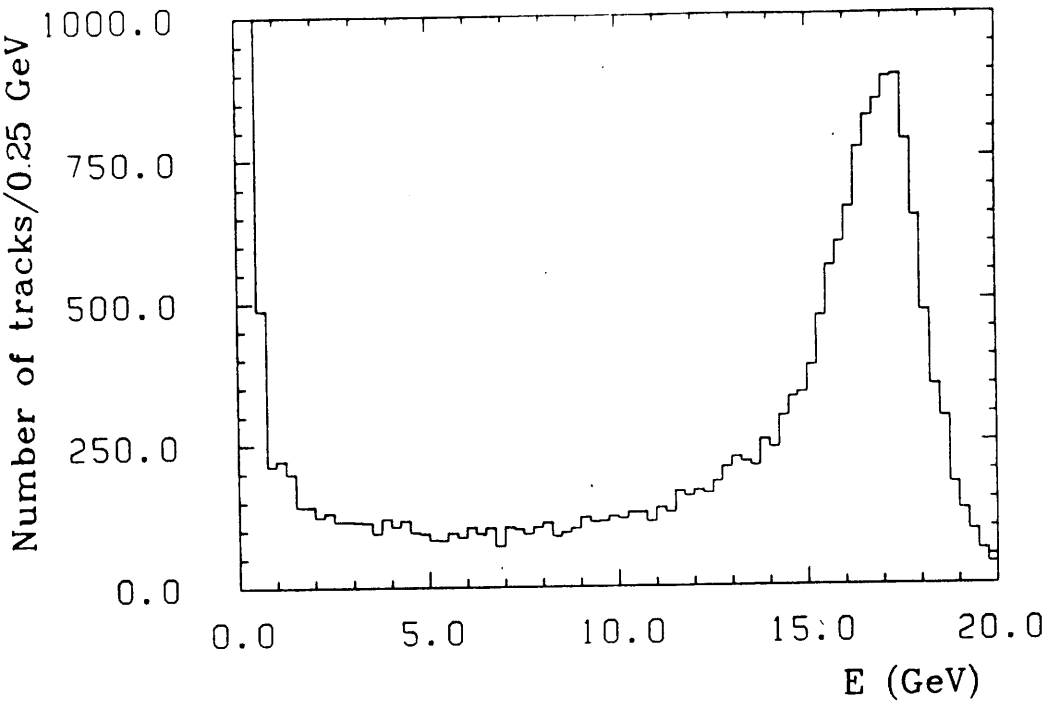

Figure 5.4: Energy deposition in the barrel calorimeter

5.2.1 Bhabha selection

For an event to be classified as a Bhabha it had to satisfy:

- Both tracks must have momentum greater than 3.0 $\frac{GeV}{c}$ and must lie within $\mid cos\theta \mid \leq 0.85$.
- Showers associated with the tracks must deposit $\geq 0.3 * E_{beam}$ in the calorimeter
- The acollinearity of the two tracks must be $\leq 25^{o}$

The distributions of the distance to the beam spot in the RZ plane, δRZ and in the $R\Phi$ plane $\delta R\Phi$ for Bhabha events ,as selected above, are shown in Figures 5.5 and 5.6 respectively.

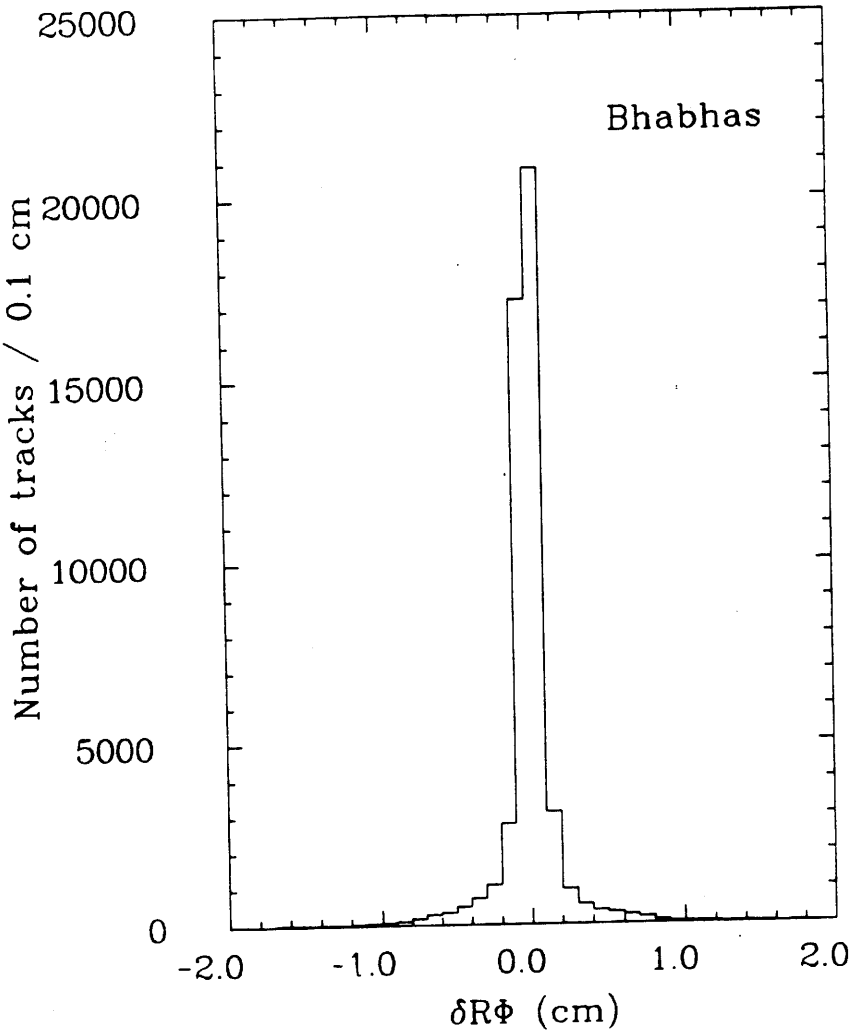

Figure 5.5: Distibutions in $\delta R\Phi$ Bhabha events

From Figures 5.5 and 5.6 we can define the interaction region as a cylinder in space defined by $\mid \delta R\Phi \mid \leq 0.5$ and $\mid \delta RZ \mid \leq 2.5$. This definition rejects 8% of the Bhabha events and so 8% of $e^+e^- \rightarrow \mu^+\mu^-$ events. Having defined the interaction region we can select cosmic ray events by looking for events with $\delta R\Phi$ and δRZ lying outside the interaction region.

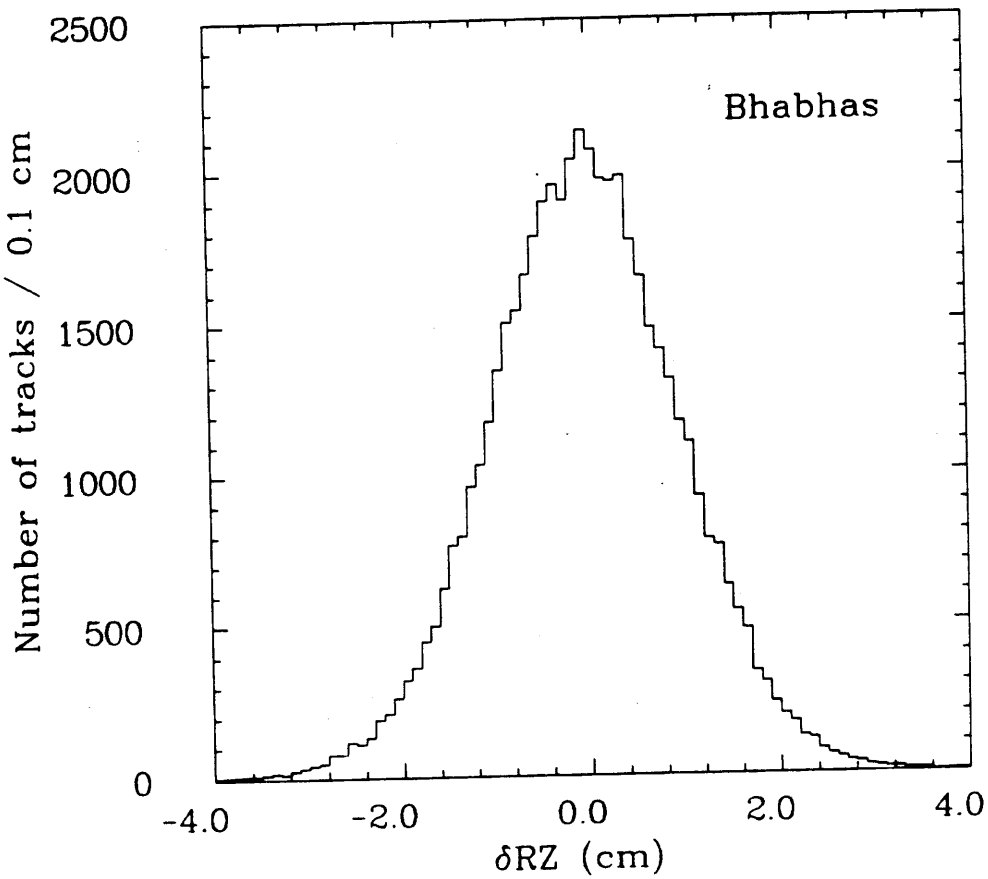

Figure 5.6: Distibutions in δRZ Bhabha events

5.2.2 cosmic ray selection

A sample of cosmic-ray events was found using the following cuts:

- Both tracks must have momentum $\geq 3.0\ \frac{GeV}{c}$ and lie within $\mid cos\theta \mid \leq 0.85$
- The showers associated with tracks should deposit a maximum of 1.3 GeV in the calorimeter
- $\mid \delta R\Phi \mid \geq 0.5$ cm and $\mid \delta RZ \mid \geq 2.5$ cm

These vertex cuts accept $\leq 1\%$ of Bhabhas.

5.3 Muon selection

An event was classified as a muon candidate (arising from an $e^+e^- \rightarrow \mu^+\mu^-$ event or a cosmic ray event) if it satisfied:

- The event should have been selected by the charged trigger.
- Both tracks should have momentum greater than 3 $\frac{GeV}{c}$ and lie within $\mid cos\theta \mid \leq 0.85$
- The associated showers should deposit a maximum of 3 GeV

The charged trigger is required so that the final mu-pair sample can be corrected for trigger inefficiencies when calculating the total cross-section and the angular distribution. The momentum cut ensures that the muons have ~100% probability of penetrating the calorimeter and the hadron filter, to reach the

muon chambers (see Figure 4.2). The energy cut reduces the number of Bhabha events and the $|\ cos\theta\ |$ cut is required to ensure the tracks are within the barrel calorimeter acceptance.

The data reduction for the above selections is shown in Table 5.1 below.

Selection	Number of events
DST SELECT	$\sim 4 \times 10^6$
Preselection	437771
Muon selection	44151

Table 5.1: Data reduction

The muon selection was passed through the GLOFIT program described in Chapter 4. Events which were successfully reconstructed by GLOFIT contained $e^+e^- \rightarrow \mu^+\mu^-$ events, cosmic ray events and a small contamination of Bhabhas. The improvment in the momentum and the $R\Phi$ vertex resolution are shown for Bhabha events in Figures 5.7 and 5.8, this allows tighter cuts to be imposed thus rejecting more cosmic ray events. The events not reconstructed by GLOFIT (NGLOFIT) are acollinear events in which the two tracks cannot be linked together. The events are mainly $e^+e^- \rightarrow \mu^+\mu^-$ and a small contamination of Bhabhas. There is a much smaller background of cosmic ray events in the NGLOFIT sample than in the GLOFIT sample because GLOFIT finds most cosmic ray events easy to reconstruct since they are in fact single tracks. The cuts on this sample are not as tight as on the GLOFIT sample but the smaller cosmic ray background means this is not important.

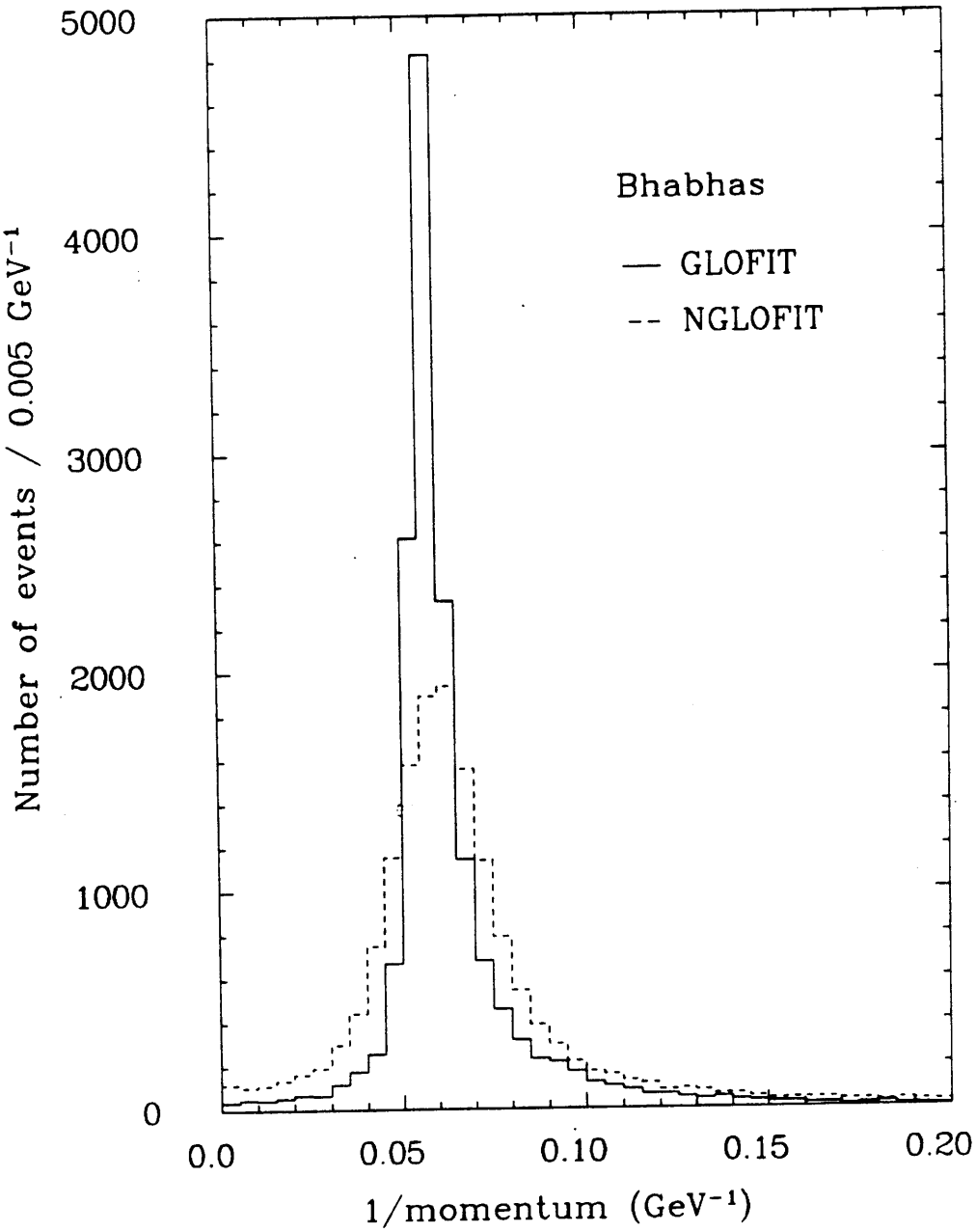

Figure 5.7: Momentum distribution for Bhabhas before and after GLOFIT

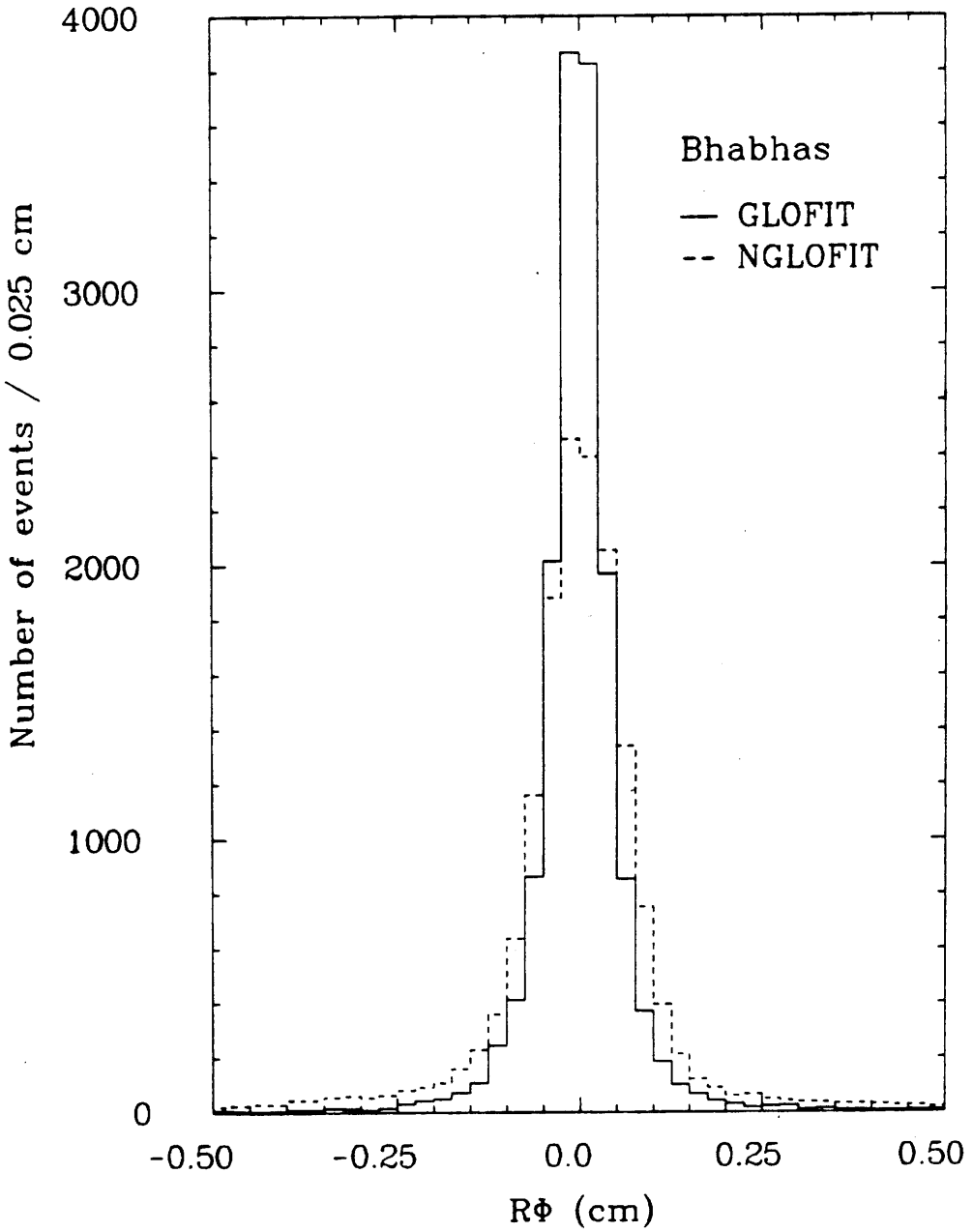

Figure 5.8: $\delta R\Phi$ distribution for Bhabhas before and after GLOFIT

5.4 Mu-pair selection

The cuts applied were

- $\mid P \mid_{cel} \geq \frac{\sqrt{s}}{4.0} \frac{GeV}{c^2}$; $\mid P \mid_{glo} \geq \frac{\sqrt{s}}{3.8} \frac{GeV}{c}$
- Energy associated with a track, deposited in the barrel calorimeter $\leq 1.3\ GeV$
- Muon chamber quality Q ≤ 5 for at least one track
- Acollinearity $\leq 25^o$
- Interaction region cut; $\mid \delta R\Phi \mid_{cel} \leq 0.4\ cm$, $\mid \delta R\Phi \mid_{glo} \leq 0.3\ cm$ and $\mid \delta RZ \mid \leq 2.5\ cm$
- Drift-time cut

where $\mid P \mid_{cel}$ and $\mid \delta R\Phi \mid_{cel}$ ($\mid P \mid_{glo}$ and $\mid \delta R\Phi \mid_{glo}$) are the momentum and $\delta R\Phi$ distance of a NGLOFIT (GLOFIT) event. The acollinearity is defined as:

$$Acollinearity = \pi - cos^{-1}\left(\frac{\mathbf{P}_1 \cdot \mathbf{P}_2}{\mid \mathbf{P} \mid_1 \mid \mathbf{P} \mid_2}\right) \tag{5.1}$$

where $\mathbf{P}_1$ and $\mathbf{P}_2$ are the momentum vectors of the first and second track respectively.

Acollinearity

The charged trigger selects tracks with a minimum opening angle, imposing an acollinearity cut. An acollinearity cut is therefore made in the analysis to ensure that the trigger efficiency is a maximum and constant.

Muon chamber quality cut

The muon chamber quality factor distributions for Bhabha events and cosmic ray events are shown in Figures 5.10and 5.9 respectively. Clearly the cut rejects many Bhabhas but retains most muons. The selection efficiency of this cut is discussed later.

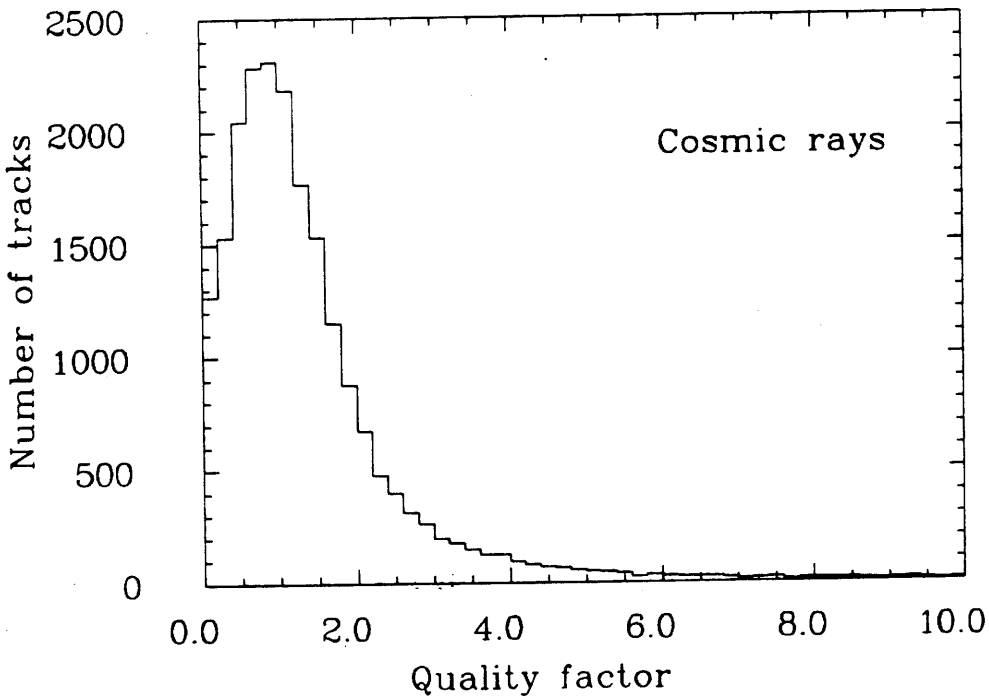

Figure 5.9: Muon chamber quality factor for cosmic ray events

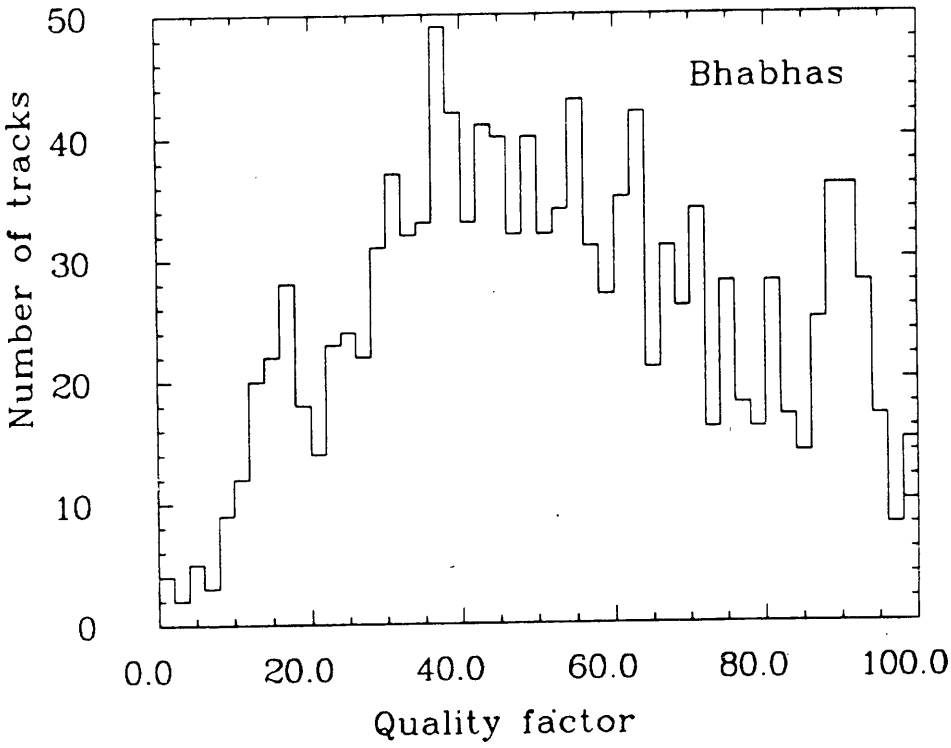

Figure 5.10: Muon chamber quality factor for Bhabha events

Energy cut

A selection of Bhabha events was made using, instead of the energy deposited in the calorimeter, the muon chamber quality factor. The energy deposition for cosmic ray events is shown in Figure 5.11 and for Bhabha events, defined as events in which both tracks have $Q \geq 30$, in Figure 5.12.

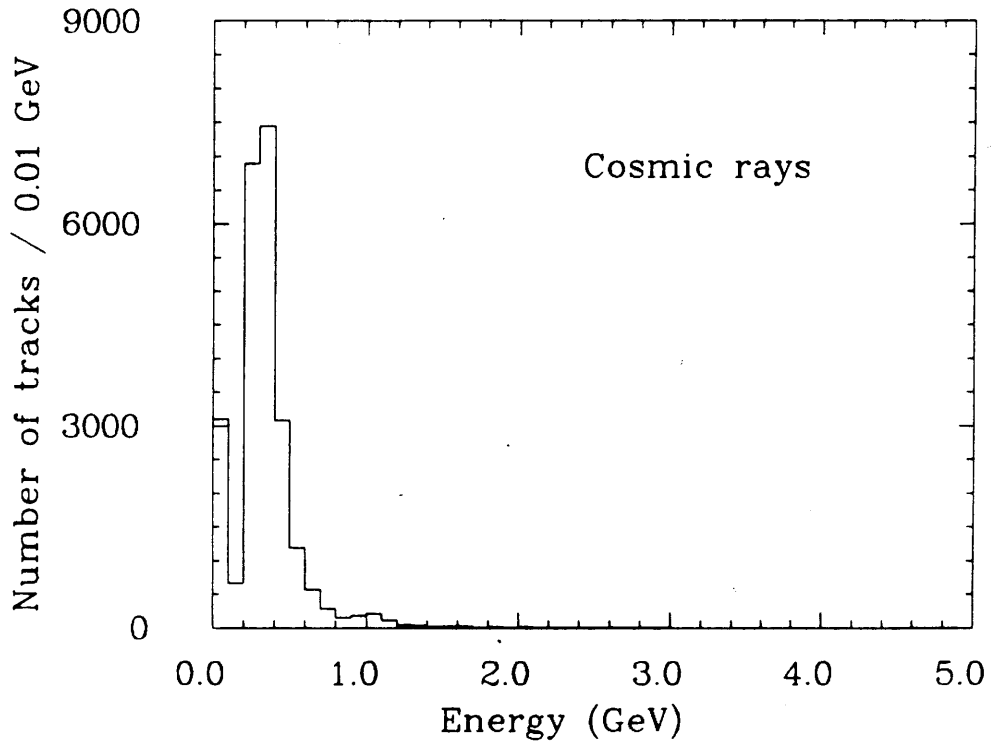

Figure 5.11: Energy deposited in the calorimeter by cosmic ray tracks

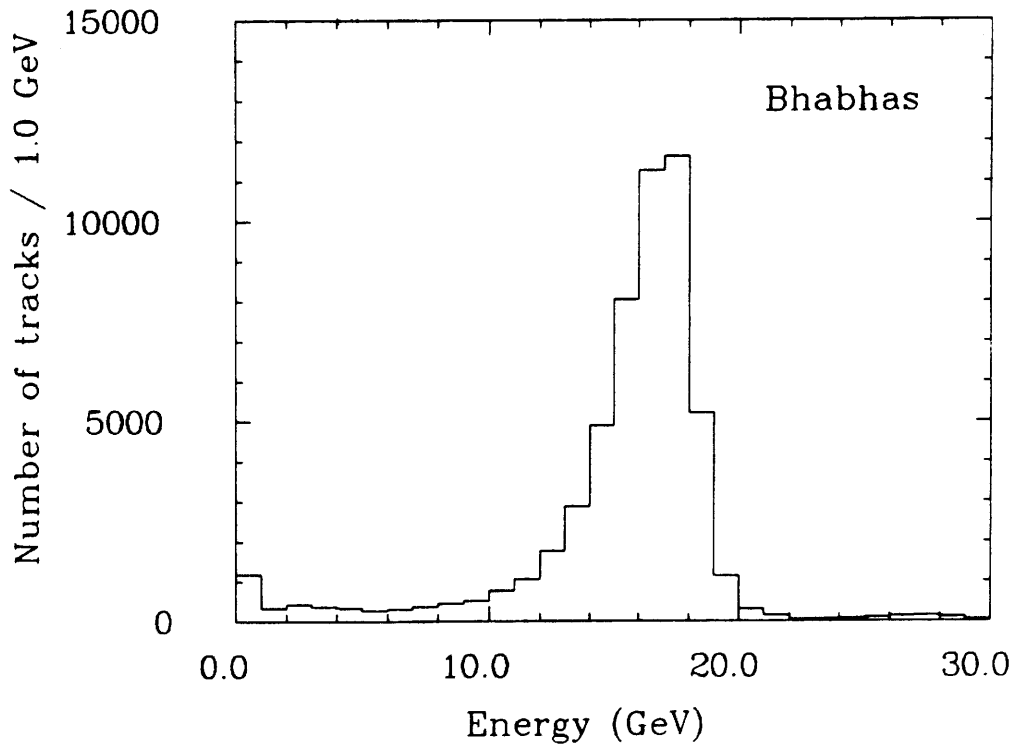

Figure 5.12: Energy deposited in calorimeter by Bhabha tracks

Momentum cut

The muon track momentum is shown for the GLOFIT events, in Figure 5.13 and the NGLOFIT events, in Figure 5.14. In both cases an $e^+e^- \rightarrow \mu^+\mu^-$ signal can be seen on a falling background of mainly cosmic ray events but also $e^+e^- \rightarrow \tau^+\tau^-$ and $e^+e^- \rightarrow e^+e^-\mu^+\mu^-$ events. The momentum cut rejects most of the $e^+e^- \rightarrow \tau^+\tau^-$ and $e^+e^- \rightarrow e^+e^-\mu^+\mu^-$ events eliminating the background due to these events. The cut also rejects a large number of cosmic ray events but a sizeable background remains. The value of the cut was found using Bhabha events.

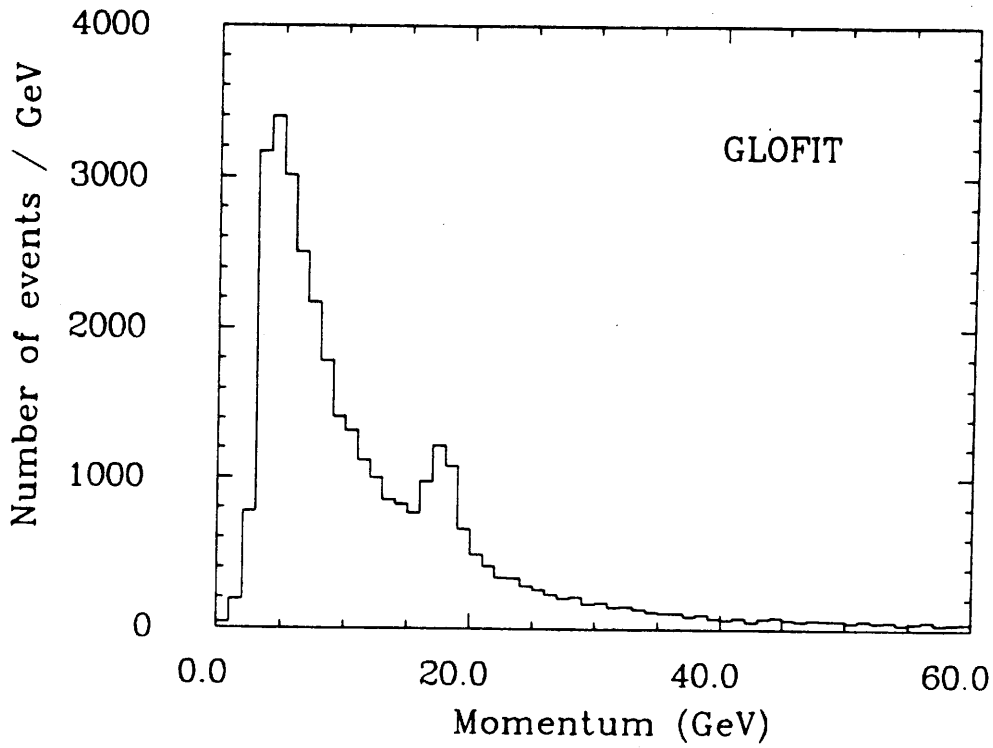

Figure 5.13: Momentum distribution of the GLOFIT sample

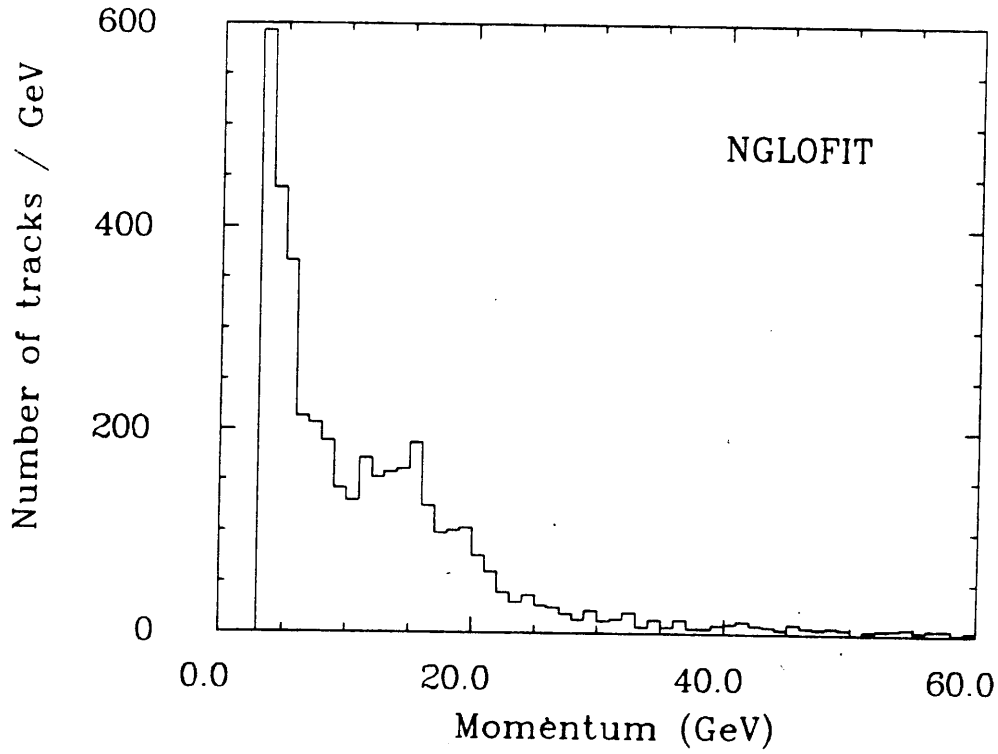

Figure 5.14: Momentum distribution of the NGLOFIT sample

Interaction region cut

Using Bhabha events the δRZ cut and $\delta R\Phi$ cuts were found (see Figures 5.6, 5.5 and 5.8). The $\delta R\Phi$ distributions for GLOFIT μ-pair events and cosmic ray background are shown in Figure 5.19. The $\delta R\Phi$ distribution for the NGLOFIT μ-pair events is shown in Figure 5.20.

Drift-time cut

The standard method of rejecting cosmics is to use time-of-flight counters to determine if the event can be associated with beam-crossing, e.g. in JADE scintillators with photomultiplier readout surround the central jet chamber. CELLO has no time of flight counters but the drift-time information from the BPCs and the outer CDCs can be used to provide crude time of flight informa-

tion to approximately determine whether an event is in time with beam-crossing or not.

Using the drift time from a single chamber will not strongly differentiate between tracks in time with the beam crossing and tracks out of time since the drift time depends strongly on the path of the track i.e. does the track pass close to an anode wire or not. However the geometry of the BPCs is such that adding the two drift times together gives a function which is approximately independent of the path, as shown in Figures 5.15a and b.

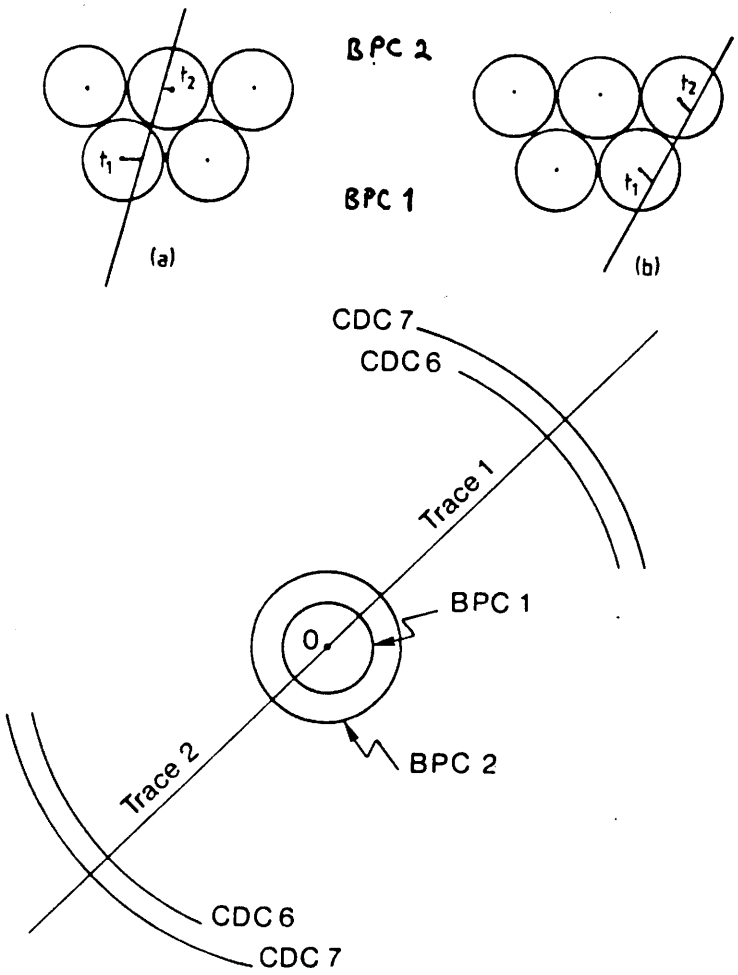

C)

Figure 5.15: Geometry of the BPCs.

This function strongly differentiates between events in time with the beam crossing and events out of time. To study this the distributions of $T_B = t_1 + t_2$ for Bhabhas and cosmic ray events were compared, see Figures 5.16 and 5.17.

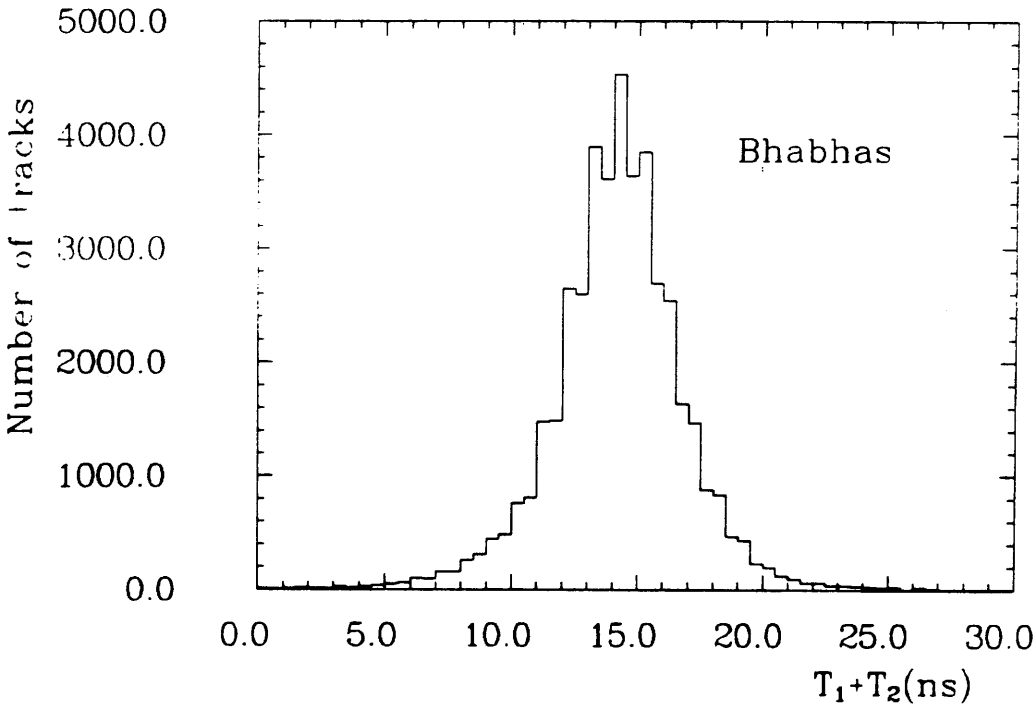

Figure 5.16: T_B distribution for Bhabha events

A similar procedure can be carried out for CDC6 and CDC7 (see Chapter 3). However the geometry of the CDCs is not as simple as that of the BPCs and so the function of the drift times used is

$$T_C = (t_6 + 10) \cdot (t_7 + 10) \tag{5.2}$$

Comparing Bhabhas and cosmic ray events we can define the following cuts:

- $7 \leq T_B \leq 21ns$
- $650 \leq T_C \leq 2200ns$

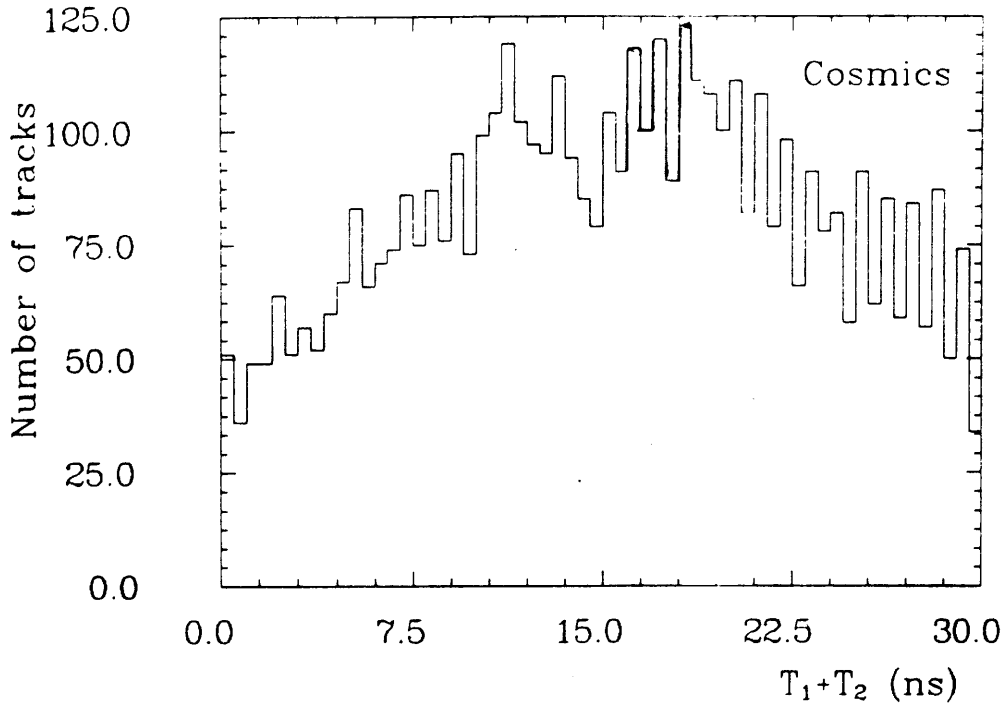

Figure 5.17: T_B distribution for cosmic ray events

Therefore cosmic ray events could be rejected by demanding that the particle tracks satisfy the following conditions (see Figure 5.15c):

- $(Trk1)_B AND (Trk1)_C$
- $(Trk2)_B AND (Trk2)_C$

where $Trk1$, $Trk2$ denote the two tracks and B (C) means that the track satisfies the BPC (CDC) timing cut.

If the above cuts were applied then a large fraction of the cosmic background would be rejected but a large number of $e^+e^- \rightarrow \mu^+\mu^-$ events would also be rejected because of chamber inefficiencies. Instead we can reverse the logic and use a similar procedure to decide if an event is a cosmic ray event or not.

A track is defined to be a cosmic ray event and rejected only if it satisfies all of the following conditions:

- $(Trk1)_{BB} AND (Trk1)_{CC}$
- $(Trk1)_{BB} AND (Trk2)_{BB}$
- $(Trk1)_{BB} AND (Trk2)_{CC}$
- $(Trk1)_{CC} AND (Trk2)_{BB}$
- $(Trk1)_{CC} AND (Trk2)_{CC}$
- $(Trk2)_{BB} AND (Trk2)_{CC}$

where BB (CC) denotes that the track does not satify the BPC (CDC) timing cut.

This procedure rejects 0.3% of Bhabha events and 28% of cosmic rays.

5.4.1 Additional cuts for the angular distribution

To obtain the angular distribution for determining the charge asymmetry the following additional cuts were imposed.

- Acollinearity $\leq 10^o$
- $\Sigma\ Q = 0$

The acollinearity cut reduces the number of $\mu\mu\gamma$ events which introduce a positive charge asymmetry as was discussed in Section 2.3. The ΣQ cut is required so that the μ^- can be identified and assigned to correct $cos\theta$ bin.

5.5 Cosmic ray background subtraction

Despite these efforts to reduce the cosmic ray background a number of these events remain in the $e^+e^- \rightarrow \mu^+\mu^-$ sample. Therefore this background must be statistically subtracted from the data to obtain the final $e^+e^- \rightarrow \mu^+\mu^-$ sample. The method uses the δRZ and the drift time cut to split the data into a pure cosmic ray sample and a $e^+e^- \rightarrow \mu^+\mu^-$ sample with cosmic ray background. The $\delta R\Phi$ distributions of the two samples are compared and the cosmic ray $\delta R\Phi$ distribution normalised to the μ-pair sample so that an estimate of the background in the μ-pair sample can be made.

The cosmic ray events used for this procedure were selected using the following cuts:

- Each track must have a momentum $\geq$ 3.0 $\frac{GeV}{c}$
- Each track must have $\mid \delta RZ \mid \geq 2.5\ cm$ or the event should be classified as a cosmic by the drift time cuts described above
- All other cuts must be the same as for the selection of the data sample except the $\delta R\Phi$ cut which is not made

The lower momentum cut retains more comic ray events which improves the statistical precision of the background subtraction. The lower cut can be made since this does not affect the normalisation. The other cuts are kept so that the sample of cosmic rays are selected under the same conditions as the data.

The $\delta R\Phi$ distributions are split into two parts:

- Events which satisfy the $\delta R\Phi$ cuts defined above (X_c events for the data and Y_c events for cosmic rays).

- Events which lie outside the interaction region satisfying: $\mid \delta R\Phi \mid_{cel} \geq$ 0.5 cm and $\mid \delta R\Phi \mid_{glo} \geq$ 0.4 cm (X_a events for the data and Y_a events for the cosmic rays)

These regions are shown in Figure 5.18.

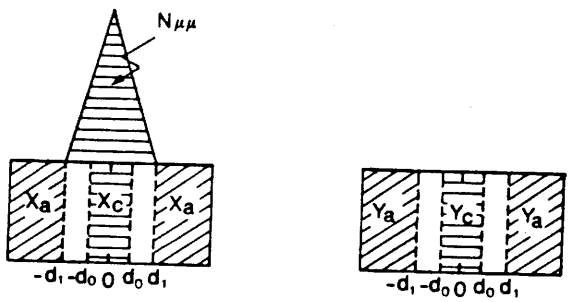

Figure 5.18: The regions used in the background subtraction

The small gap between the regions is to avoid the tail of the $e^+e^- \rightarrow \mu^+\mu^-$ signal being included in region X_a since this would affect the normalisation.

The number of cosmic rays in the data sample is

$$N_{cosm} = X_c = \frac{X_a}{Y_a} Y_c \tag{5.3}$$

where these numbers relate to the number of events in the distributions in the regions defined above. The number of $e^+e^- \rightarrow \mu^+\mu^-$ candidates in the selected sample N_{tot} is:

$$N_{\mu\mu} = N_{tot} - N_{cosm} \tag{5.4}$$

The statistical error on the number of $e^+e^- \rightarrow \mu^+\mu^-$ candidates is therefore not Gaussian. From (5.4) above the error on $N_{\mu\mu}$, $\delta N_{\mu\mu}$, is now given by:

$$\delta N_{\mu\mu} = (\delta N_{tot}^2 + \delta N_{cosm}^2)^{\frac{1}{2}} \tag{5.5}$$

assuming that N_{tot} is Gaussian distributed then $\delta N_{tot} = \sqrt{N_{tot}}$. δN_{cosm} is, from (5.3), given by:

$$\delta N_{cosm} = \left(\frac{\delta X_a}{X_a} + \frac{\delta Y_a}{Y_a} + \frac{\delta Y_c}{Y_c} \right)^{\frac{1}{2}} \tag{5.6}$$

assuming Gaussian errors for δX_a, δY_a and δY_c this becomes

$$\delta N_{cosm} = \left(\frac{1}{X_a} + \frac{1}{Y_a} + \frac{1}{Y_c} \right)^{\frac{1}{2}} \tag{5.7}$$

The $\delta R\Phi$ distribution for the GLOFIT μ-pair data and the normalised cosmic ray distribution is shown in Figure 5.19 and for the NGLOFIT data in Figure 5.20. The other results are summarised in Table 5.2 below:

	GLOFIT sample	NGLOFIT sample
Signal	2922 ± 61	533 ± 23
Background	604 ± 16	3 ± 1
$\frac{Signal}{Background}$	4.3 ± 0.2	178 ± 60

Table 5.2: Summary of background results

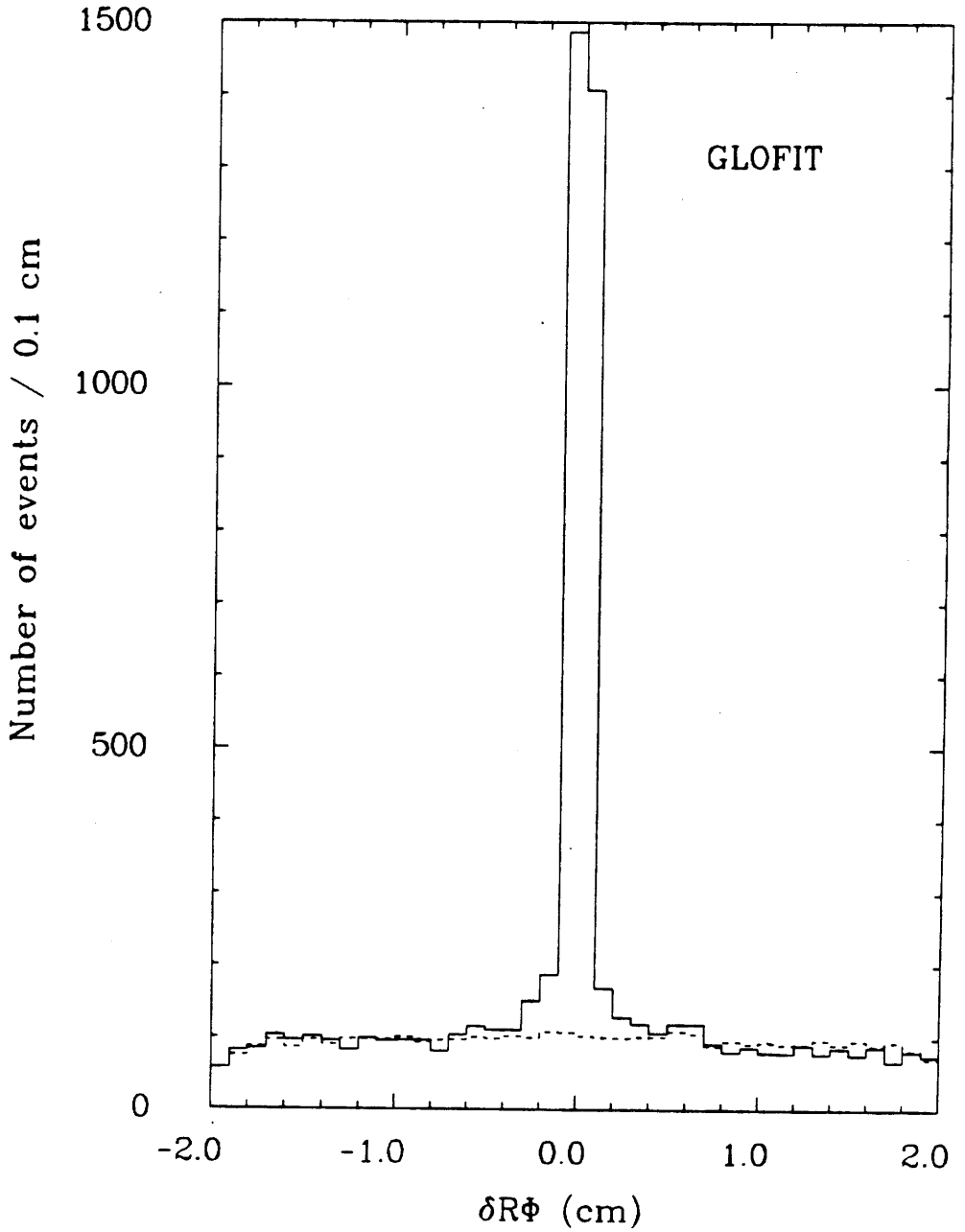

Figure 5.19: $\delta R\Phi$ distribution for the GLOFIT μ-pair data (full line) and for the normalised cosmic background (dashed line)

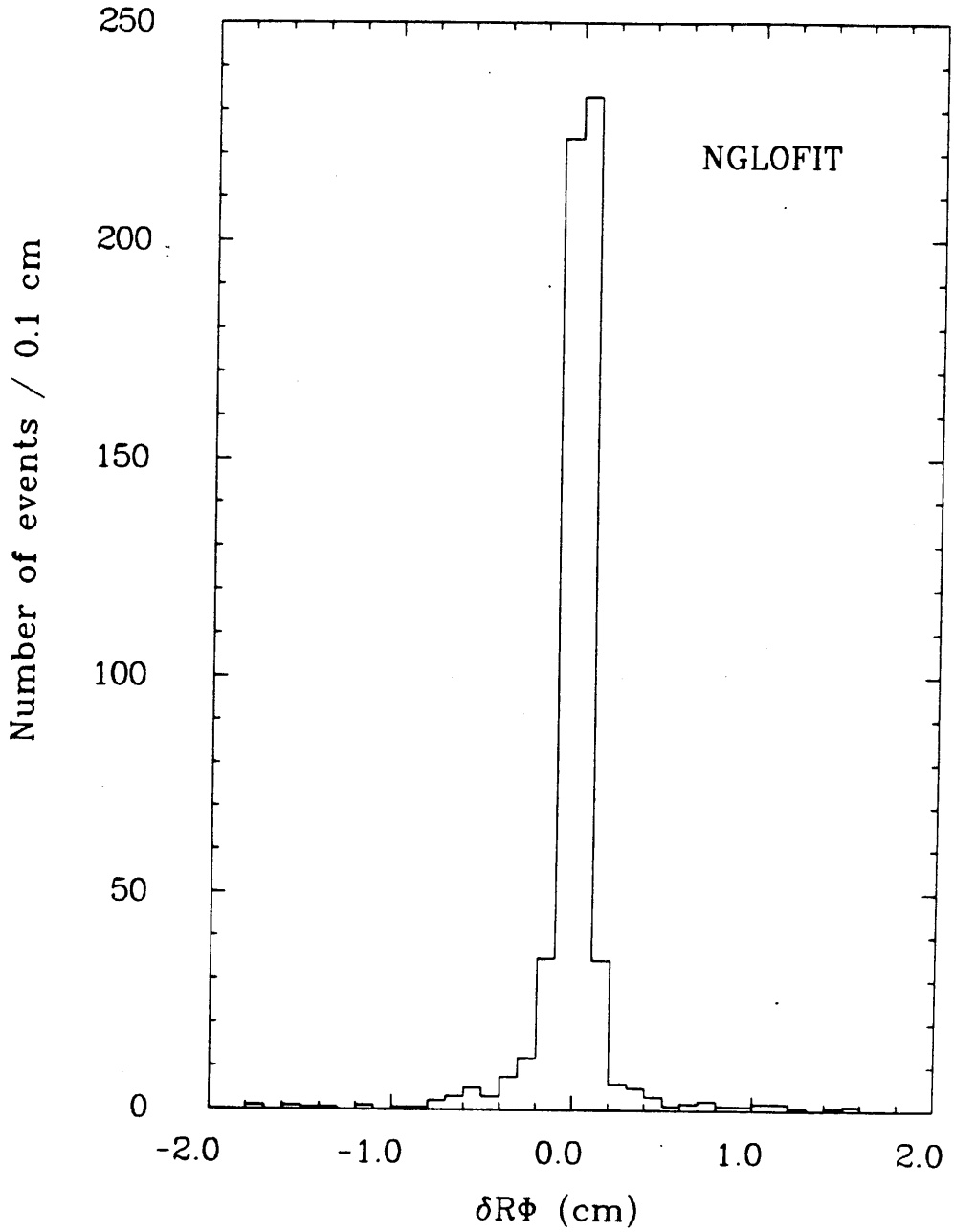

Figure 5.20: $\delta R\Phi$ distribution for the NGLOFIT μ-pair data

For the angular distribution the background must be subtracted from each $cos\theta$ bin. Therefore the cosmic ray sample selected using all the cuts applied to the data except the $\delta R\Phi$ and δRZ cuts and then split into the same $cos\theta$ bins as the μ-pair sample. A smaller momentum cut cannot be used in this case because the angular distribution depends on the momentum cut, as shown in Figure 5.21.

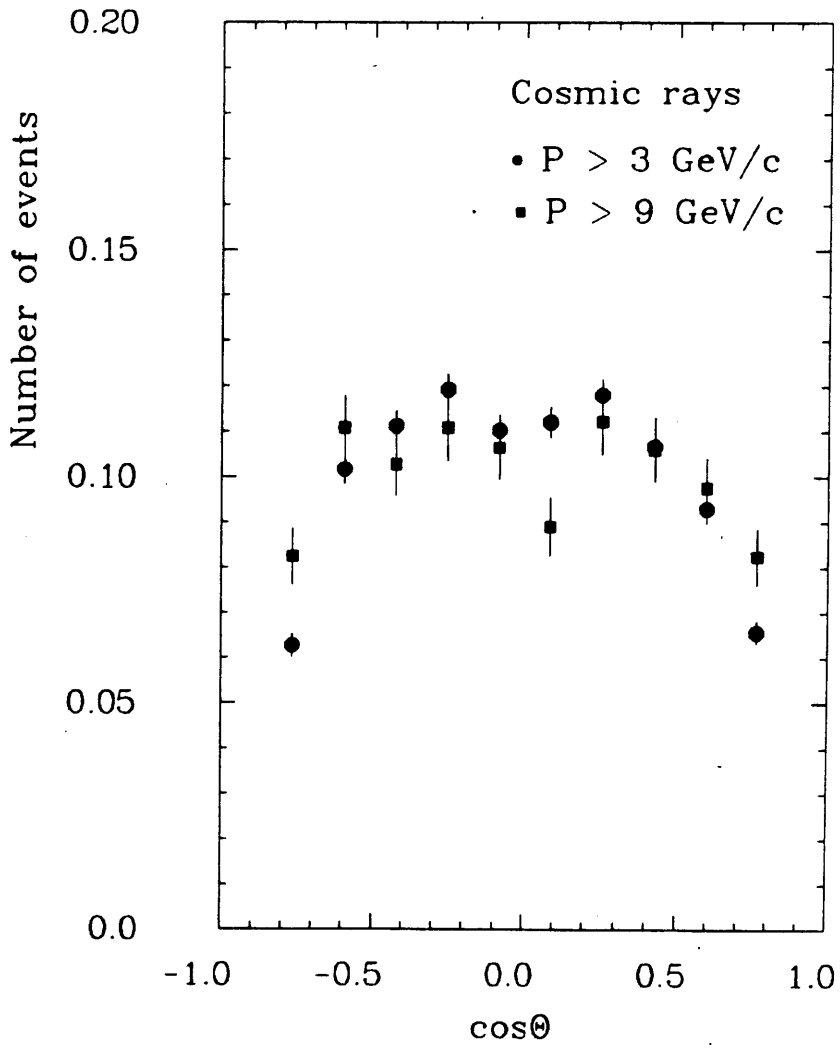

Figure 5.21: Angular distribution of cosmic ray events for different momentum cuts, normalised to one

The background in each bin N^i_{cosm}, can then be estimated from

$$N^i_{cosm} = \frac{Y_c}{X_a} Y_c \frac{n^i_{cosm}}{\Sigma n^i_{cosm}} \tag{5.8}$$

where n^i_{cosm} is the number of cosmic rays in the i^{th} $cos\theta$ bin and Σn^i_{cosm} is the total number of cosmic ray events. The number of $e^+e^- \rightarrow \mu^+\mu^-$ candidates, $N^i_{\mu\mu}$, in a given $cos\theta$ bin of N^i_{tot} events is then

$$N^i_{\mu\mu} = N^i_{tot} - N^i_{cosm} \tag{5.9}$$

As for $N_{\mu\mu}$ above the errors on $N^i_{\mu\mu}$, $\delta N^i_{\mu\mu}$, is given by

$$\delta N^i_{\mu\mu} = (N^i_{tot} + \delta N^{i\ 2}_{cosm})^{\frac{1}{2}} \tag{5.10}$$

assuming that N_{tot} has Gaussian errors and δN^i_{cosm} given by

$$\delta N^i_{cosm} = \left(\frac{\delta X_a}{X_a} + \frac{\delta Y_a}{Y_a} + \frac{\delta Y_c}{Y_c} + \frac{1}{N^i_{cosm}} + \frac{1}{\Sigma N^i_{cosm}} \right)^{\frac{1}{2}} \tag{5.11}$$

5.6 Estimation of the other backgrounds

Bhabha contamination

The contamination of these events in the final $e^+e^- \rightarrow \mu^+\mu^-$ sample can be estimated using the muon chamber quality distributions for Bhabha events and the μ-pair sample. The number of events in the μ-pair sample with both tracks having a quality factor $Q > 30$ is

$$n = n_b + n_c \tag{5.12}$$

where n_b is the number of Bhabhas and n_c is the number of cosmic rays and $e^+e^- \rightarrow \mu^+\mu^-$ events which have bad quality factors due to muon chamber

inefficiencies. From a study of cosmic ray events we know that the number of cosmic ray events in this region is $< 1\%$ and therefore negligible. We then look at Bhabha events to determine the number of events where both tracks have $Q > 30$, B_h and the number of events which satisfy the cut applied to the data, of at least one track having $Q \leq 5$, B_l.

The estimated number of Bhabhas,N_b, in the $e^+e^- \rightarrow \mu^+\mu^-$ sample, $N_{\mu\mu}$, is then

$$N_b = \frac{B_l}{B_h} n \times \frac{100}{N_{\mu\mu}}(\%) \tag{5.13}$$

The contamination was estimated to be $\leq$ 0.02% of the final $e^+e^- \rightarrow \mu^+\mu^-$ sample which is negligible.

$e^+e^- \rightarrow \tau^+\tau^-$

This contamination was estimated to be $\leq 0.2\%$ [49] using Monte Carlo generated events which had been passed through the detector simulation.

$e^+e^- \rightarrow ee\mu\mu$

The cross-section for events with the electron and positron undetected was found to be 0.08 pb for events within the momentum and $cos\theta$ acceptance cut. The contamination was then estimated to be $\leq 0.2\%$ [49].

Chapter 6

Efficiencies and corrections

There are two types of correction that must be applied to the data: corrections for the inefficiencies of the detector and the selection procedure, and radiative corrections discussed in section 2.2.2.

6.1 Efficiencies

The theoretical calculations of the angular cross-section and the total cross-section when combined with the the luminosity give the number of events $N(cos\theta)$ and N_{tot} respectively, that are predicted by the theory according to

$$N(cos\theta) = L\frac{d\sigma}{d\Omega}N_{tot} = L\sigma \tag{6.1}$$

However we only detect a fraction of these events because the detector and the software used in reconstructing the events are not perfect. Therefore to compare the data with the theory we must correct the data for such inefficiencies.

6.1.1 Charged trigger efficiency

Inefficiencies in the charged trigger are due to: dead areas in the central tracker, the track not being recognised by the pattern recognition of the trigger and the trigger conditions which are set to optimise the number of events but also keep the trigger rate at a value acceptable to the data aquisition system.

The charged trigger efficiency is determined by selecting a sample of Bhabha events using the neutral trigger and the other cuts applied to the data except the muon chamber quality factor cut, the drift time cut and the charged trigger requirement and then determining the number of events selected by the charged trigger from this sample. The global efficiency ϵ_{ch} and the efficiency of the i^{th} $cos\theta$ bin ϵ^{i}_{ch} can then be defined by

$$\epsilon^{(i)}_{ch} = \frac{n^{(i)}_b}{N^{(i)}_b} \tag{6.2}$$

where $n^{(i)}_b$ is the number of Bhabhas selected by the charged trigger (in the i^{th} $cos\theta$ bin) from $N^{(i)}_b$ the number selected by the neutral trigger in the i^{th} $cos\theta$ bin.

The global efficiency is given table 6.1 and the efficiencies for the angular distribution are shown in figure 6.1.

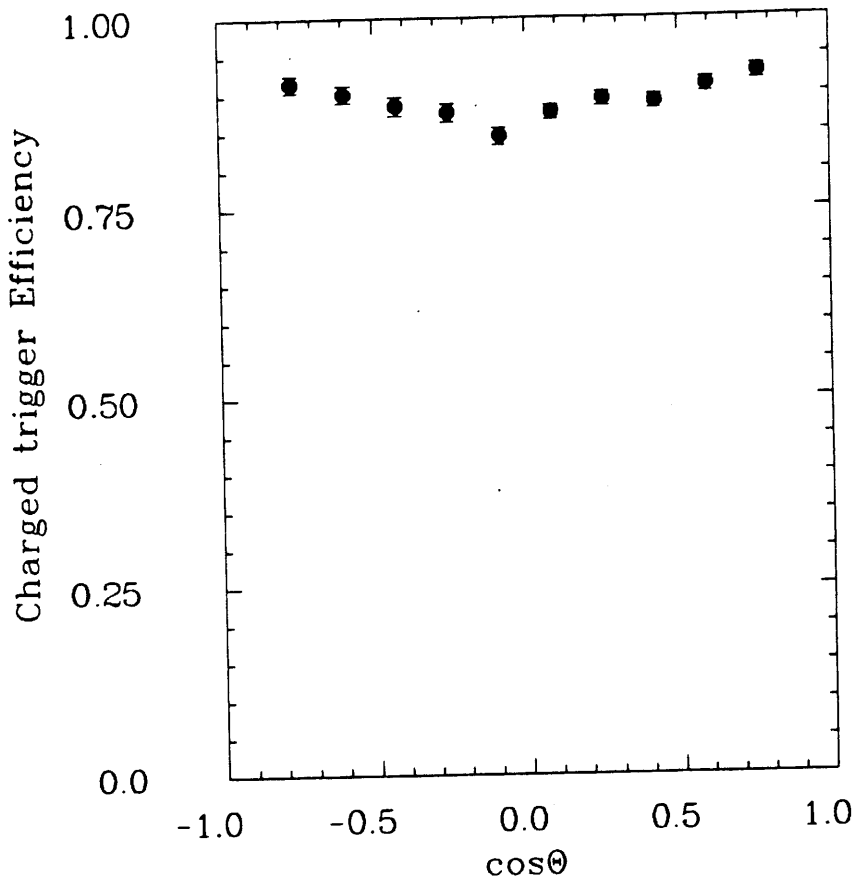

Figure 6.1: Charged trigger efficiency for each $cos\theta$ bin

6.1.2 Muon chamber efficiencies

The muon chamber efficiency is a combination of the charged particle detection efficiency of the muon chambers and the selection efficiency of the muon chamber quality factor cut. The muon chamber detection efficiency will be limited by dead areas. Inefficiencies in the muon selection can arise when a particle is not correctly tracked through the calorimeter and the hadron filter so that an incorrect quality factor is assigned to it.

The cosmic-ray selection was used to determine the global muon chamber efficiency, ϵ_μ and the the efficiency of the i^{th} $cos\theta$ bin, ϵ_μ^i from:

$$\epsilon_\mu^{(i)} = \frac{n_c^{(i)}}{N_c^{(i)}} \tag{6.3}$$

where $n_c^{(i)}$ is the number of cosmics-ray events (in the i^{th} bin) with Q_1 or $Q_2 \leq$ 5.0 and $N_c^{(i)}$ is the total number of cosmic-ray events (in the i^{th} bin).

The global efficiency is given in table 6.1 and the efficiencies for each $cos\theta$ bin are shown in figure 6.2.

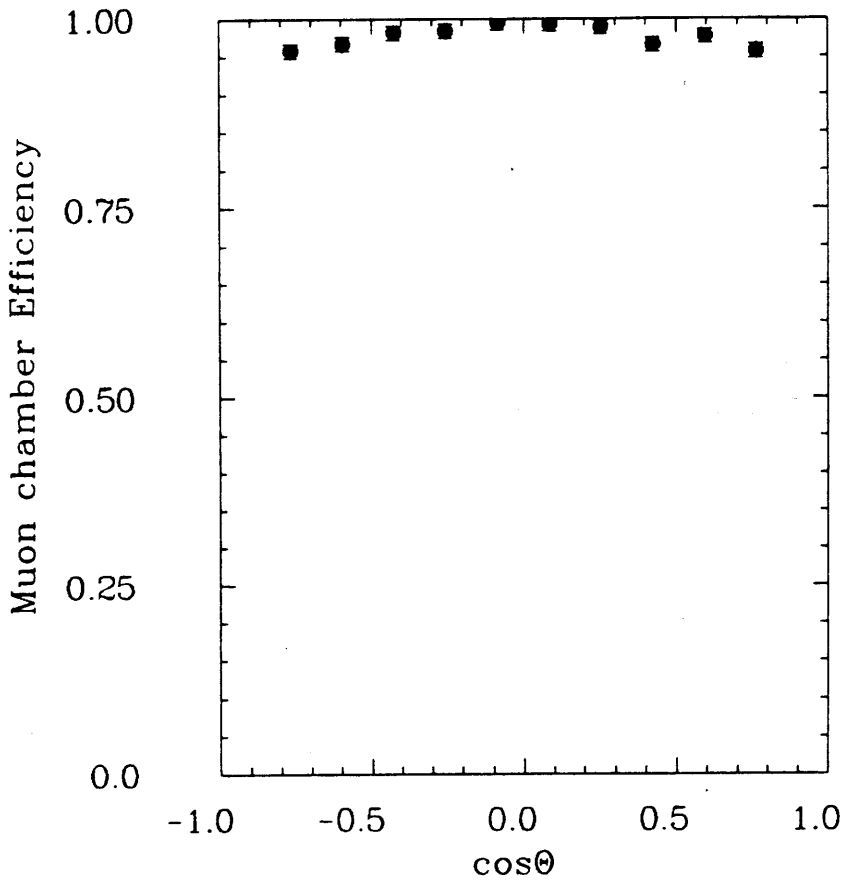

Figure 6.2: Muon chamber efficiency for each $cos\theta$ bin

6.2 Monte Carlo efficiencies

The BKJ Monte Carlo is used to generate a large number of $\mu\mu$ and $\mu\mu\gamma$ events. The generated four-vectors are then passed through the detector simulation to produce a complete event record. These events are then passed through the GLOFIT reconstruction program and the selection program. The global Monte

Carlo efficiency ϵ_{mc} and the $\cos\theta$ bin efficiency ϵ^i_{mc} can then be defined

$$\epsilon^{(i)}_{mc} = \frac{N^{(i)acc}_{mc}}{N^{(i)gen}_{mc}} \tag{6.4}$$

where N^{gen}_{mc} is the total number of generated events, $N^{i\ gen}_{mc}$ is the number of generated events in the i^{th} $cos\theta$ bin, N^{acc}_{mc} is the total number of events accepted by the selection and $N^{i\ acc}_{mc}$ is the number of events accepted by the selection in the i^{th} $cos\theta$ bin.

The Monte Carlo efficiency includes the reconstruction efficiency and the selection efficiency of the following cuts:

- Acceptance cut in $cos\theta$.
- Momentum cut.
- Cut in the energy deposited in the calorimeter.
- $\delta R\Phi$ and δRZ cuts.
- Acollinearity cut for the total cross-section and the angular distribution.
- Cut in the sum of the charges (only for the angular distribution).

The global efficiency is given in table 6.1 and the efficiency for each $cos\theta$ bin is shown in figure 6.3.

The selection efficiency of the energy cut found using Monte Carlo was compared with efficiency found using data. From the data a pure sample of muons was defined using:

- The muon chamber quality factor for both tracks was required to be $\leq$ 3.0.

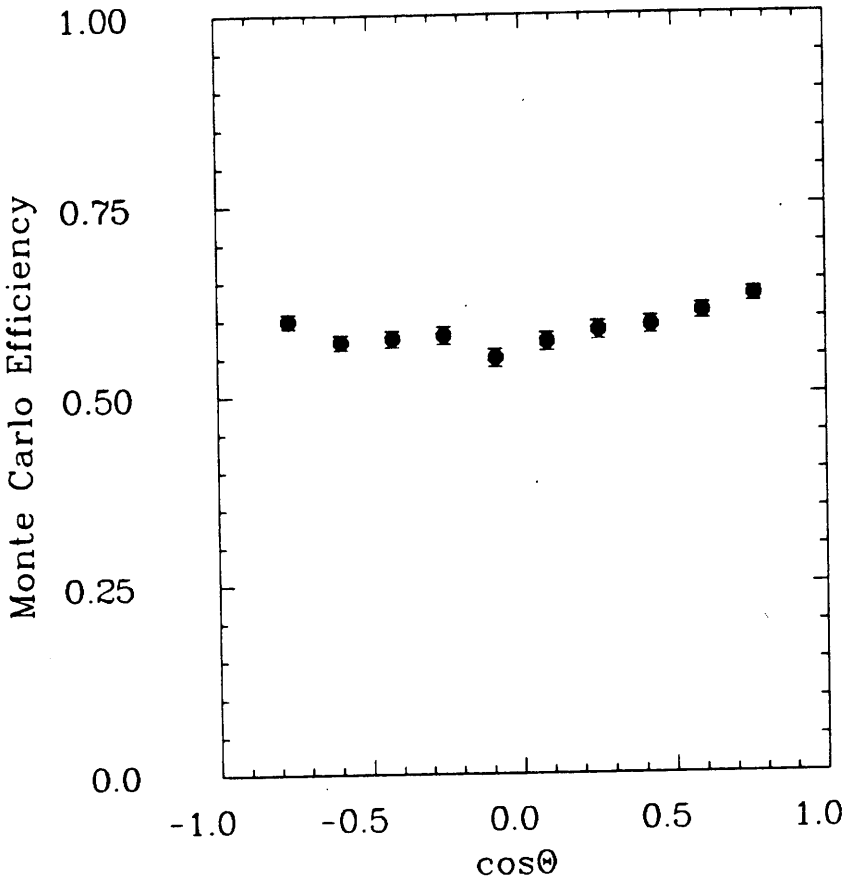

Figure 6.3: Monte Carlo efficiency for each $cos\theta$ bin

- The acollinearity of the tracks must $\leq$ 5^o

The muon chamber quality factor cut leaves a negligible Bhabha contamination and the acollinearity cut rejects $\mu\mu\gamma$ events. The rest of the cuts used in the analysis except the energy cut were also applied.

The efficiency ϵ_E was defined as

$$\epsilon_E = \frac{Number\ of\ events\ selected\ by\ the\ energy\ cut}{Number\ of\ events\ selected\ by\ the\ cuts} \tag{6.5}$$

The data gave an efficiency of 0.973 ± 0.002 and the Monte Carlo ,using the same cuts, an efficiency of 0.967 ± 0.002.

The same procedure was used to compare the selection efficiency of the momentum cut ϵ_p found using Monte Carlo with that found using Bhabha

events. The Bhabha events gave: $\epsilon_p = 0.960 \pm 0.002$ and Monte Carlo events gave: $\epsilon_p = 0.95 \pm 0.002$ for GLOFIT events. For NGLOFIT events Bhabhas gave: $\epsilon_p = 0.897 \pm 0.002$ and Monte Carlo events gave: $\epsilon_p = 0.913 \pm 0.003$.

6.3 Drift time efficiency

The drift time selection efficiency is calculated by comparing the number of Bhabhas n_b^{tim} which pass the timing cut out of a total sample of N_b^{tot} Bhabhas. The global efficiency, given in table 6.4, is then defined as:

$$\epsilon_{tim} = \frac{n_b^{tim}}{N_b^{tot}} \tag{6.6}$$

There is no bin by bin correction because the timing variables were chosen such that they were independent of the path of the track.

6.3.1 Statistical error on the efficiency

To calculate the error on the efficiency the Binomial distribution was used. The statistical error for a given efficiency $\delta\epsilon$ is:

$$\delta\epsilon = \sqrt{\frac{\epsilon(1-\epsilon)}{N}} \tag{6.7}$$

where N is the total number of events used to estimate the efficiency.

6.4 Radiative corrections

After correcting the data for detector and selection inefficiencies, radiative corrections must also be applied so that the data can be compared with the lowest

order cross-section. In section 2.2.2 we showed that only reduced QED corrections need to be applied to the data.

To correct the data the BKJ Monte Carlo is used to generate $\mu\mu$ and $\mu\mu\gamma$ events according to QED only. The total number of $\mu\mu$ and $\mu\mu\gamma$ events N_{mc} and the number of events in i^{th} $cos\theta$ bin are then compared with the QED predictions N_{QED} and N^i_{QED} (see Appendix 2). The correction factor is then given by:

$$(1+\delta)^{(i)} = \frac{N^{(i)}_{MC}}{N^{(i)}_{QED}} \tag{6.8}$$

where $(1+\delta)$ is the total correction factor and $(1+\delta)^i$ is the correction factor for the i^{th} $cos\theta$ bin.

The total correction factor is given in table 6.1 together with the global efficiencies and the bin by bin correction factor is shown in figure 6.4.

ϵ_{ch}	0.914 ± 0.001
ϵ_{mu}	0.973 ± 0.002
ϵ_{mc}	0.527 ± 0.003
ϵ_{tim}	0.997 ± 0.001
$(1+\delta)$	1.279 ± 0.001

Table 6.1: Summary of global efficiencies

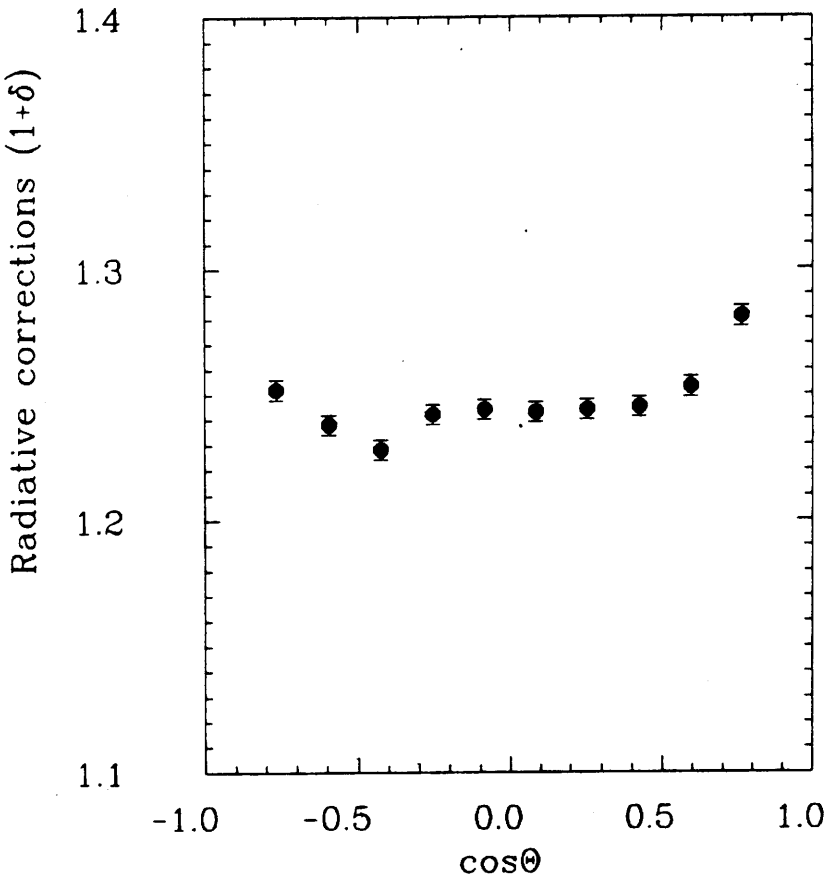

Figure 6.4: Radiative correction factor for each $cos\theta$ bin

Chapter 7

Results

7.1 The total cross-section

The measured total cross-section is given by

$$\sigma_{meas} = \frac{N}{L\epsilon_{tot}(1+\delta)} \tag{7.1}$$

where N is the number of $e^+e^- \rightarrow \mu^+\mu^-$ candidates selected using the procedure described in Chapter 5 after the cosmic ray background has been subtracted, L is the luminosity discussed in Chapter 3, ϵ_{tot} is the total efficiency of the selection procedure $= \epsilon_{trig}\epsilon_{\mu}\epsilon_{mc}\epsilon_{tim}$ and $(1+\delta)$ is the radiative correction, which were discussed in Chapter 6. The results are summarised in Table 7.1 below.

N	3455 ± 66
ϵ_{tot}	0.468 ± 0.003
$(1+\delta)$	1.279 ± 0.001
L	$85.3 \pm 1.1\ pb^{-1}$

Table 7.1: Summary of results for the total cross-section

The errors given in Table 7.1 above are statistical, discussed in Chapter 5. The systematic errors arise from the following sources:

- The systematic error in the luminosity measurement.
- The background subtraction procedure.
- The trigger efficiencies.
- The muon chamber efficiencies.

The systematic error due to the luminosity was estimated to be 4.9%. The background subtraction procedure is sensitive to the definition of the interaction region and the momentum cut. The systematic error was estimated to be 1.0% by examining the change in σ_{meas} when the cuts applied to $\delta R\Phi$, δRZ , $\mid P \mid_{glo}$ and $\mid P \mid_{cel}$ were changed. The systematic errors from the charged trigger efficency and the muon chamber efficiencies were each estimated to be 1%. As these errors are independent they were added in quadrature to give a total systematic error of 5.2%

The measured cross-section is therefore:

$$\sigma_{meas} = 67.7 \pm 1.6 \pm 3.5 pb$$

The QED prediction for $\sigma_{\mu\mu}$ is 70.9 pb, hence

$$R_{\mu\mu} = 0.95 \pm 0.02 \pm 0.05$$

in good agreement with QED.

The CELLO results for σ_{meas} and $R_{\mu\mu}$ at other centre of mass energies [1] [50] and [51] are given together with the above in Table 7.2 and plotted together with the QED prediction in Figure 7.1.

$\sqrt{s}$ GeV	Luminosity pb^{-1}	σ (pb)	$R_{\mu\mu}$
14	0.9	$415.4 \pm 41.0 \pm 22.0$	$0.94 \pm 0.09 \pm 0.05$
22	2.5	$179.4 \pm 14.3 \pm 9.1$	$1.01 \pm 0.08 \pm 0.05$
25	0.2	$131.7 \pm 38 \pm 6.6$	$0.96 \pm 0.28 \pm 0.05$
34.1	11.2	$67.3 \pm 4.1 \pm 3.5$	$0.91 \pm 0.06 \pm 0.05$
35.0	85.3	$67.6 \pm 1.6 \pm 3.5$	$0.95 \pm 0.02 \pm 0.05$
38.3	7.8	$57.4 \pm 4.2 \pm 2.3$	$0.97 \pm 0.07 \pm 0.04$
41.3	3.6	$54.1 \pm 8.9 \pm 2.1$	$1.06 \pm 0.17 \pm 0.04$
43.6	16.9	$44.1 \pm 3.3 \pm 1.7$	$0.97 \pm 0.07 \pm 0.04$
44.2	12.5	$44.7 \pm 4.0 \pm 1.7$	$1.01 \pm 0.09 \pm 0.04$
46.2	4.3	$38.9 \pm 8.9 \pm 1.5$	$0.95 \pm 0.22 \pm 0.04$

Table 7.2: CELLO results for $e^+e^- \rightarrow \mu^+\mu^-$ total cross-section and $R_{\mu\mu}$

[1] The data in [50] around $\sqrt{s} = 34$ GeV have been combined to give one point

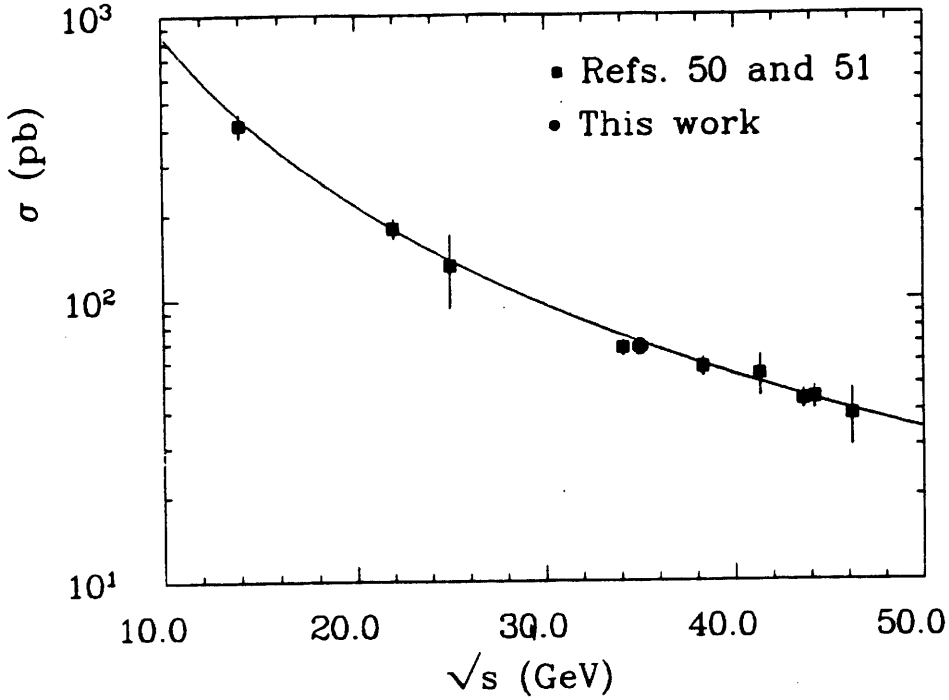

Figure 7.1: The total cross-section for $e^+e^- \rightarrow \mu^+\mu^-$ as a function of centre of mass energy (only statistical errors are shown)

7.1.1 Deviations from QED

In Chapter 2 we saw that the deviations from QED could be, to a good approximation, parameterised by:

$$1 - R_{\mu\mu} = \pm\frac{2s}{\Lambda_\pm^2} \tag{7.2}$$

Using the result for $R_{\mu\mu}$ given above we can put the following lower limits on $\Lambda_\pm$ at the 95% C.L.

$$\Lambda_+ > 136GeV$$

$$\Lambda_- > 277GeV$$

This can be interpreted as QED being valid down to 10^{-18} m.

7.2 The forward backward asymmetry

The measured angular distribution is given in Table 7.3. We present the results in three different ways: the angular distribution, $\frac{dN}{dcos\theta}^1$, corrected only for the detector acceptance and efficiencies, as proposed by Cashmore at al [21]; the angular distribution, $\frac{dN}{dcos\theta}^2$, corrected for reduced QED, which is used to obtain the asymmetry from a fit to the angular distribution and the differential cross-section, $s\frac{d\sigma}{d\Omega}$, for comparison with other measurements. From these results the

$cos\theta$ *bin*	Number of events	$\frac{dN}{dcos\theta}^1$	$\frac{dN}{dcos\theta}^2$	$s\frac{d\sigma}{d\Omega}$ $GeV\ nb\ ster^{-1}$
$-0.85 \rightarrow -0.68$	382 ± 20	4294 ± 235	3432 ± 191	7.84 ± 0.56
$-0.68 \rightarrow -0.51$	383 ± 20	4541 ± 253	3670 ± 205	8.39 ± 0.59
$-0.51 \rightarrow -0.34$	288 ± 17	3394 ± 218	2766 ± 176	6.32 ± 0.50
$-0.34 \rightarrow -0.17$	268 ± 16	3165 ± 212	2551 ± 169	5.83 ± 0.49
$-0.17 \rightarrow 0$	227 ± 15	2894 ± 206	2327 ± 167	5.32 ± 0.48
$0 \rightarrow 0.17$	234 ± 15	2782 ± 194	2238 ± 157	5.12 ± 0.45
$0.17 \rightarrow 0.34$	217 ± 15	2476 ± 176	1993 ± 143	4.56 ± 0.41
$0.34 \rightarrow 0.51$	233 ± 15	2706 ± 188	2175 ± 151	4.97 ± 0.44
$0.51 \rightarrow 0.68$	308 ± 18	3359 ± 200	2682 ± 161	6.13 ± 0.47
$0.68 \rightarrow 0.85$	380 ± 20	4018 ± 218	3138 ± 171	7.17 ± 0.51

Table 7.3: The angular distribution

charge asymmetry can be measured in two ways

1. If we detect F muons in the $+Z$ hemisphere and B events in the $-Z$ hemisphere, then the asymmetry is given by

$$A_{fb} = \frac{F - B}{F + B} \tag{7.3}$$

This gives the asymmetry for the detector acceptance i.e. $\mid cos\theta \mid \leq 0.85$ and must be corrected for this using

$$A_{fb}(\mid cos\theta \mid \leq 1.0) = \frac{3+x^2}{4x} A_{fb}(\mid cos\theta \mid < x) \tag{7.4}$$

where x is the acceptance cut.

2. The asymmetry can also be determined by doing a least squares fit of the differential cross-section to the function

$$f(cos\theta) = N(1 + cos^2\theta + \frac{8}{3} A_{fb} cos\theta)$$

The statistical error on the asymmetry for method (1) is

$$\delta A_{fb} = \frac{2}{(F+B)^2} \left(B^2 \delta^2 F + F^2 \delta^2 B \right)^{\frac{1}{2}} \tag{7.5}$$

If method (2) is used then the statistical error is derived from the fit.

The main sources of systematic error on the asymmetry measurement are:

- The background subtraction procedure
- Incorrect charge assignment to the tracks

The systematic error due to the background subtraction procedure was estimated to be 0.8%. In the data $6\mu^+\mu^+$ events and $6\mu^-\mu^-$ events were found. This gives a probability of misidentifying the charge of a track of 0.2% [49]. However 6% of Monte Carlo events are rejected because they are either $\mu^+\mu^+$ events or $\mu^-\mu^-$ events, compared with 0.3% for the data, and so we estimate the systematic error due to charge misassignment to be 0.5%. The total systematic error on the asymmetry was taken to be 1.0%.

The measured asymmetry using method (1) was found to be

$$A_{fb} = -9.3 \pm 2.0 \pm 1.0\%$$

for the CELLO acceptance. After correcting for the acceptance this becomes:

$$A_{fb} = -10.2 \pm 2.2 \pm 1.0\%$$

Since the asymmetry does not depend on the luminosity, to determine the asymmetry from method (2) the $\frac{dN}{dcos\theta}$ distribution was used in the fit. We obtained:

$$A_{fb} = -8.9 \pm 2.0 \pm 1.0\%$$

with a $\frac{\chi^2}{DoF} = \frac{11.8}{8}$.

These results are consistent with each other. The fitted result, which is used to determine the physical constants below, is in good agreement with the electroweak model prediction given in Chapter 2 of $A_{fb}^{pred} = -8.94$.

These results are given with the other CELLO results for the charge asymmetry obtained by method (2) in Table 7.4 and are plotted with the theoretical prediction in Figure 7.2.

$\sqrt{s}\ GeV$	Luminosity pb^{-1}	Asymmetry
35.0	85.3	$-8.9 \pm 2.0 \pm 1.0\%$
39.0	11.4	$-4.8 \pm 6.5 \pm 1.0\%$
44.0	33.7	$-18.8 \pm 4.5 \pm 1.0\%$

Table 7.4: CELLO results for A_{fb}

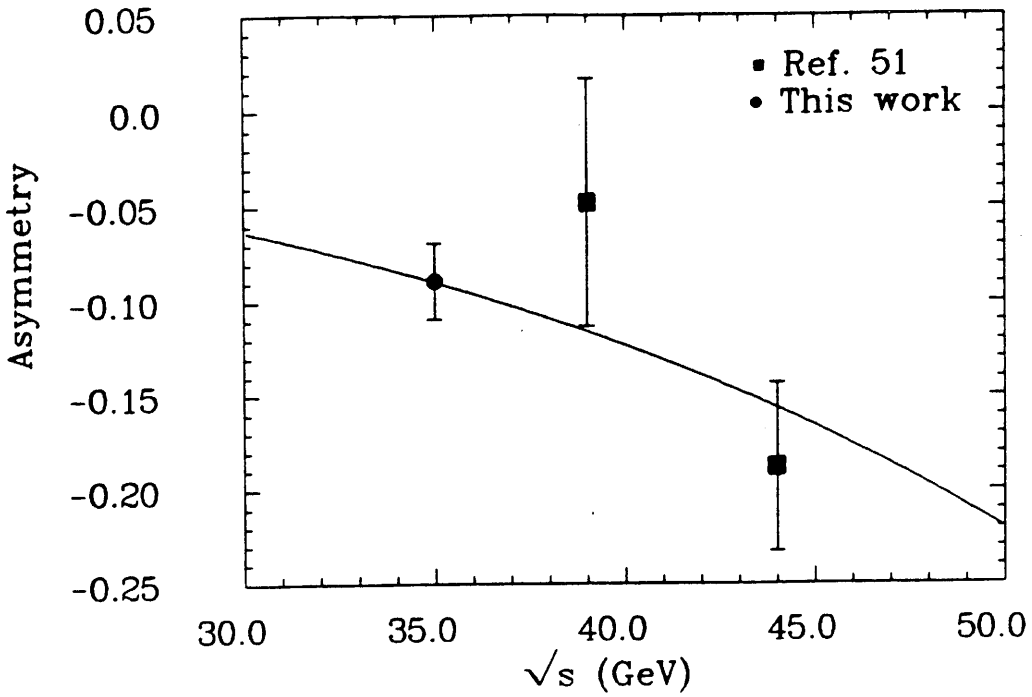

Figure 7.2: The asymmetry as a function of the centre of mass energy (only statistical errors are shown)

The angular distribution was also fitted to a function $f(cos\theta) = N(1+cos^2\theta)$ which is the QED prediction. The fit had a $\frac{\chi^2}{DoF} = \frac{30.2}{9}$.

The angular distribution together with the results of the fits are shown below in Figure 7.3

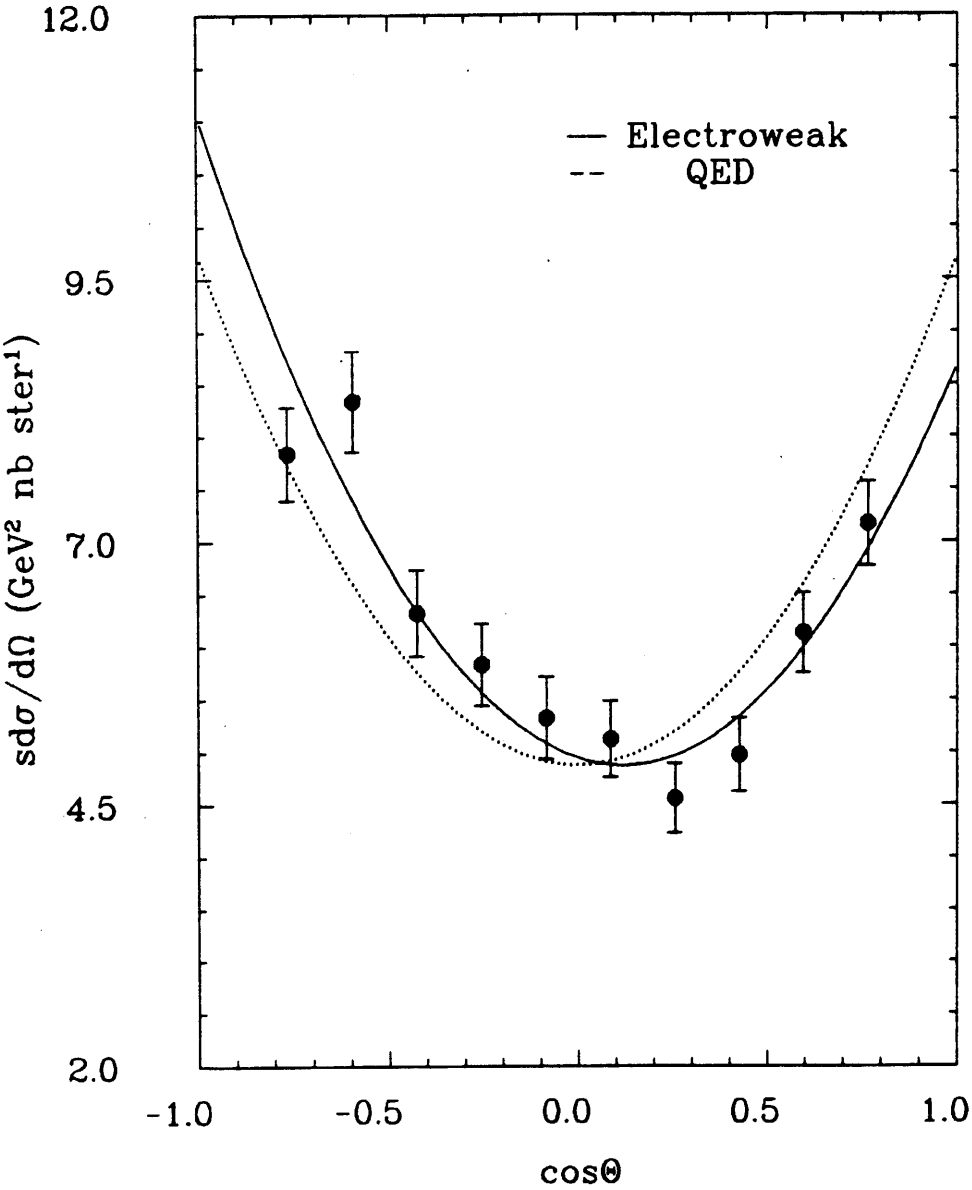

Figure 7.3: The differential cross-section together with the results of the fits.

7.2.1 The axial-vector coupling constants

In Chapter 2 we saw that the asymmetry and the axial-vector coupling constants were related by

$$A_{fb} = \frac{3}{2} a_e a_\mu Re(\chi) \tag{7.6}$$

Using parameterisation 1 for χ, $\sin^2\theta_w = 0.228$ and $M_Z = 92.3$ we find

$$a_e a_\mu = 1.00 \pm 0.25$$

a_e has been determined from $\bar{\nu}_\mu e$ and $\nu_\mu e$ scattering experiments [52] giving $a_e = -0.99 \pm 0.05$. Using this result we find for a_μ

$$a_\mu = -1.01 \pm 0.26$$

which is in good agreement with the electroweak model assumptions of $a_e = a_\mu = -1$.

7.2.2 Determination of $sin^2\theta_w$

A_{fb} is sensitive to $sin^2\theta_w$ through the propagator coupling constant term, χ_1:

$$\chi_1 = \frac{1}{16 sin^2\theta_w (1 - sin^2\theta_w)} \frac{s}{s - M_Z^2} \tag{7.7}$$

A fit was made to the $\frac{dN}{dcos\theta}$ distribution with the normalisation and $sin^2\theta_w$ as free parameters and using $a_e = a_\mu = -1$ and $M_Z = 92.3\ GeV$ giving the result:

$$sin^2\theta_w = 0.23^{+0.10}_{-0.05} \pm 0.01$$

The first error is statistical and the second is the uncertainty in $sin^2\theta_w$ due to the error on M_Z .

This is in good agreement with measurements of $sin^2\theta_w$ from other experiments shown in Figure 2.13.

7.2.3 The ρ parameter

The ratio of the charged current to neutral current coupling can be determined if parameterisation 2 is used:

$$\chi_2 = \rho \frac{G_F M_Z^2}{8\sqrt{2}\pi\alpha} \frac{s}{s - M_Z^2} \tag{7.8}$$

However, as was discussed in Chapter 2, we must correct the asymmetry for full QED radiative corrections. The asymmetry we have presented above have already been corrected for reduced QED radiative corrections and so we need only correct the asymmetry for the QED corrections to the Z^0 exchange diagram. Using the BKJ Monte Carlo we estimated this correction to be +0.7%, giving an asymmetry of

$$-9.6 \pm 2.0 \pm 1.0\%$$

The ρ parameter is then found to be, using the world averages for α and G_F given in table 2.3 and $M_Z = 92.3\ GeV$:

$$\rho = 1.00 \pm 0.20$$

This is in good agreement with the minimal electroweak model prediction of one.

Chapter 8

Search for acoplanar muons

8.1 Introduction

In this Chapter a search for acoplanar muon pairs, a signature of supersymmetric partners of the muon, is described. The analysis was done on data taken at $\sqrt{s} = 43GeV$ corresponding to a total luminosity of $17pb^{-1}$.

8.2 Supersymmetry

The $SU(3)_C \times SU(2)_L \times U(1)_Y$ standard model is in impressive agreement with experiment [18] and there are no experimental results which cast serious doubt on it. However the standard model is considered to be theoretically unsatisfying leaving important questions unanswered such as

- How is gravity to be unified with the other forces ?
- What stabilises the Higgs mass ?

There are several possible answers to these questions. Grand unified theories (GUTs) attempt to embed the $SU(3)_C \times SU(2)_L \times U(1)_Y$ gauge symmetry in a larger gauge group such as $SU(5)$ and $SO(10)$. The theory then has a single coupling constant that all the coupling constants in the standard model approach at the GUT scale which is believed to be of the order of $10^{15} GeV$. Another approach is to consider the quarks and leptons and possibly the $Z^0, W^{\pm}$ and the Higgs bosons to be composite. However probably the most successful approach in recent years has been that of supersymmetry (SUSY) [53]

In the standard model the Higgs mass is

$$M_H = \sqrt{\lambda v^2} \tag{8.1}$$

as shown in Chapter one. If the value of λ becomes too large then perturbation theory breaks down and so an upper limit on the Higgs mass can be determined

$$M_H \leq 1 TeV$$

However the masses of the Higgs are very unstable because they are subject to large corrections from loop diagrams shown in fig 8.1 [54]

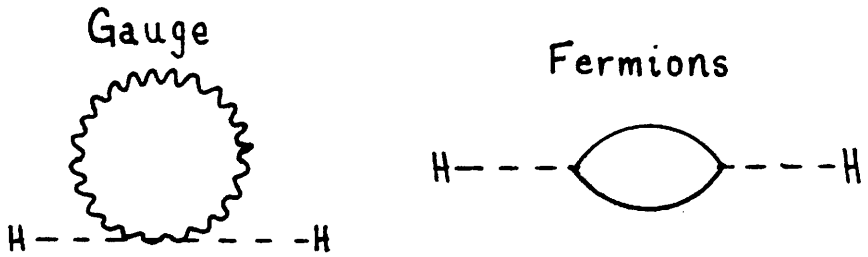

Figure 8.1: Loop corrections to the Higgs mass squared

This gives rise to corrections

$$\delta M_H^2 \simeq \left(\frac{\alpha}{\pi}\right) \Lambda^2 \tag{8.2}$$

where Λ is a cut-off in the loop integrals and can be interpreted as the threshold at which new physics must be introduced. If we require that the corrections δM_H^2 are such that $\delta M_H^2 \leq M_H^2$ then $\Lambda^2 \leq 1TeV^2$.

To solve this problem the loops are cancelled by introducing loops of the opposite sign. For fermion loops, boson loops are introduced and for boson loops, fermion loops are introduced (Figure 8.2).

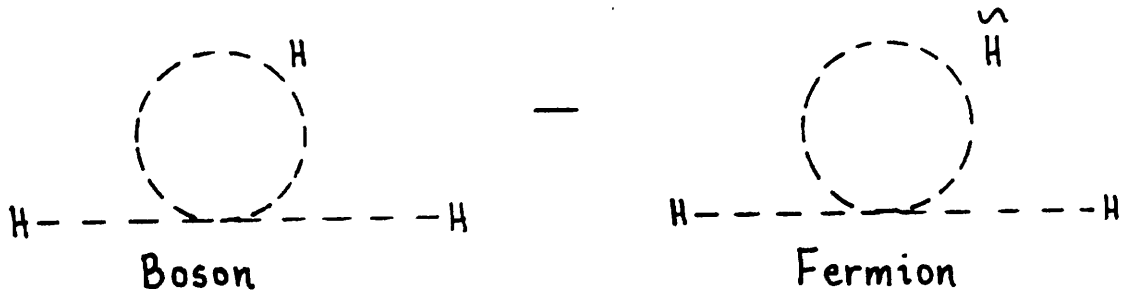

Figure 8.2: Loop corrections to the Higgs mass squared

$$\delta M_H^2 \simeq +O\left(\frac{\alpha}{\pi}\right)(\Lambda^2 + M_b^2) - O\left(\frac{\alpha}{\pi}\right)(\Lambda^2 + M_f^2) \simeq O\left(\frac{\alpha}{\pi}\right)(M_b^2 - M_f^2) \quad (8.3)$$

So the cancellation argument forces the introduction of particles with the same couplings as their partners but differing in spin by $\pm\frac{1}{2}\hbar$ and having a masses $\leq 1TeV$ since

$$(M_b^2 - M_f^2) \sim \Lambda^2 \leq O(1TeV)^2 \quad (8.4)$$

The particles required for the loop cancellations can be produced by SUSY transformations using the SUSY operator, Q

$$Q \mid fermion > \rightarrow \mid boson > \quad (8.5)$$

$$Q \mid boson > \rightarrow \mid fermion > \quad (8.6)$$

where the sparticles have the same couplings as their partners.

The incorporation of gravity can be done naturally in SUSY theories. The SUSY transformation changes spin which is space-time dependent since it is related to rotations. Global supersymmetry is invariant under space-time translations but if, as experience with the standard model indicates, the SUSY transformation is local then the SUSY transformations are space-time dependent and are invariant only under general co-ordinate transformations which are basis of general relativity. Local SUSY is usually called supergravity.

The simplest realistic SUSY model is $N = 1$, indicating that it has a single SUSY operator. This model predicts the particle spectrum shown in Table 8.1 The mass eigenstates may be mixtures of electroweak eigenstates $\tilde{\gamma}$, $\tilde{z}^0$, $\tilde{h}_1^0$ or of $\tilde{w}_1^{\pm}$, $\tilde{h}_1^{\pm}$ or of $\tilde{q}_l$, $\tilde{q}_r$, or of $\tilde{l}_l$, $\tilde{l}_r$.

Spin	0	$\frac{1}{2}$	1	$\frac{3}{2}$	2
matter	$\tilde{l}_L$ $\tilde{l}_R$	l			
multiplets	$\tilde{q}_L$ $\tilde{q}_R$	q			
		$\tilde{g}$	g		
		$\tilde{\gamma}$	γ		
Gauge	h_w	$\tilde{w}_1$, $\tilde{w}_2$	$W^{\pm}$		
Multiplets	h_z	$\tilde{z}_1$, $\tilde{z}_2$	Z^0		
	h, a	$\tilde{h}$			
				$\tilde{G}$	G

Table 8.1: Particle spectrum of the minimal SUSY model

8.2.1 Signatures for supersymmetry

Most SUSY models have a multiplicatively conserved quantum number R-parity [55] defined by

$$R = (-1)^{2J+3B+L}$$

where J is the particle spin, B its baryon number and L its lepton number. Therefore particles have $R = +1$ and their supersymmetric partners have $R = -1$. This has the following important consequences for their detection. The lightest SUSY particle must be stable and sparticles will be produced in pairs. In this analysis it is assumed that the lightest SUSY particle is the photino. Scalar muons are therefore pair produced in e^+e^- annihilation and decay into photinos as shown in Figure 8.3. The photino will not be detected because its

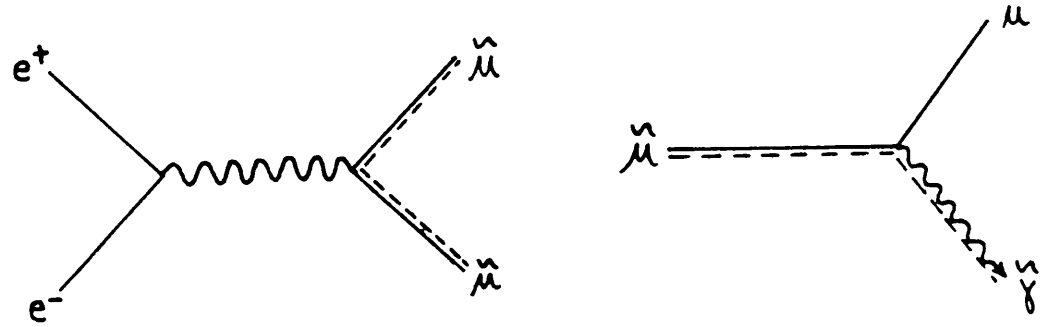

Figure 8.3: Production and decay of scalar muons

interaction with matter is weak [56] since any interaction requires the production and/or decay of heavy particles. The signature for scalar muons is therefore a muon pair with missing momentum.

The cross-section of such events [57] is, normalised to the QED muon cross-section, for a scalar muon of mass $M_{\tilde{\mu}}$ is

$$R_{\tilde{\mu}\tilde{\mu}} = \frac{1}{4}\beta^3 \tag{8.7}$$

where $\beta = \sqrt{1 - \frac{M_{\tilde{\mu}}^2}{E_b^2}}$ for beam energy E_b.

Since the mass eigenstates may be mixtures of the left-handed and right-handed states two extreme assumptions are made about the masses of the scalar muons when deriving the mass-limits. The masses were of the left-handed and right-handed states were assumed to be the same or the mass of the right-handed state was much less than the mass of the left-handed state. The cross-section given above assumes degenerate masses. If the masses are not degenerate as in the second assumption the cross-section is reduced by a factor of two.

8.3 Data analysis

The data were collected using a trigger (trigger 8) which required two track candidates in the $R\Phi$ projection with an opening angle of at least 20^0 and a hit in a muon chamber to which one of the tracks points. The restriction on the opening angle leads to a maximum acoplanarity of 160^0, where the acoplanarity of two tracks is the angle between them in the $R\Phi$ projection as shown in fig 8.4, where $\vec{p}_{\pm}$ are the momentum vectors of the muons and $\hat{z}_0$ is the unit vector in the Z-direction which is the direction of the electrons.

The following cuts were then applied to the data,

1. Two fully reconstructed tracks must be found in the central tracker within $|\cos\theta| \leq 0.85$ and coming from the interaction point, as was defined for the muon analysis.

2. Both tracks should have a momentum of at least $3\frac{GeV}{c}$ and a linked shower

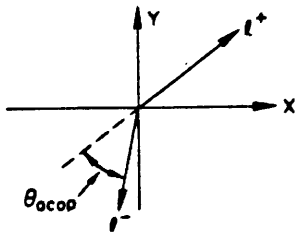

$$\theta_{acop} = 180^{o} - \cos^{-1} \frac{(\vec{p}_{+} \times \hat{z}_0) \cdot (\vec{p}_{-} \times \hat{z}_0)}{| \vec{p}_{+} \times \hat{z}_0 | \cdot | \vec{p}_{-} \times \hat{z}_0 |} \tag{8.8}$$

Figure 8.4: Definition of acoplanarity

energy $\leq 1.3GeV$.

3. At least one track should have muon hit quality of ≤ 5.

4. The acoplanarity of the two tracks must be $\geq 20^0$.

5. The missing transverse momentum must be $> 4\frac{GeV}{c}$.

6. There should be no other visible showers in the barrel, endcap calorimeters and in the holetagger.

The cuts 1,2 and 5 reject background from $e^+e^- \rightarrow ee\mu\mu$, radiative μ-pair production is vetoed by 6 and cosmic ray events are removed by 1 and 4. No events were found after these cuts were applied.

8.3.1 Efficiencies

Trigger efficiency

This was determined using the cosmic ray sample described in Chapter five. The efficiency was defined as

$$\epsilon_8 = \frac{Number\ of\ events\ with\ \ charged\ trigger\ and\ trigger\ 8}{Number\ of\ events\ with\ charged\ trigger} \tag{8.9}$$

where the charged trigger was defined in Chapter 3. The efficiency was found to be

$$\epsilon_8 = 0.50 \pm 0.01$$

Tracking efficiency

The tracking efficiency describes how good the reconstruction programs are at finding tracks and reconstructing them. It was determined using two different Bhabha samples. Events with one track having a linked shower in the calorimeter and another shower back-to-back with track, N_1 and events with two tracks each with a linked shower, N_2. The inefficiency of finding one of two tracks is then:

$$\alpha_1 = \frac{2N_1}{N_1 + 2N_2} \tag{8.10}$$

The probability of finding two tracks is then,

$$\epsilon_{trk} = (1 - \alpha_1)^2 \tag{8.11}$$

This result is derived in appendix 2. The tracking efficiency is found to be

$$\epsilon_{trk} = 0.986 \pm 0.008$$

Muon chamber efficencies

The efficiency of the identification of a muon by the muon chambers using the quality factor defined in Chapter four was calculated in the same way as for the μ-pair analysis.

$$\epsilon_\mu = 0.94 \pm 0.01$$

Selection efficiency

To determine the selection efficiency a Monte Carlo [58] was used to generate events for a given scalar muon mass and photino mass. Initial state radiation was included [59] since this is important for pair production of particles with threshold near the beam energy. The cuts used to analyse the data were applied to these events. The resulting selection efficiency is then given by

$$\epsilon_{sel} = \frac{N_{sel}}{N_{gen}} \tag{8.12}$$

where N_{gen} is the number of events generated and N_{sel} is the number of events selected from N_{gen}. The efficiencies are presented as a function of scalar muon and scalar photon mass in Figure 8.5 where curve (a) is for $M_{\tilde{\gamma}} = 0\ \frac{GeV}{c^2}$, (b) is for $M_{\tilde{\gamma}} = 5\ \frac{GeV}{c^2}$, (c) is for $M_{\tilde{\gamma}} = 10\ \frac{GeV}{c^2}$, and (d) is for $M_{\tilde{\gamma}} = 15\ \frac{GeV}{c^2}$.

8.3.2 Statistical analysis

To turn the fact that no events were observed into a statement about the scalar muon mass Poisson statistics are used.

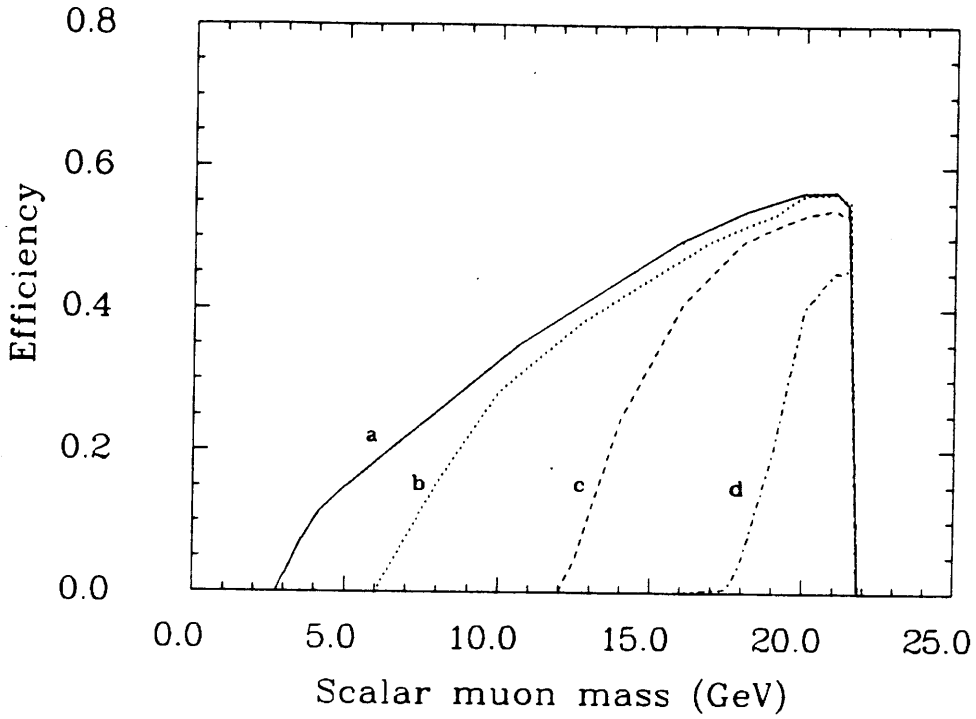

Figure 8.5: Selection efficiency of scalar muons as function of the scalar muon mass and the photino mass

The Poisson distribution is

$$P(n) = \frac{m^n e^{-m}}{n!} \tag{8.13}$$

where $P(n)$ is the probability of observing n events which occur with rate m. The mean $\bar{n}$ and the variance σ^2 are given by

$$\bar{n} = m \qquad \sigma^2 = m \tag{8.14}$$

For a Poisson distribution a confidence level (C.L.) is defined in terms of an upper limit [60]. The confidence level associated with a given upper limit N for an observed value n_0 of n is the probability that $n > n_0$ if $\bar{n} = N$ i.e.

$$C.L. = 1 - \sum_{n=0}^{n_0} P(n) \tag{8.15}$$

So for a 95% confidence level we require

$$\sum_{n=0}^{n_0} P(n) = 0.05$$

so

$$e^{-\bar{n}} = 0.05$$

Therefore

$$\bar{n} = N = 3$$

So the upper limit on the observed number of events, N_{up}, consistent with the observed result of zero events is 3 at the 95% C.L.

The efficiency for detecting a scalar muon and its cross-section as a function of its the scalar muons mass and the photino mass was calculated using the Monte Carlo described above. The visible number of expected events N_{exp} can then be calculated for luminosity L

$$N_{exp} = L\epsilon_8\epsilon_{trk}\epsilon_\mu\epsilon_{sel}\sigma_{mc} \tag{8.16}$$

The 95% C.L. curve for the mass is then drawn by plotting the masses $M_{\tilde{\mu}}$, $M_{\tilde{\gamma}}$ for which

$$N_{exp} = N_{up}$$

8.4 Results

The excluded mass regions for the case $M_{\tilde{\mu}R} = M_{\tilde{\mu}L}$ and $M_{\tilde{\mu}R} << M_{\tilde{\mu}L}$ are shown in fig 8.6 and are given below for $M_{\tilde{\gamma}} = 0$

$$2.8 < M_{\tilde{\mu}L} = M_{\tilde{\mu}R} < 20.5 \frac{GeV}{c^2}$$

$$3.4 < M_{\tilde{\mu}R} < 19.4 \frac{GeV}{c^2} < M_{\tilde{\mu}L}$$

The results of other experiments are given in Table 8.2.

Experiment	$M_{\tilde{\mu}}(\frac{GeV}{c^2})$
JADE [61]	> 20.3
MARK J [62]	> 20.0
TASSO [63]	> 16.4

Table 8.2: Limits on the scalar muon mass for $M_{\tilde{\gamma}} = 0$ at the 95% C.L. from other experiments

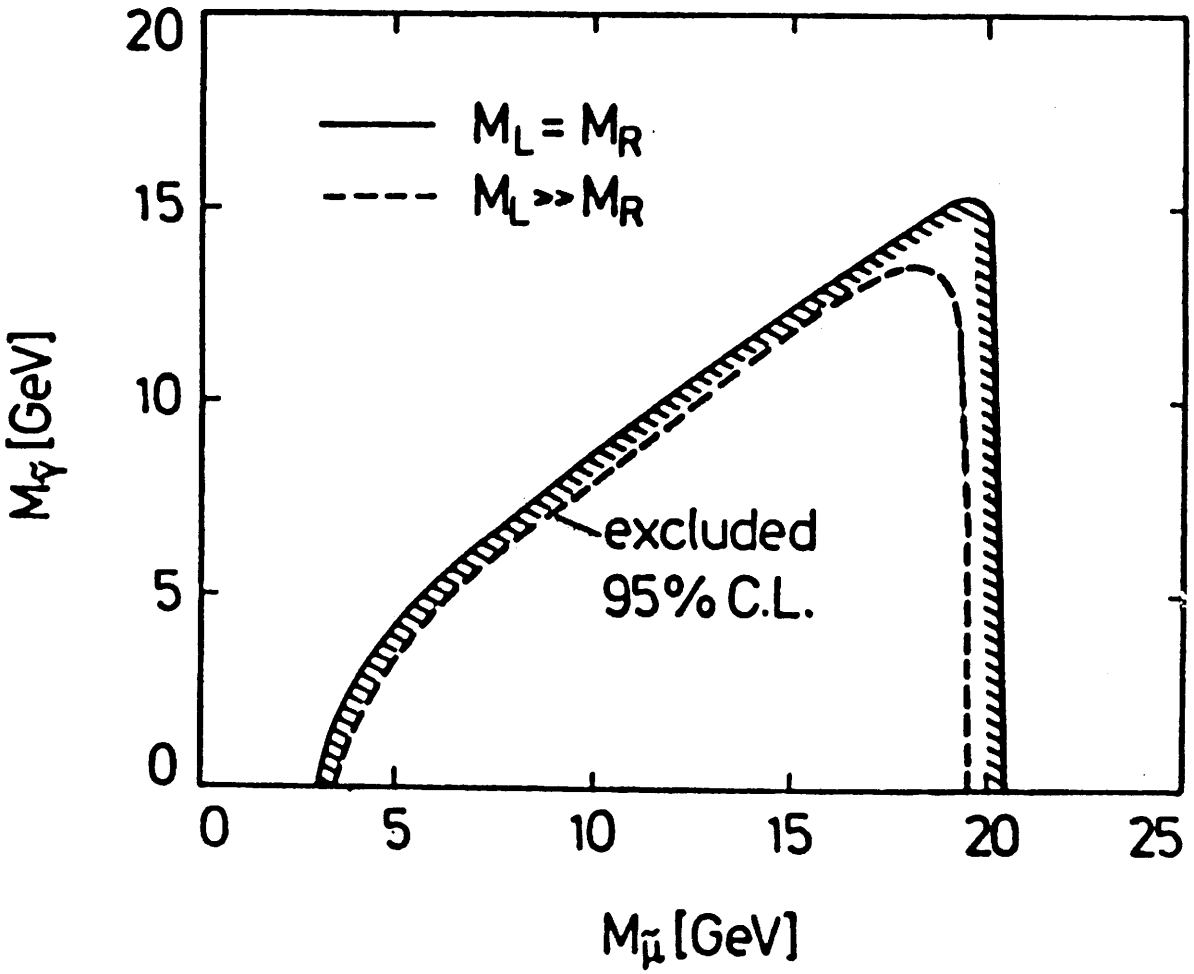

Figure 8.6: Excluded masses of scalar muons and photinos at the 95% C.L.

Chapter 9

Summary and conclusions

From 85.3 pb^{-1} of data collected at $\sqrt{s} = 35\ GeV$ with the CELLO detector at PETRA, $e^+e^- \rightarrow \mu^+\mu^-$ events were selected and the total cross-section ,σ, and the electroweak charge asymmetry, A_{fb}, measured giving

$$\sigma = 67.7 \pm 1.6 \pm 3.5\ pb$$

$$A_{fb} = -8.9 \pm 2.0 \pm 1.0\%$$

where both quantities have been corrected for reduced QED and the asymmetry was obtained from a fit to the angular distribution.

At PETRA energies the total cross-section is, to a good approximation, described by QED. By comparing the measured cross-section with the QED expectation we obtained:

$$R_{\mu\mu} = \frac{\sigma}{\sigma_{QED}} = 0.95 \pm 0.02 \pm 0.05$$

This was used to put limits on deviations from QED. The limits obtained at

the 95% C.L. were:

$$\Lambda_+ > 136 \qquad \Lambda_- > 277\ GeV$$

This can be interpreted as a test of the validity of QED down to $10^{-18}\ m$.

The measured asymmetry was found to be in good agreement with the electroweak model expectation of -8.94%. This contradicts previous results in this energy region which were lower than the electroweak model predictions.

From the asymmetry the product of the axial-vector couplings of the electron and the muon was obtained:

$$a_e a_\mu = 1.00 \pm 0.25$$

Using the result for a_e from $\bar{\nu}_\mu e$ and $\nu_\mu e$ scattering experiments we find:

$$a_\mu = -1.01 \pm 0.26$$

Both these results are in good agreement with the electroweak model assumptions of $a_e = a_\mu = -1$.

A fit to the angular distribution was made to determine $sin^2\theta_w$. The result obtained was

$$sin^2\theta_w = 0.23^{+0.10}_{-0.05} \pm 0.01$$

the first error is statistical and the second due to the uncertainty on M_Z . This result is in good agreement with measurements of $sin^2\theta_w$ from other experiments.

After correcting the asymmetry for full QED corrections the ratio of the neutral coupling to the charged coupling constant, the ρ parameter, was deter-

mined from the asymmetry:

$$\rho = 1.00 \pm 0.20$$

This is in good agreement with the value predicted by the minimal electroweak model of one.

Using 17 pb^{-1} of data collected at $\sqrt{s} = 43\ GeV$ a search for acoplanar muons, a signature of scalar muons predicted by supersymmetric theories, was made. No candidate events were found and the following mass regions were excluded at the 95% C.L.

$$2.8 < M_{\tilde{\mu}L} = M_{\tilde{\mu}R} < 20.5\ \frac{GeV}{c^2}$$

$$3.4 < M_{\tilde{\mu}R} < 20.5\ \frac{GeV}{c^2}\ < M_{\tilde{\mu}L}$$

assuming $M_{\tilde{\gamma}} = 0\ \frac{GeV}{c^2}$.

In conclusion, we have found that all the physical parameters derived from an analysis of $e^+e^- \rightarrow \mu^+\mu^-$ are in good agreement with the predictions of the electroweak model and that there is no evidence for the existence of scalar muons predicted by supersymmetric theories.

Appendix 1

Here the calculation of the radiative correction applied to the i^{th} $cos\theta$ bin is presented in detail.

The lowest order QED angular cross-section is given by:

$$\left(\frac{d\sigma}{dcos\theta}\right)_0 = \frac{3}{8}\sigma_0(1+cos^2\theta) \tag{9.1}$$

where σ_0 is the lowest order QED total cross-section given in chapter 2.

The cross-section scattering into a given $cos\theta$ bin σ_0^i is therefore:

$$\sigma_0^i = \frac{3}{8}\sigma_0((x_h - x_l) + \frac{1}{3}(x_h^3 - x_l^3)) \tag{9.2}$$

where x_h is the upper limit on the bin and x_l the lower limit on the bin.

The radiative correction applied to the i^{th} $cos\theta$ bin is:

$$(1+\delta)^i = \frac{\sigma_{MC}^i}{\sigma_0^i} \tag{9.3}$$

where σ_{MC}^i is the generated cross-section in the i^{th} bin. This is related to the number of generated events by:

$$\sigma_{MC}^i = N_{MC}^i \frac{\sigma_{MC}}{N_{MC}} \tag{9.4}$$

where N_{MC}^i is the number of generated events in the i^{ih} bin. σ_{MC} is the total generated cross-section, given by the BKJ Monte Carlo and N_{MC} is the total number of generated events.

Combining the above we get:

$$(1+\delta)^i = \frac{8}{3}\frac{\sigma_{MC}}{\sigma_0}\frac{N_{MC}^i}{N_{MC}}\frac{1}{((x_h - x_l) + \frac{1}{3}(x_h^3 - x_l^3))} \tag{9.5}$$

Appendix 2

Charged track reconstruction efficiency

For N events with two charged particles such as $e^+e^- \rightarrow \mu^+\mu^-$ there are three subsets of events corresponding to the three possible outcomes of the track reconstruction:

1. No tracks found; N_0 events

2. 1 track found; N_1 events

3. 2 tracks found; N_2 events

If we define α_+ as the probability of not reconstructing a positively charged track and α_- as the probability of not reconstructing a negatively charged track then

$$N_0 = \alpha_+\alpha_-N \tag{9.6}$$

$$N_1 = \alpha_+(1-\alpha_-)N + \alpha_-(1-\alpha_+)N \tag{9.7}$$

$$N_2 = (1-\alpha_+)(1-\alpha_-)N \tag{9.8}$$

If we assume $\alpha_+ = \alpha_- = \alpha$ then the above equations become:

$$N_0 = \alpha^2N \tag{9.9}$$

$$N_1 = 2\alpha(1-\alpha)N \tag{9.10}$$

$$N_2 = (1-\alpha)^2N \tag{9.11}$$

We can measure N_1 and N_2 from Bhabha events so from (9.10) and (9.11) we get:

$$\frac{1-\alpha}{2\alpha} = \frac{N_2}{N_1} \tag{9.12}$$

and finally we find:

$$\alpha = \frac{2N_1}{N_1 + 2N_2} \tag{9.13}$$

References

[1] F.J. Hasert et al., Phys Lett 46B (1973) 121, Phys Lett 46B (1973) 138.

[2] G. Arnison et al., Phys Lett 112B (1983) 103, Phys Lett 126b (1983) 398. M. Banner et al., Phys Lett 122B (1983) 476, P. Bagnaia et al., Phys Lett 129B (1983) 130.

[3] T.D. Lee and C.N. Yang, Phys Rev 104 (1956) 254.

[4] C.S. Wu et al., Phys. Rev. 105 (1957) 1413.

[5] R.P. Feynman and M. Gell-Man, Phys Rev 110 (1958a) 1178.

[6] P.D. Gall, DESY 86-040 and references therein.

[7] E.D. Commins and P.H. Bucksbaum, Weak Interactions of Leptons and Quarks, Cambridge University Press.

[8] S. Glashow, Nucl Phys 22 (1961) 579.

[9] P.W. Higgs Phys Rev Lett 13 (1964) 508.

[10] C.N. Yang and R. Mills, Phys Rev 96 (1954) 191.

[11] S. Weinberg, Phys Rev Lett 19 (1967) 1264.

[12] A. Salam, Proc 8th Nobel Symposium, Stockholm 1968, ed. Almqvist and Wiksell.

[13] G. t' Hooft, Nucl Phys B33 (1971) 173, Nucl Phys B33 (1971) 167.

[14] E.S. Abers and B.W. Lee, Phys Rep 9C(1) (1973) 1.

[15] S.D. Drell, Ann Phys 4 (1958) 75.

[16] D. Saxon, RAL 86-073; CELLO collab., DESY 87-005.

[17] Particle Data Group, Review of particle properties, Phys Lett 170B (1986).

[18] G. Altarelli, 23rd International Conference on High Energy Physics, Berkeley.

[19] W. de Boer, 17th Int. Symp. on Multiparticle Dynamics, Austria, 1986.

[20] W. Marciano, 23rd International Conference on High Energy Physics, Berkeley.

[21] R. Cashmore et al, Oxford preprint 45/85.

[22] W. Hollik, DESY 86-049.

[23] M. Bohm and W. Hollik, Phys Lett 139B (1984) 213.

[24] F.A. Berends et al, Nucl Phys B202 (1982) 63 and Comp Phys Comm 29 (1983) 185.

[25] R.W Brown et al, Phys Rev Lett 52 (1984) 1192.

[26] B. Naroska DESY 86-051 and 21st Recontre de Moriond, Les Arcs, 1986.

[27] H.Jung, Private communication.

[28] H-J. Behrend et al., Physica Scripta 23 (1981) 610.

[29] M. Cohen, Etude des performances des chambres proportionalles du detecteur central CELLO, These 3eme cycle LAL 80/10 (unpublished).

[30] W. De Boer et al., Nucl Instr and Meth 176 (1980) 167.

[31] W. De Boer et al., Nucl Instr and Meth 217 (1983) 255.

[32] F. Sauli, CERN 77-09.

[33] B. Sack, Die Strahlkammer des CELLO detektor, MPI-PAE/EXP E1 133 (1984).

[34] H. Desportes et al., Construction and test of CELLO thin wall solenoid. Contribution to 21st Cryogenic Engineering Conference, Madison, Wisconsin, August 1979.

[35] G. Flugge, Karlsruhe preprint Kfk 3288.

[36] R. Aleksan et al., Nucl Instr and Meth 185 (1981) 95.

[37] H-J. Behrend, Comp Phys Comm 22 (1981) 365.

[38] J. Knapp, CELLO note K-081; K. Gamerdinger et al, CELLO note K-101.

[39] D. Notz, DESY 85-046.

[40] G. Franke, CELLO note D-085.

[41] V. Blobel, DESY Internal Report DESY F14-79/02.

[42] W. De Boer and I. Hildebrandt, CELLO note M-159.

[43] Gluckenstern, N.I.M. 24 (1963) 381.

[44] J. Pamela, PhD Thesis, Universite Paris Sud (1986), Note CEA-N-2400.

[45] M. Feindt, CELLO note D-042.

[46] R.L. Ford and W.R. Nelson, SLAC 210 (1977).

[47] HETC: Monte Carlo High Energy Nucleon Transport Code, RSIC Computer Code Collection, ORNL CCC-178.

[48] O.C. Allkofer et al., Phys Lett 36B (1971) 425.

[49] F. Ould-Saada, PhD Thesis, Saclay, CEA-N-2505.

[50] H-J. Behrend et al., Z. Phys 14C (1982) 283.

[51] H-J. Behrend et al., Phys Lett 191B (1987) 209.

[52] G. Barbellini and C. Santoni, Riv Cim 9 Nr2 (1896).

[53] J. Wess and B. Zumino, Nucl. Phys. B70 (1974) 39; A. Salam and J. Strathdee, Nucl. Phys.B76 (1974) 477; P Fayet, Phys. Lett. 69B (1977) 489; H.E. Haber and G.L. Kane, Phys Rep 117 (1985) 75.

[54] J. Ellis, Int. Symp. on Lepton and Photon Interactions at High Energies, Kyoto 1985.

[55] P. Fayet, Phys. Lett. 69B (1977) 489.

[56] P. Fayet Phys. Lett. 86B (1979) 272.

[57] G. Farrar and P. Fayet, Phys. Lett. 84B (1980) 191.

[58] H.Kuster, PhD Thesis, Karlsruhe Preprint KfK 4294.

[59] F. Bonneau and F. Martin Nucl. Phys. B27 (1971) 381.

[60] Particle Data Group, Review of particle properties, Phys Lett 170B (1986).

[61] W. Bartel et al, Phys. Lett. 152B (1985) 392.

[62] B. Adevra et al, Phys. Lett. 152B (1985) 439.

[63] R. Brandelik et al, Phys. Lett. 117B (1982) 365. Phys. Lett. 170B (1986).